

# *In situ* transmission electron microscopy investigations of electromigration in metals

Proefschrift

ter verkrijging van de graad van doctor  
aan de Technische Universiteit Delft,  
op gezag van de Rector Magnificus prof. ir. K.C.A.M. Luyben,  
voorzitter van het College voor Promoties,  
in het openbaar te verdedigen op  
25 september 2015 om 15:00 uur

Door

Tatiana KOZLOVA  
Master of Science in Physics,  
Novosibirsk State University, Rusland  
geboren te Novokuznetsk, Sovjet-Unie

Dit proefschrift is goedgekeurd door de promotor(en):

Prof.dr. H.W. Zandbergen

Samenstelling promotiecommissie:

Rector Magnificus

Prof.dr. H.W. Zandbergen

Prof.dr. J.M. van Ruitenbeek

Dr.ir. F.D. Tichelaar

Technische Universiteit Delft, promotor

Universiteit Leiden

Technische Universiteit Delft

Independent members:

Prof. D.C. Bell

Prof.dr.ir. H.S.J. van der Zant

Prof.dr. P.J. French

Prof.dr.ir. R. Benedictus

Dr. H. Bender

Harvard University

Technische Universiteit Delft

Technische Universiteit Delft

Technische Universiteit Delft

Imec Company

This research was financially supported by ERC project 267922.

*Keywords:* Electromigration, Transmission Electron Microscopy, *in situ*

*Printed by:* Gildeprint Drukkerijen

Copyright © 2015 by Tatiana Kozlova

ISBN 978-90-8593-226-0

Casimir PhD-series, Delft-Leiden 2015-18

An electronic version of this dissertation is available at <http://repository.tudelft.nl/>

*To my family*



# Contents

<b>Chapter 1</b> Introduction to Electromigration and Thesis Outline	1
1.1. Electromigration	2
1.1.1. Brief history	2
1.1.2. Atomistic approach	3
1.1.3. Joule heating	6
1.1.4. Accelerated electromigration experiments	8
1.2. Motivation of research	8
References	9
<b>Thesis outline</b>	13
<b>Chapter 2</b> Experimental Technics and Sample Fabrication	15
2.1. Investigation tools	16
2.1.1. Transmission electron microscopy (TEM)	16
2.1.2. Atomic force microscopy (AFM)	22
2.2. Sample fabrication / Clean room processing	22
2.3. <i>In situ</i> TEM experiments	27
2.3.1. Electrical measurements	28
2.3.2. Heating experiments	30
2.3.3. Joint electrical – heating experiments	30
References	31
<b>Chapter 3</b> The Use of STEM Imaging to Analyze Thickness Variations	35
3.1. Introduction	36
3.2. Experiment	36
3.3. Results and discussion	37
3.3.1. Grain growth due to the Joule heating	37
3.3.2. The ways of mass-thickness contrast enhancement: camera length decrease and averaging through tilt series	38
3.3.3. STEM and AFM imaging correlation	41
3.3.4. STEM imaging of nanogaps	42
3.4. Conclusions	43
References	43
<b>Chapter 4</b> Reversible Electromigration in Pd–Pt Nanobridges	45
4.1. Introduction	46
4.2. Experiment	47

4.3. Results and discussion	48
4.3.1. Electromigration visualisation in TEM mode	48
4.3.2. Electromigration visualisation in STEM mode	49
4.3.3. Material transfer analysis	51
4.3.4. Grain boundaries grooving	54
4.3.5. Bridge breakage due to the Joule heating	55
4.4. Conclusions	55
References	56
<b>Chapter 5</b> The Origin of Increased Resistivity in Platinum Nanobridges	59
5.1. Introduction	60
5.2. Experiment	61
5.3. Results and discussion	62
5.3.1. Electrical resistance change of Pt nanobridge during heating	62
5.3.2. The origin of increased resistivity in thin metallic films	64
5.3.3. Estimation of the four contributions to the total resistivity	65
5.3.4. Experiment limitation	68
5.4. Conclusions	69
References	69
Appendix A5	71
<b>Chapter 6</b> Electromigration in Pt Nanobridges at Different Substrate Temperatures	73
6.1. Introduction	74
6.2. Experiment	75
6.3. Results and discussion	77
6.3.1. Electromigration at $T_s = 100$ K	77
6.3.2. Local temperature determination	78
6.3.3. Electromigration at $T_s = 300$ K	80
6.3.4. Electromigration at $T_s = 420$ K	80
6.3.5. Electromigration at $T_s = 660$ K	82
6.3.6. Critical power of the bridge break	84
6.3.7. Comparison of different substrate temperature regimes	84
6.3.8. Change of the bridge resistance due to the grain growth	85
6.4. Conclusions	87
References	87
<b>Chapter 7</b> Towards <i>in situ</i> TEM Investigations of Nanoparticles under Dynamic Conditions	91
7.1. Introduction	92
7.2. Achievements and difficulties in <i>in situ</i> TEM molecular electronic properties investigations	93
7.2.1. Visualisation of SCO NPs using TEM	93

7.2.2. Nanoparticles trapping	95
7.2.3. Remaining challenges	97
7.3. Conclusions	98
References	99
Appendix A7	101
<b>Summary</b>	103
<b>Samenvatting</b>	105
<b>Curriculum Vitae</b>	107
<b>Publications</b>	109
<b>Acknowledgements</b>	111



---

# *Chapter 1*

---

## Introduction to Electromigration and Thesis Outline

This chapter gives a short introduction to electromigration process describing the several theoretical approaches to explain the physics of the process. Furthermore the method applied throughout this thesis of performing accelerated electromigration experiments in transmission electron microscope is explained. At the end of the chapter, the thesis outline is given.

## 1.1. Electromigration

### 1.1.1. Brief history

Electromigration is a process in which a metallic contact line is thinned by passing a current through it, which occurs because of a gradual displacement of atoms, ultimately leading to destruction of the wire. Electromigration was first reported in 1861 by M. Gerardin<sup>1</sup>. In that study mass motion in molten alloys of mercury–sodium (Hg–Na) and lead–tin (Pb–Sn) had been observed. But the big interest to electromigration phenomena was raised only around 1960's due to a problem of interconnects failures in commercially available integrated circuits. The first observation of electromigration in thin metallic films was done by I. Blech<sup>2,3</sup>. Among literature reviews of the early days Jost<sup>4</sup>, Seith and Wever<sup>5</sup>, Huntington<sup>6</sup>, Ho and Kwok<sup>7</sup> can be listed.

Failure of integrated circuits in microelectronics due to electromigration is a big limitation on the maximum allowed current density or power through the device<sup>8,9</sup>. Typical example of integrated circuit failure is shown in Figure 1.1(a). When wires are downscaled to nano-sizes, the maximum allowed current diminishes even further (due to decrease of wire cross-section). So, the threshold value to start the electromigration process is achieved easily.

Although electromigration leads to failure in micro and nanoelectronics, it can also be applied constructively. One well-known application is the creation of nanogaps, the typical image of it is shown in Figure 1.1(b). Nanogaps are used to determine the electronic properties of small particles or molecules<sup>10-13</sup>. Park *et al.*<sup>10</sup> reported a highly reproducible method to fabricate metallic electrodes with nanometer separation by passing a high electric current through an Au nanowire. Later, Prins *et al.*<sup>14</sup> showed that much more stable nanogaps can be manufactured with platinum (Pt), owing to the much higher surface mobility of Au, which results in the rapid rounding of the electrode tip.

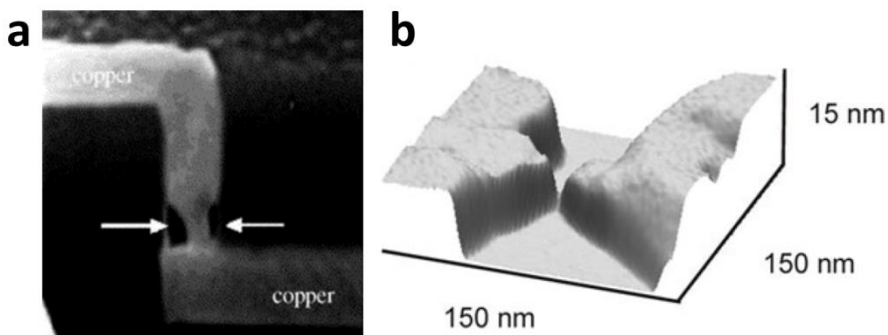


**Figure 1.1.** Consequences of electromigration. (a) Failure of vertical connector (via) between two copper wiring of the transistor, the arrows indicate the place of breakage<sup>15</sup>. (b) Nanogap formed from Pt bridge<sup>13</sup>.

In order to understand the mechanism of material transport under an applied electric field, many parameters should be considered: size of the structure, material, temperature, stress, microstructure (size of the grains, type of grain boundaries), surface effects<sup>16-18</sup>. Due to these complications up till now there is no general theory of electromigration and many questions remain.

Two approaches for electromigration phenomena explanation can be listed: atomistic approach (considering the motion of single atoms) and dislocation motion study. In this thesis we use the atomistic approach, which will be described in more details in the following section.

When a movement of groups of atoms is considered one can refer to dislocation movement<sup>19,20</sup>. In polycrystalline material grain boundaries (GB) act as pinning points for dislocations, resulting in their pile up under applied external stress (i.e. electrical field<sup>21</sup>). Grain size decrease results in higher needed external stress for dislocation movement through the material. This effect is known as grain boundary strengthening or Hall-Petch strengthening<sup>22-24</sup>. Grain boundary strengthening has a limit<sup>25</sup>. When the grain size diminishes till the size of dislocation (5-20 nm<sup>26</sup>), dislocations pile up is not possible. So, this approach can be implemented for a material containing relatively big grains, while for fine-grained structures the GB diffusion is considered.

### 1.1.2. Atomistic approach

In an atomistic approach, the electromigration process is the displacement of atoms from their crystal lattice positions, hence requiring atoms to overcome the crystal lattice energy barrier (energy of atom should reach the activation energy). Since atoms at the surface and at grain boundaries have a smaller binding energy, these atoms are most likely to be electromigrated.

The electromigration force ( $F_{em}$ ) on a single atom is assumed to be the sum of two terms: the electrostatic force ( $F_d$ ) and the wind force ( $F_w$ )<sup>27</sup> (Figure 1.2).

$$F_{em} = F_d + F_w. \quad (1.1)$$

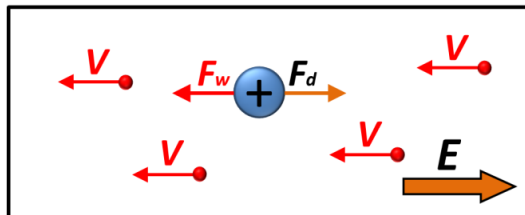


**Figure 1.2.** Schematic illustration of forces acting on atom under applied electric field  $E$ . Red dots refer to electrons.

The electrostatic force is the direct force on an atom or ion in a material due to an electric field. The concept of “wind force” was introduced by Skaupy<sup>28</sup> and became a key point in the basic understanding of electromigration. The wind force corresponds to the momentum transfer from the current carriers, i.e. electrons (electron-wind force) or holes (hole-wind force), to atoms in scattering processes<sup>7,29</sup>. Because atoms move under the electric field, they can be considered to have a temperature dependent effective charge ( $Z^*$ ) which can be derived from ballistic transport theory developed by Fiks<sup>27</sup>:

$$F_{em} = Z^* e E = (n_e \sigma_e l_e) e E, \quad (1.2)$$

where  $e$  is the fundamental charge,  $E$  is the applied electric field,  $n_e$  is the electron density,  $\sigma_e$  is the scattering cross section,  $l_e$  is the mean free path of electron.

### Electromigration-induced stress

If the electron wind force is bigger than the direct force, the effective charge is negative and atoms move from the cathode toward the anode side. Atomic flux due to electromigration ( $J_{em}$ ) can be calculated using the Nernst–Einstein equation<sup>30</sup>:

$$J_{em} = V c_a = \frac{D F_{em}}{kT} c_a = \frac{D Z^* e (\rho j)}{kT} c_a, \quad (1.3)$$

where  $V$  is the atomic drift velocity,  $c_a$  is the atomic concentration,  $D$  is the diffusivity,  $k$  is the Boltzmann’s constant,  $T$  is the temperature,  $\rho$  is the resistivity, and  $j$  is the current density. It should be noted, that resistivity of thin polycrystalline films is different from the bulk values. In thin films electron scattering on phonons, lattice imperfections (impurities, interstitials or vacancies), grain boundaries and surface/interface should be taken into account (more details will be given in Chapter 5).

Movement of atoms in a preferential direction leads to creation of regions with material depletion (near cathode side) and accumulation (near anode side). If atoms are depleted, a tensile stress develops, while atoms accumulation leads to compressive stress (Figure 1.3). In other words, electromigration-induced mass transport leads to a stress gradient development between cathode and anode sides of metallic wire. This stress gradient often referred as a back stress due to creation of a force which directs opposite to the electromigration force. When these forces equilibrate each other, the net atomic flux becomes zero. In such case, the formula derived by I. Blech and C. Herring can be written<sup>31</sup>:

$$Z^* e E = \Omega \frac{\partial \sigma}{\partial x}, \quad (1.4)$$

where  $\Omega$  is the atomic volume,  $\sigma$  is the back stress,  $x$  is the distance along the wire in the direction of electron flow.

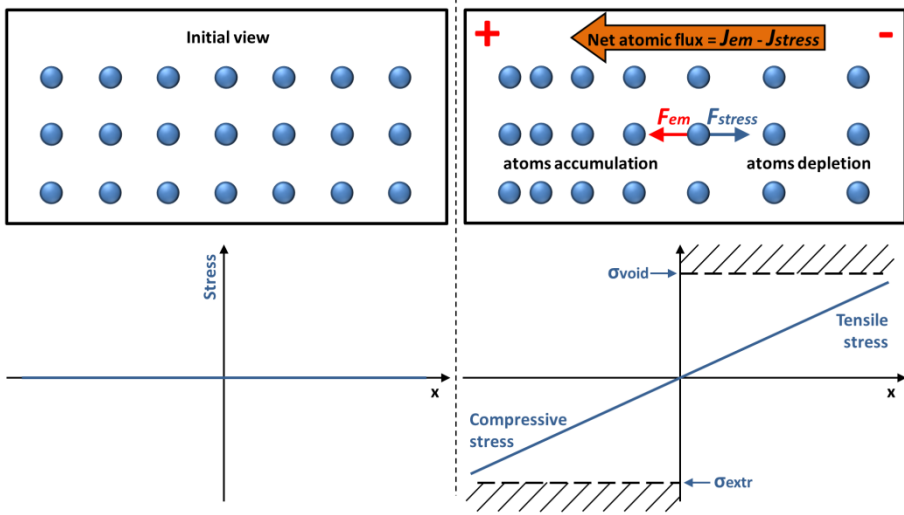


**Figure 1.3.** Electromigration-induced stress development.

If the equilibrium state is reached before voids nucleation or material extrusion occurs, the metallic line is prevented from a breakage. For “immortal” lines the product of the wire length and the applied current density ( $jL$ ) should be less than the threshold value derived from equation (1.4) as

$$(jL)_{threshold} = \frac{2\sigma_{void-extr}\Omega}{Z^*ep}, \quad (1.5)$$

where  $\sigma_{void-extr}$  is the stress required for voids nucleation or material extrusion,  $L$  is the total wire length.

By measuring the drift velocities of Al stripes on titanium nitride substrate, I. Blech<sup>2</sup> found the value of threshold-length product for Al at 350°C to be around 1260 A/cm. The threshold current can be increased by decreasing the sample temperature.

If  $(jL) > (jL)_{threshold}$ , voids form in the regions of outgoing atomic flux (Figure 1.4). They mainly nucleate at triple junctions (points where three grain boundaries meet each other and surface) or at the edge of the structure<sup>32-34</sup>. First voids will form at triple points formed with high energy grain boundaries<sup>35</sup>. Both electromigration force and surface tension drive the evolution of growth direction and shape change of voids<sup>36-39</sup>. If electromigration prevails a directional slit will form. But if surface tension is dominant over electromigration, the voids will have almost round shape (no preferential growth direction). Voids growth eventually leads to the breakage of metallic lines closer to the cathode side.

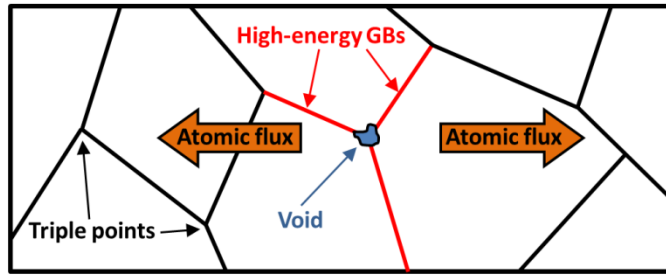


**Figure 1.4.** Schematic illustration of void nucleation at triple point.

### 1.1.3. Joule heating

During current passage through a conductor, the local temperature is increased. This effect (Joule heating) is named after James Prescott Joule who discovered this phenomenon in 1841. Heat accumulates due to electrons scattering on lattice atoms, so with a current increase, the amount of heat increases:

$$Q = I^2 R t, \quad (1.6)$$

where  $Q$  is the accumulated heat,  $I$  is the applied current,  $R$  is the sample resistance,  $t$  is the time.

The temperature of the metallic bridge will depend on the input energy due to the applied current and the rate of energy loss to the surroundings. If electrical contacts toward the bridge act as a heat sinks, the temperature profile has a bell-like shape with the highest temperature value in the middle of the bridge, approaching ambient temperature at the contacts (Figure 1.5). The presence of a temperature gradient leads to thermal stress development<sup>29,40</sup>, resulting in atomic flux from hot towards cold regions (thermomigration). If the electrical current is driven through a temperature gradient, a thermoelectrical effect occurs resulting in the shift of the maximum temperature depending on the electric current direction<sup>41,42</sup>. This effect is high in semiconductor materials.

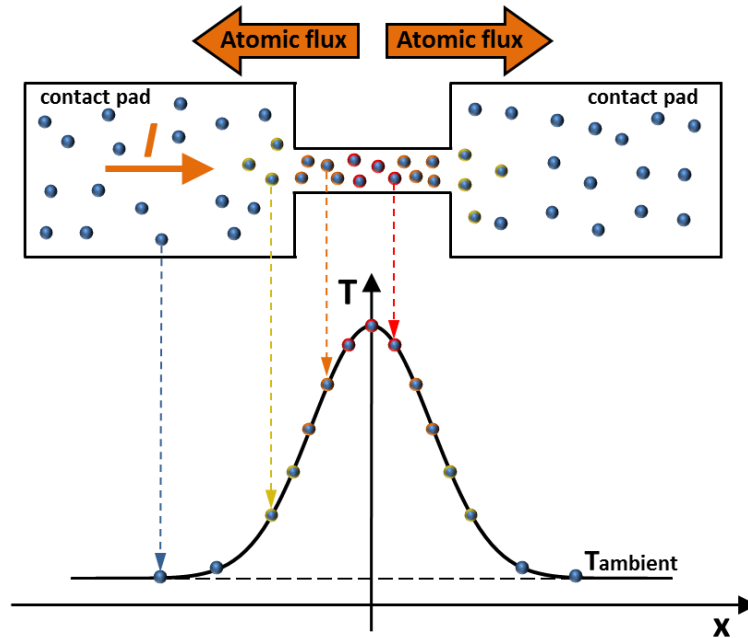


**Figure 1.5.** A temperature profile in metallic bridge forms due to Joule heating, the hottest regions marked with red, while the atoms with ambient temperature shown with blue. Contact pads act as heat sinks.

Another effect of Joule heating (or any other heating by an external heat source) on polycrystalline nanobridges is grains structure modification. First grain boundaries improvement occurs. It is a process of atoms reorganisation at the GBs in order to occupy positions of minimal energy, this leads to an increase of the GB's transmittance. Then the grain growth process starts<sup>43,44</sup>. With further temperature increase the grain growth process slows down due to grain boundary inhibition near the free surface and the film–substrate interface<sup>45,46</sup>. Also, due to the heating electromigration process starts easily. In other words, smaller current density is needed to displace atoms from their lattice positions at higher temperatures. More details are discussed in Chapter 6.

It should be mentioned that at high temperatures dewetting can be activated in thin films<sup>34</sup>. It is non reversible process of surface energy minimisation due to capillary forces resulting in islands formation. Dewetting happens below a film's melting temperature and the rate of it accelerates with decreasing film thickness.

#### 1.1.4. Accelerated electromigration experiments

In typical electromigration studies to study the ageing under application conditions the experiments last from several hours to many months. However, accelerated electromigration experiments are often implemented in order to gain useful information about failure mechanism in a reasonable time.

Median time to failure ( $MTF$ ) for the wire can be estimated using Black's equation <sup>47</sup>:

$$MTF = Aj^{-2} \exp\left(\frac{E_a}{kT}\right), \quad (1.7)$$

where  $A$  is a constant which contains the cross-sectional area of the film,  $j$  is a current density in  $A/cm^2$ ,  $E_a$  is an activation energy in  $eV$ ,  $k$  is the Boltzman's constant, and  $T$  is the film temperature in  $K$ .

From Black's equation it is clear that in order to minimise  $MTF$ , higher current densities or higher structure temperatures should be applied. To sum up, accelerated tests are made under much severe conditions than normal operating ranges. In this thesis electromigration was investigated inside the transmission electron microscope, so we shorten the experimental time to several minutes.

## 1.2. Motivation of research

The electromigration process is actively investigated for more than fifty years. Nowadays, the circuits failure tests, reliability tests, determination of different metals and semiconductors resistance toward the electromigration process are extensively explained in literature. But still no unique confirmed theory of electromigration is established, and there are a lot of open questions in fundamental level of process understanding.

In this thesis *in situ* transmission electron microscopy together with electrical measurements were used for investigations of electromigration in thin metallic nanobridges. This technique allows to obtain information about material under an applied electric field at the atomic level, helping in understanding the process dynamics.

In general, besides electromigration failure experiments, many different studies can be done implementing this technique. For instance, in molecule electronic device studies electrical properties of nanoparticles or molecules can be measured in combination with morphological changes visualisations. It can be also implemented in memory-switching devices investigations or in one of the hot topics of lithium-ion batteries.

## References

- 1 Gerardin, M. *Compt. Rend. Acad. Sci. Paris* **53** (1861).
- 2 Blech, I. A. Electromigration in Thin Aluminum Films on Titanium Nitride. *J Appl Phys* **47**, 1203-1208, doi:Doi 10.1063/1.322842 (1976).
- 3 Blech, I. A. & Kinsbron, E. Electromigration in Thin Gold-Films on Molybdenum Surfaces. *Thin Solid Films* **25**, 327-334, doi:Doi 10.1016/0040-6090(75)90052-8 (1975).
- 4 Jost, W. *Diffusion in solids, liquids, gases,* (Academic Press, 1952).
- 5 Seith, W. & Wever, H. *Z. Elektrochem.* **59** (1953).
- 6 Huntington, H. B. in *Diffusion in solids* (ed A.S. Nowick) (Academic Press, INC., 1975).
- 7 Ho, P. S. & Kwok, T. Electromigration in Metals. *Rep Prog Phys* **52**, 301-348, doi:Doi 10.1088/0034-4885/52/3/002 (1989).
- 8 Christou, A. *Electromigration and Electronic Device Degradation.* (John Wiley & Sons Inc, 1994).
- 9 Tan, C. M. & Roy, A. Electromigration in ULSI interconnects. *Materials Science and Engineering R* **58**, 1-75 (2007).
- 10 Park, H., Lim, A. K. L., Alivisatos, A. P., Park, J. & McEuen, P. L. Fabrication of metallic electrodes with nanometer separation by electromigration. *Appl Phys Lett* **75**, 301-303 (1999).
- 11 Gao, B., Osorio, E. A., Gaven, K. B. & van der Zant, H. S. J. Three-terminal electric transport measurements on gold nano-particles combined with ex situ TEM inspection. *Nanotechnology* **20**, 415207, doi:Doi 10.1088/0957-4484/20/41/415207 (2009).
- 12 Strachan, D. R. *et al.* Controlled fabrication of nanogaps in ambient environment for molecular electronics. *Appl Phys Lett* **86**, doi:Doi 10.1063/1.1857095 (2005).
- 13 Rudneva, M. *et al.* In-situ transmission electron microscopy imaging of electromigration in Pt nanowires. *Microscopy and Microanalysis* **11** (2012).
- 14 Prins, F. *et al.* Room-temperature stability of Pt nanogaps formed by self-breaking. *Appl Phys Lett* **94**, 123108, doi:Doi 10.1063/1.3109784 (2009).

- 15 Duesberg, G. S. *et al.* Ways towards the scaleable integration of carbon nanotubes into silicon based technology. *Diamond and Related Materials* **13**, 354–361 (2004).
- 16 Zschech, E. *et al.* Geometry and Microstructure Effect on EM-Induced Copper Interconnect Degradation. *Device and Materials Reliability, IEEE Transactions* **9**, 20-30 (2009).
- 17 Gonzalez, J. L. & Rubio, A. Shape effect on electromigration in VLSI interconnects. *Microelectronics Reliability* **37**, 1073–1078 (1997).
- 18 D'Heurle, F. M. Electromigration and Failure in Electronics: An Introduction *Proceedings of the IEEE* **59**, 1409-1418 (1971).
- 19 Hull, D. & Bacon, D. J. *Introduction to Dislocations*. (Elsevier Ltd, 2011).
- 20 Cottrell, A. H. *Theory of Crystal Dislocations*. (Routledge, 1964).
- 21 Suo, Z. Electromigration-Induced Dislocation Climb and Multiplication in Conducting Lines. *Acta metall. mater.* **42**, 3581-3588 (1994).
- 22 Hall, E. O. The deformation and ageing of mild steel. *Proc. Phys. Soc. Lond. B* **64**, 747-753 (1951).
- 23 Hall, E. O. *Yield Point Phenomena in Metals and Alloys*. (Plenium Press, 1970).
- 24 Petch, N. J. The cleavage of polycrystals. *J. Iron Steel Inst.* **174**, 25-28 (1953).
- 25 Chokshi, A. H., Rosen, A., Karch, J. & Gleiter, H. On the validity of the Hall–Petch relationship in nanocrystalline materials. *Scripta Metall.* **23**, 1679–1684 (1989).
- 26 Nieh, T. G. & Wadsworth, J. Hall-Petch Relation in Nanocrystalline Solids. *Scripta Metallurgica et Materialia* **25**, 955-958 (1991).
- 27 Fiks, W. B. On the mechanism of the mobility of ions in metals. *Sov. Phys. - Solid State* **1**, 14-28 (1959).
- 28 Skaupy, F. Electrical conduction in metals. *Verband Deutscher Physikalischer Gesellschaften* **16**, 156-157 (1914).
- 29 Durkan, C. *Current at nanoscale. An introduction to Nanoelectronics.*, (2007).
- 30 Sham, L. J. Microscopic Theory of Driving Force in Electromigration. *Phys Rev B* **12**, 3142-3149, doi:DOI 10.1103/PhysRevB.12.3142 (1975).
- 31 Blech, I. A. & Herring, C. Stress Generation by Electromigration. *Appl Phys Lett* **29**, 131-133, doi:Doi 10.1063/1.89024 (1976).

- 32 Srolovitz, D. J. & Safran, S. A. Capillary instabilities in thin films. I. Energetics. *J App Phys* **60**, 247-254 (1986).
- 33 Genin, F. Y., Mullins, W. W. & Wynblatt, P. Capillary instabilities in polycrystalline metallic foils: experimental observations of thermal pitting in nickel. *Acta metall. mater.* **42**, 1489-1492 (1994).
- 34 Thompson, C. V. Solid-state dewetting of thin films. *Annu. Rev. Mater. Res.* **42**, 399-434 (2012).
- 35 Presland, A. E. B., Price, G. L. & Trimm, D. L. Kinetics of hillock and island formation during annealing of silver films. *Prog. Surf. Sci.* **3**, 63-96 (1972).
- 36 Suo, Z., Wang, W. & Yang, M. Electromigration instability: Transgranular slits in interconnects. *Appl Phys Lett* **64**, 1944-1946 (1994).
- 37 Wang, W. & Suo, Z. A simulation of electromigration-induced transgranular slits. *J App Phys* **79**, 2394-2403 (1996).
- 38 Kraft, O., Bader, S., Sanchez, J. E. & Arzt, E. Observation and Modellig of Electromigration-Induced Void Growth in Al-based interconnects. *Mat. Res. Soc. Symp. Proc.* **308**, 267-272 (1993).
- 39 Kraft, O. & Arzt, E. Electromigration mechanisms in conductor lines: Void shape changes and slit-like failure. *Acta Materialia* **45**, 1599-1611, doi:Doi 10.1016/S1359-6454(96)00231-5 (1997).
- 40 Chen, C., Tong, H. M. & Tu, K. N. Electromigration and Thermomigration in Pb-Free Flip-Chip Solder Joints. *Annual Review of Materials Research* **40**, 531-555 (2010).
- 41 Chih Chen, C., Hsiao, H.-Y., Chang, Y.-W., Ouyang, F. & Tu, K. N. Thermomigration in solder joints. *Materials Science and Engineering R* **73**, 85-100 (2012).
- 42 Bakan, G., Khan, N., Silva, H. & Gokirmak, A. High-Temperature Thermoelectric Transport at Small Scales: Thermal Generation, Transport and Recombination of Minority Carriers. *Scientific Reports* **3**, 2724 (2013).
- 43 Thompson, C. V. Structure evolution during processing of polycrystalline films. *Annual Review of Materials Science* **30**, 159-190, doi:DOI 10.1146/annurev.matsci.30.1.159 (2000).
- 44 Holm, E. A. & Foiles, S. M. How Grain Growth Stops: A Mechanism for Grain-Growth Stagnation in Pure Materials. *Science* **328**, 1138-1141, doi:DOI 10.1126/science.1187833 (2010).

- 45 Burke, J. E. & Turnbull, D. Recrystallization and Grain Growth. *Progress in Metal Physics* **3**, 220-292, doi:Doi 10.1016/0502-8205(52)90009-9 (1952).
- 46 Rost, M. J., Quist, D. A. & Frenken, J. W. M. Grains, Growth, and Grooving. *Phys. Rev. Lett* **91**, 4 (2003).
- 47 Black, J. R. Electromigration - a Brief Survey and Some Recent Results. *Ieee Transactions on Electron Devices* **Ed16**, 338-&, doi:Doi 10.1109/T-Ed.1969.16754 (1969).

## Thesis outline

This thesis contains 7 Chapters. **Chapter 1** is an introduction chapter which gives an overview of electromigration process. Different theoretical approaches for understanding the underlying forces which affect the material transfer under an applied electric field are discussed. **Chapter 2** tells to the reader about experimental technics implemented in this study with the main focus on *in situ* transmission electron microscopy describing the used modes of imaging and diffraction and *in situ* holders. Big part of this chapter is devoted to the details of sample fabrication for the experiments. **Chapter 3** shows scanning transmission electron microscopy imaging with high angle annular dark field detector as a powerful mode to visualize electromigration-induced thickness variations in polycrystalline films. In this mode the diffraction contrast can be further minimized using a tilt series. This imaging technique shown to be implemented in measurements of nanogaps shape formed by electromigration. In **Chapter 4** we investigated the dynamic of reversible electromigration process in Pd–Pt nanobridges. Material transport is shown to be from the cathode towards the anode side, indicating a negative effective charge. Upon a change of the electric field the direction of material transport reverses, leading to the initial configuration after one full cycle. This reversible electromigration is shown to be the basis of a memristor. **Chapter 5** and **Chapter 6** are devoted to investigations of the nanobridges under both dynamic conditions, i.e. heating and electric current passage. Initially, in Chapter 5 the origin of increased resistivity in Pt nanobridges is discussed. By correlation of resistance changes with morphological transformations in polycrystalline Pt nanobridges during the substrate heating, different impacts in the total nanobridge resistance are investigated. We considered the total resistance raise due to electron scattering on phonons, grain boundaries, surface and point defects. Chapter 6 shows results of electromigration in Pt nanobridges at different substrate temperatures (from liquid nitrogen to 660 K). Despite the surrounding temperatures, electromigration experiments show the same tendency: Material transport occurs from the cathode to the anode side, which can be explained by the electron-wind force. In all cases the bridges break due to the neck formation closer to the cathode side. Higher surrounding temperatures enhance the voids formation, leading to lower value of power needed to break the nanobridge. **Chapter 7** gives some suggestions for a future work, showing the possibility of *in situ* TEM implementation for nanoparticles observations under both dynamic conditions, i.e. heating and current passage.



---

# Chapter 2

---

## Experimental Technics and Sample Fabrication

This chapter is devoted to the experimental technics applied in this study. First of all, a short introduction in transmission electron microscopy is given with the focus on imaging, diffraction and scanning modes. Also, a couple of paragraphs devoted to atomic force microscopy, which was implemented for obtaining a 3D profiles of investigated structures. The second section shows an overview of clean room sample processing for dynamic, *in situ* experiments. The last, third section, shows the experimental setup which allows to perform *in situ* electrical and heating TEM experiments.

## 2.1. Investigation tools

### 2.1.1. Transmission electron microscopy (TEM)

(Most of the text in this section has been adapted from references <sup>1,2</sup>).

#### Brief history

The story of transmission electron microscopy starts in 1858 when Julius Plucker first observed the electron. He found a new phenomenon: a fluorescent patch was seen opposite to the cathode in a discharge tube. At that time the origin of "cathode rays" was unknown. Only in 1897 J. J. Thomson showed that "cathode rays" are charged particles. After, in 1925, Louis de Broglie postulated the wave-like behaviour of electrons, which was confirmed with electron-diffraction experiments two years later <sup>3</sup>.

In 1932 electron lenses were developed and the first idea of an electron microscope was proposed by M. Knoll and E. Ruska <sup>4, 5</sup>. After that different companies (Hitachi, JEOL, Phillips) started to build commercial microscopes. The important step for material scientists was done by Bollman and Hirsch in the mid-50's when they developed techniques for thinning metal foils to electron transparency <sup>6</sup>.

Nowadays TEM is one of the most powerful tools for material investigation on atomic level. Using aberration correction it is possible to achieve 0.5Å resolution <sup>7</sup>. If the arrangement of individual atomic columns in crystals can be visualised, the technique is called high resolution TEM (HRTEM). TEM allows one to determine not only morphology and crystal structure of specimens, but also their chemical composition (to do microanalysis).

#### Imaging and diffraction

TEM has many similarities with the construction of optical microscope. Both machines have three main parts: 1) the illumination system; 2) the objective lens/stage (sample area); and 3) the imaging system. As an illumination system in case of TEM the electron gun is implemented shaped with the electromagnetic lenses, while the visible light is used as a source in optical microscope shaped with glass lenses. The difference in surrounding pressure (high vacuum in case of TEM and atmosphere for optical microscope) is explained by the electrons scattering on atmosphere particles and as a result the signal distortion and attenuation. See summary in Table 2.1.

	TEM	Optical microscope
Illumination system	Electron gun	Visible light
Lenses	Electromagnetic lenses	Glass lenses
Surrounding	High vacuum	Atmosphere

**Table 2.1.** Comparison of TEM and optical microscope construction.

Figure 2.1 shows the two basic operation modes of TEM – imaging and diffraction modes<sup>8,9</sup>. In both cases specimen is illuminated with the parallel beam, formed by electron beam shaping with the system of Condenser lenses and Condenser aperture. After interaction with the sample, on the exit surface of the specimen two types of electrons exist – unscattered (which will correspond to the bright central beam on the diffraction pattern) and scattered electrons (which change their trajectories due to interaction with the material).

In Imaging mode an objective aperture can be inserted in a back focal plane (BFP) of objective lens (where diffraction spots are formed). If using the objective aperture an area with the central beam is selected (the rest signal is blocked), a so-called bright field image (BF image) is obtained. If we select an area excluding the central beam a so-called dark-field image (DF image) is made. Than selected signal is magnified and projected on a screen (or on a camera) with the help of intermediate and projector lenses. Image of the sample is received.

In Diffraction mode a selected area aperture is used to determine the specimen area from which the signal will be displayed, or the beam is focussed to a small spot. By changing the strength of intermediate lens the diffraction pattern is projected on a screen. Diffraction is a very powerful tool for doing a crystal structure determination and crystal orientation determination.

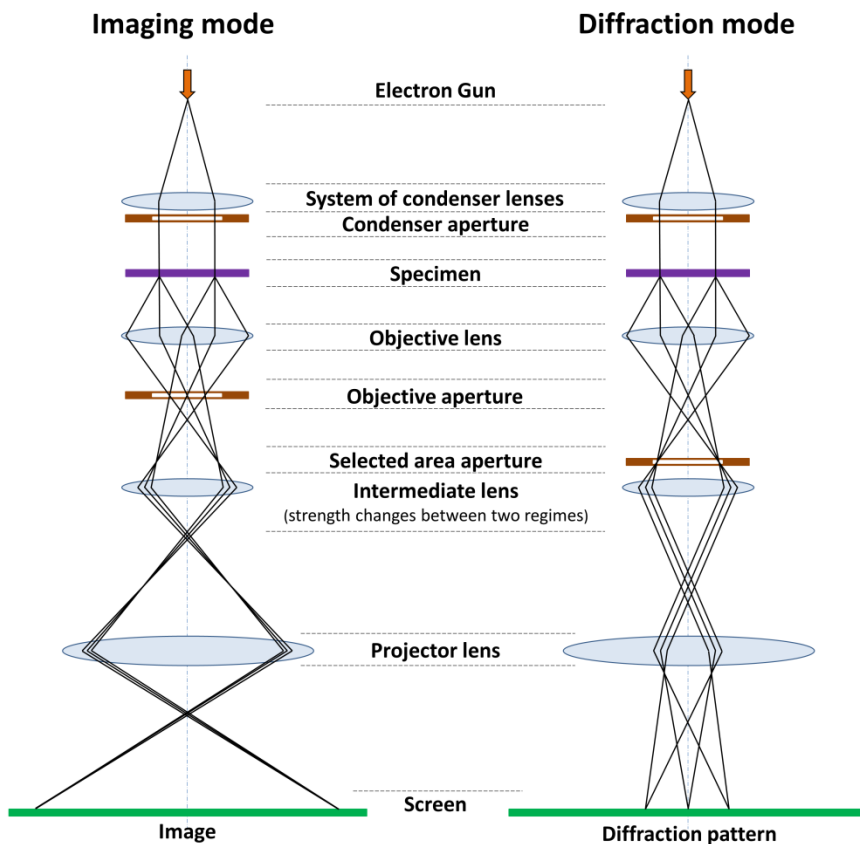


**Figure 2.1.** Schematic view of imaging and diffraction modes in TEM.

### Scanning TEM (STEM)

In the previous section the parallel beam mode of illumination system was described. The second option to operate the illumination system is convergent beam (Figure 2.2). In this case, the beam is focused on top of the Specimen (with the typical Spot Size 0.05–0.2 nm), and using the Deflection coils it is scanned along the sample (scanning transmission electron microscopy)<sup>10</sup>. It should be noted that illumination system constructed in a way that at each point sample illuminated with the beam parallel to the optical axis. The exit electron waves collected with the Objective lens on the STEM detector. Typically, high-angle scattered electrons are collected with the annular dark-field detector (ADF) and after the computer processing the DF image is displayed.

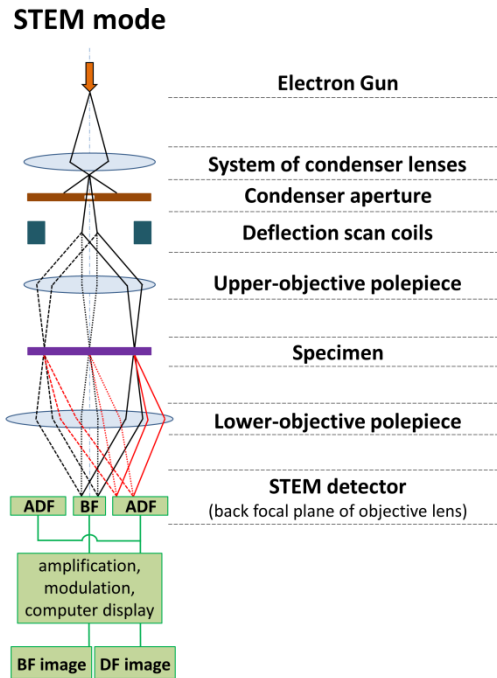


**Figure 2.2.** Schematic view of STEM mode.

## Contrast

The contrast between two adjacent areas in a TEM image can be defined as the difference in the electron densities in image plane. Due to the scattering of the incident beam by the sample, the amplitude and phase of the electron wave change, which results in *amplitude contrast* and *phase contrast*, correspondingly<sup>11,12</sup>. Most of images have both contrast components.

Amplitude-contrast is obtained due to removal of some electrons before the image plane. During their interaction with the specimen some of electrons will be lost due to absorption, or due to scattering at very high angles beyond the physical limitation of microscope or are blocked by the objective aperture. While the first two losses are due to the specimen and microscope construction, the objective aperture can be used by operator to enhance the contrast.

Figure 2.3(a-b) shows a TEM image and the corresponding diffraction pattern of Pt polycrystalline film taken without an objective aperture. In order to enhance the contrast in the TEM image the number of scattered beams as visible in the diffraction pattern should be reduced. This can be done by selecting a certain area in the diffraction plane like only the central beam or a diffracted beam, or combinations of beams with objective aperture to form BF (Figure 2.3(c)) in case the central beam is included or DF (Figures 2.3(d-e)) images in case

the central beam is blocked. DF images (Figures 2.3(d-e)) are obtained using the diffracted beams indicated in diffraction pattern with circles (Figure 2.3(b)). Grains from which electrons are scattered into these diffraction spots appear brighter. More details about diffraction contrast formation are given further.

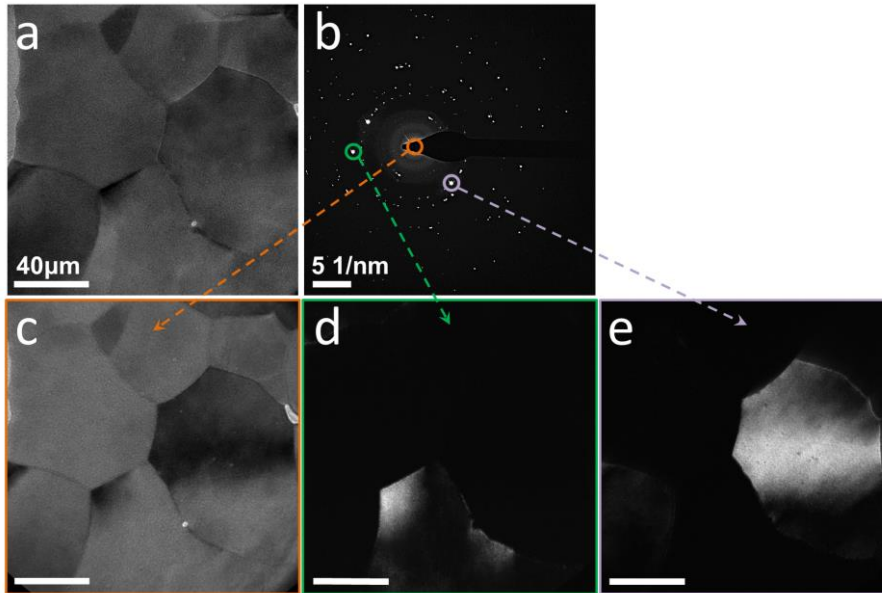


**Figure 2.3.** (a) TEM image of Pt polycrystalline film and correspondent diffraction pattern (b). BF TEM (c) and DF TEM (d-e) images taken with inserted 50  $\mu\text{m}$  objective aperture at places indicated with circles in diffraction pattern (b).

There are two types of amplitude contrast – *mass-thickness* and *diffraction contrast*. Figure 2.4 shows schematic representation of the mechanisms of both contrasts formation in BF TEM mode. First, let's consider mass-thickness contrast. When the beam illuminates two neighbouring areas with low mass (or thickness) and high mass (or thickness), the heavier region scatters electrons at bigger angles. These strongly scattered electrons are blocked in BF TEM mode by objective aperture. As a result, heavier regions appear darker in BF images (have low intensity). It should be noted, that mass-thickness contrast is most important for non-crystalline, amorphous materials.

Diffraction contrast (see Figure 2.4, right) occurs due to a specific crystallographic orientation of a grain. In such a case the crystal is in a so-called Bragg condition, whereby atomic planes are oriented in a way that there is a high probability of scattering. Thus diffraction contrast provides information on the orientation of the crystals in a polycrystalline sample. Examples are given in Figure 2.3. Note that in case diffraction contrast exists, the contrast cannot be interpreted as due to mass or thickness variations.

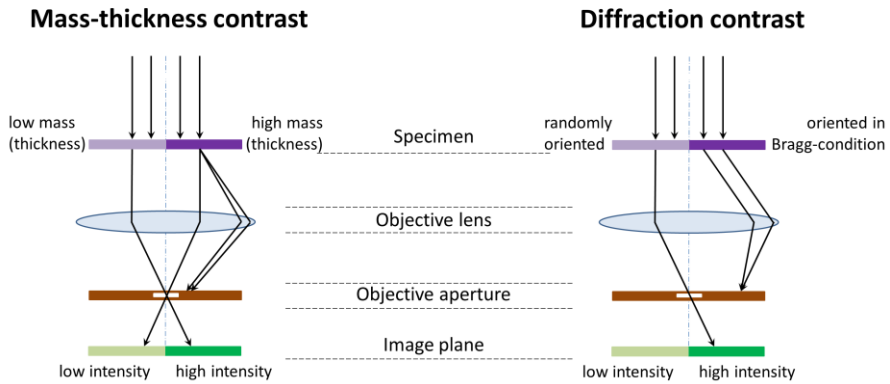


**Figure 2.4.** Schematic representation of mass–thickness and diffraction contrasts formation in BF TEM mode.

In a perfect electron microscope without aberrations the phase variations in the electron wave cannot be seen at zero focus: there is no contrast variation in the image plane. Figure 2.5(a) shows an image of a graphene sample (which is almost pure phase object due to its thinness and because C is a weakly scattering atom) under such a condition<sup>13</sup>. Only by including an aberration (in this case a defocus) one can transfer phase information into amplitude information; therefore variations in the thickness of the graphene layer can be observed (Figure 2.5(b)). Note that the contrast in the defocused image is still poor and a much better contrast is obtained by removing the central beam. Under this DF condition (Figure 2.5(c)) the small holes present in the graphene are clearly visible.

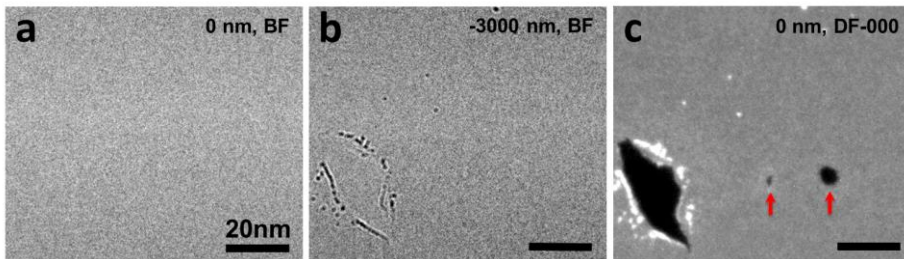


**Figure 2.5.** The same area of single layer graphene in which three holes (the two smaller ones are indicated with red arrows) were made with the electron beam. (a) and (b) BF TEM images at 0 focus and at -3000 nm defocus, showing the effect of focus on the contrast. (c) DF TEM image in which only the central beam is removed from the imaging. Note that the two small holes are only barely visible in the BF image taken at -3000 nm and not at all in the BF image taken at 0 focus<sup>13</sup>.

In STEM mode scattered beams are selected by using different detectors (BF or ADF, by varying the camera length,  $L$ , different collection angles of STEM detector (a ring detector) can

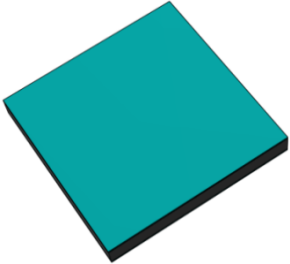
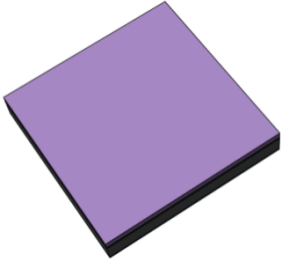
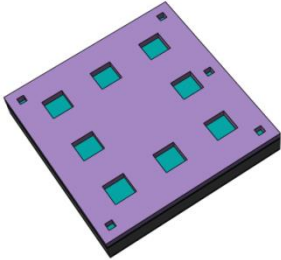
be selected) rather than apertures. In this case one can select the preferred contrast by choosing the a specific camera length / ring detector combination.

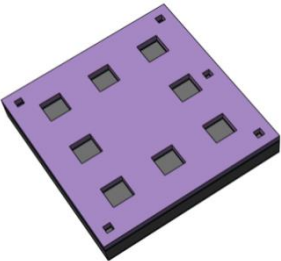
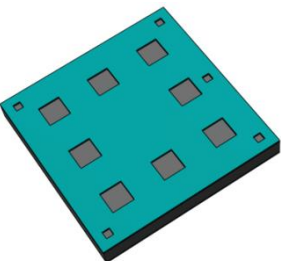
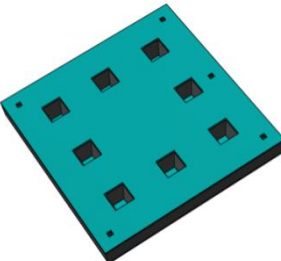
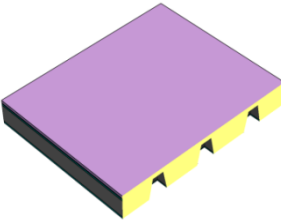
### **2.1.2. Atomic force microscopy (AFM)**

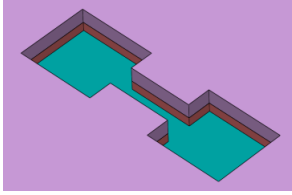
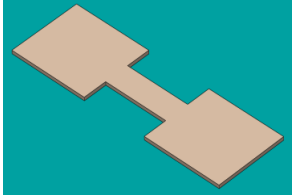
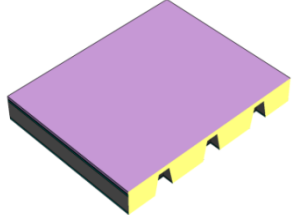
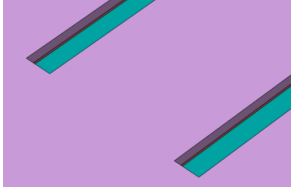
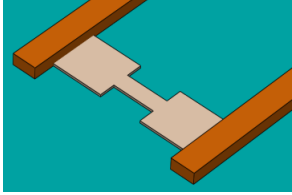
Atomic force microscopy (AFM) can be used for investigation of 3D sample topography, surface charge, capacity, magnetic properties, etc. The basic principal of AFM is based on the interaction between the sharp tip of cantilever and surface atoms. Two scanning regimes can be implemented: constant force or constant height regimes. During scanning, the tip–surface interaction leads to the cantilever deflection, which is measured by an optical system. The signal measured with a photodetector is recorded for further analysis and used to adjust the position of the cantilever at the next scan step. Depending on the distance between tip and surface, three modes can be concerned: contact, non-contact or tapping modes. The vertical distance resolution in AFM is around an angstrom, while lateral resolution is determined by the shape of cantilever tip<sup>14</sup>.

## **2.2. Sample fabrication / Clean room processing**

All chips used in the described in this thesis experiments were made using Kavli Nanolab Delft facilities (<http://www.ns.tudelft.nl/nanofacility>). Step by step procedure of fabrication process is shown in Table 2.2. In general, there are three main steps: 1) substrate making (including wafer preparation and obtaining Si<sub>3</sub>N<sub>4</sub> windows); 2) making investigated structures (using two steps of e-beam lithography for bridges and contacts); 3) single chip modification after substrate cleaving (optional membrane thinning or adding a protective coverage layer). Following table corresponds to the preparation of the chips shown in Chapters 3, 4 and 7. For chips investigated in Chapters 5 and 6 the flat–centre heaters were used as substrates.

Fabrication step	Schema	Description of technical details
Preparation		<ul style="list-style-type: none"> <li>➤ Using low-pressure chemical vapour deposition (LPCVD) 100-nm-thick <math>Si_3N_4</math> layers are grown on both sides of double-sided polished (400 nm) <i>Si wafer</i>;</li> <li>➤ AZ5214 resist spin coating for protection; rotation speed: 1000 rotation per minute (rpm), time: 55 s; baking (110°C, 10 min);</li> <li>➤ Wafer <i>dicing</i> on 14×14 mm<sup>2</sup> squares (substrates);</li> </ul> <p><i>*samples are received at that stage</i></p> <ul style="list-style-type: none"> <li>➤ Resist removal in nitric acid (15 min), rinsing in water;</li> </ul>
Windows and markers making		<ul style="list-style-type: none"> <li>➤ Positive resist coating (500-nm-thick): PMMA 950k <sup>(1)</sup>, 7% in anisole <sup>(2)</sup>, rotation speed: 5000 rpm, time: 55 s; baking (175°C, 60 min);</li> </ul> <p>* only one resist layer is used at that step due to no demand to high accuracy;</p>
		<ul style="list-style-type: none"> <li>➤ Electron beam lithography (5000+ Leica EB pattern generator), pattern creation in DesignCad 3D Max 16 (Figure 2.6), layout file is done with LayoutBEAMER program;</li> </ul> <p>1<sup>st</sup> step (resolution 120 nm) – windows and markers;</p> <ul style="list-style-type: none"> <li>➤ Resist development (removal from exposed areas): rinsing in 1+3 methyl isobutyl ketone (MIBK) ÷ isopropyl alcohol (IPA, 2-Propanol) (70 s); IPA (50 s); drying with the compressed air;</li> </ul>

		<ul style="list-style-type: none"> <li>➤ <i>Reactive ion etching (RIE)</i> (Leybold F1) of opened <math>\text{Si}_3\text{N}_4</math>: <math>\text{CHF}_3/\text{Ar}</math> with gas flow 25/25 sccm, pressure 6.7 <math>\mu\text{bar}</math>, forward power 50 W, etching speed 20nm/min, etching 5 min;</li> </ul>
		<ul style="list-style-type: none"> <li>➤ <i>Resist removal</i> in hot acetone (55°C, 10 min), rinsing in IPA; drying with the compressed air;</li> </ul>
		<ul style="list-style-type: none"> <li>➤ <i>KOH etching</i> – anisotropic Si removal from the areas not protected by <math>\text{Si}_3\text{N}_4</math>. Samples are placed in solution (100 gram KOH + 200 gram water) at 85°C for 6 hours;</li> <li>➤ <i>Sample cleaning</i> with water, acetone and IPA;</li> </ul>
<p>Metallic bridges making (shown in blue in Figure 2.1 (c, d))</p>	 <p>Chip cross section</p>	<ul style="list-style-type: none"> <li>➤ <i>Positive resist coating</i> with two layers; double layer is used to improve resist sensitivity which is necessary to produce 100-nm-wide structures.</li> </ul> <p>1<sup>st</sup> layer (300 nm): PMMA/MMA (17.5%)<sup>(3)</sup>, 8% in ethyl-l-lactate, rotation speed: 3000 rpm, time: 55 s; baking (175°C, 15 min);</p> <p>2<sup>nd</sup> layer (130 nm) PMMA 950k, 3% in anisole, rotation speed: 3000 rpm, time: 55 s; baking (175°C, 15 min);</p>

		<ul style="list-style-type: none"> <li>➤ Electron beam <i>lithography</i></li> <li>2<sup>nd</sup> step (resolution 5 nm) – bridges;</li> <li>➤ <i>Resist development</i>;</li> </ul>
		<ul style="list-style-type: none"> <li>➤ Desired <i>metal deposition</i> with the speed 1 Å/s</li> <li>(Pt deposition on Temescal FC-2000 e-beam evaporator,</li> <li>Ni, Pd – on Leybold L560 e-beam evaporator);</li> <li>➤ <i>Resist removal</i>;</li> </ul>
<p>Contacts making (shown in purple in Figure 2.1)</p>	 <p>Chip cross section</p>	<ul style="list-style-type: none"> <li>➤ Positive <i>resist coating</i> (500 nm + 80 nm): PMMA/MMA (17.5%), 8% in ethyl-l-lactate, rotation speed: 1000 rpm, time: 55 s; baking (175°C, 10 min);</li> <li>PMMA 950k, 2% in anisole, rotation speed: 1000 rpm, time: 55 s; baking (175°C, 20 min);</li> </ul>
		<ul style="list-style-type: none"> <li>➤ Electron beam <i>lithography</i></li> <li>3<sup>rd</sup> step (resolution 20 nm – fine contact details,</li> <li>resolution 120 nm – coarse contact details);</li> <li>➤ <i>Resist development</i>;</li> </ul>
		<ul style="list-style-type: none"> <li>➤ <i>Metal deposition</i> on Temescal FC-2000 e-beam evaporator:</li> <li>3 nm Cr as an adhesion layer with the speed 0.5 Å/s;</li> <li>97 nm Au with the speed 2 Å/s;</li> </ul>
<p>Substrate cleaving</p>		<ul style="list-style-type: none"> <li>➤ Manual <i>sample cut</i> on separate chips using a diamond pan;</li> </ul>

Membrane thinning (optional)		➤ <i>RIE</i> of $\text{Si}_3\text{N}_4$ from the back side. The membrane thickness of 20 nm was obtained in order to get higher resolution in TEM;
Protection layer deposition (optional)		➤ <i>Atomic layer deposition (ALD)</i> of $\text{Al}_2\text{O}_3$ for sample protection from oxidation ( $300^\circ\text{C}$ , $3 \times 10^{-6}$ torr).

**Table 2.2.** Steps of sample fabrication process.

<sup>(1)</sup> PMMA 950k – polymethyl methacrylate with molecular weight 950 000. In general, resist with this big molecular weight dissolves slower in a solvent developer, but provides higher contrast between the exposed and unexposed areas. As a result, high molecular weight PMMA is typically used for creation high resolution structures<sup>15</sup>.

<sup>(2)</sup> Anisole is used as a solvent for PMMA.

<sup>(3)</sup> MMA – methyl methacrylate, PMMA/MMA (17.5%) is a copolymer of PMMA with 17.5% MMA. This copolymer has molecular weight equal to PMMA 100k.

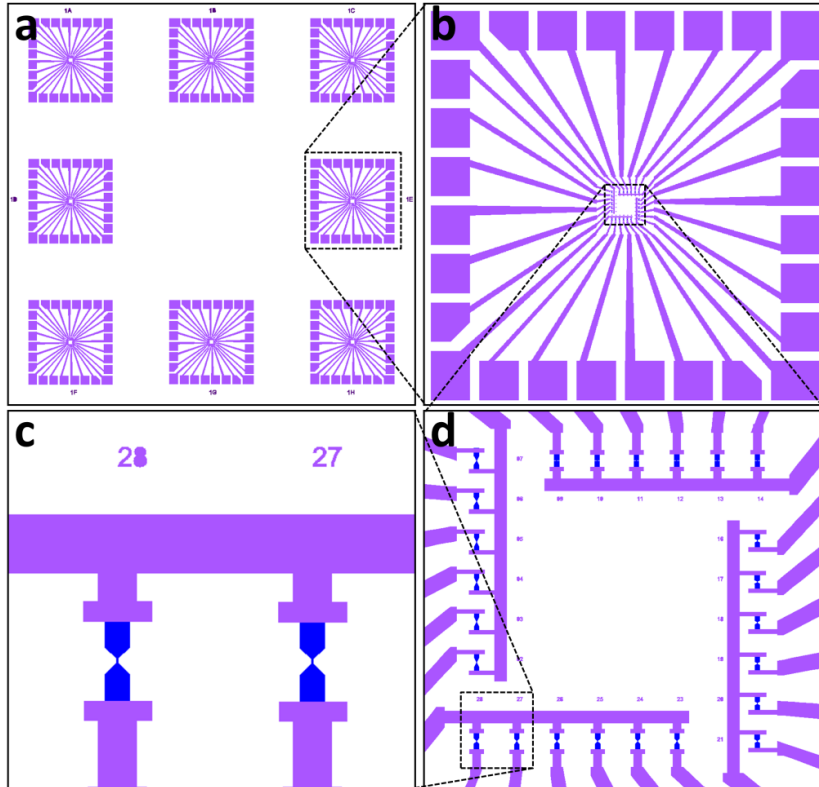


**Figure 2.6.** Pattern for electron beam lithography created in DesignCad 3D Max 16. One single structure (a) contains 8 chips (b), each of which has 24 bridges (shown in blue) with the Au leads (shown in purple) (c, d).

### 2.3. *In situ* TEM experiments

Conventional TEM is a very powerful characterisation tool for a thorough understanding of stable sample structure and composition at atomic level in vacuum conditions at ambient temperature. But *ex situ* experiments allow to investigate only the beginning and ending sample state, while the modification process is done separately. Such studies leave many open questions about the time of transformations, their start and kinetics. Also the environment change (change of pressure, oxidation while removing/inserting from/to the microscope) can play a crucial role.

In order to understand the dynamic of sample change under various external conditions, i.e. heating<sup>16-18</sup>, cooling<sup>19-21</sup>, interaction with reactive environment<sup>22-24</sup>, electrical bias applying<sup>25-27</sup>, mechanical deformations<sup>28-30</sup>, *in situ* microscopy has to be implemented. *In situ* experiments have two important components: external stimulus and real time observations<sup>31,32</sup>. To apply different external stimulus inside the TEM special holders are needed, which is

the most challenging part. For real time observations a fast recording system is required. Using a combination of microelectromechanical systems (MEMS) based devices and special TEM holders, the real time changes in a specimen can be visualised with high stability. In this thesis electrical bias applying, cooling and heating conditions were discussed. Experiments were performed using a FEI Titan microscope operating at 300 keV.

### 2.3.1. Electrical measurements

#### Holder

Figure 2.7 shows the electromigration holder, built in-house. It can be cooled to about 100 K by placing connected to the holder copper wires in a dewar filled with liquid nitrogen. The holder has eight separate electrical lines inside the tube ending with the eight contacts for performing electrical measurements from one side and electrical connector from another. The inset in Figure 2.7 shows the tip of the holder with the chip mounted in it. The chip with nanobridges (like shown in Figure 2.6) is fixed onto an  $\text{Al}_2\text{O}_3$  chip carrier using conductive tape and connected with it by means of the standard wire bonding technique.

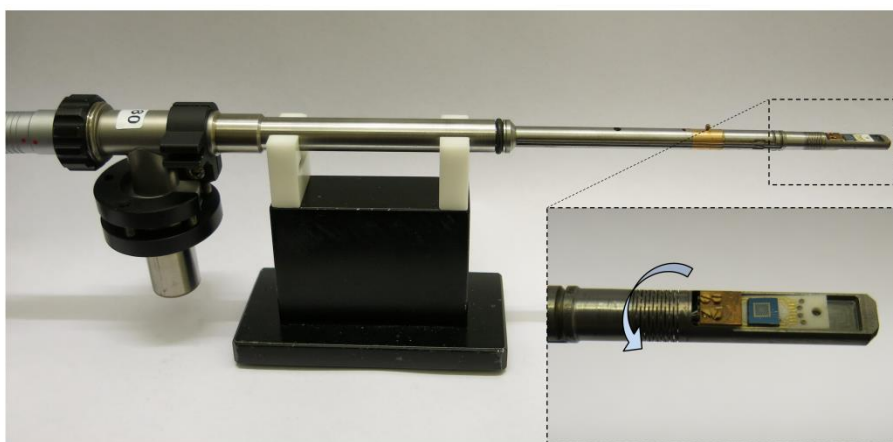


**Figure 2.7.** Electromigration holder for *in situ* experiments.

Through the connector using the copper shielded cable the holder is attached to electrical measurements setup.

## Electrical measurements setup

The electrical measurements setup consist of four parts: Matrix module, IVVI rack, ADwin-GOLD module and PC (Figure 2.8). The holder is connected to the Matrix module; this module has 24 ports, 8 of them correspond to the contacts from the holder. Measurement electronics setup (IVVI rack<sup>33</sup>) allows one to send and receive electrical signals to and from the experimental structure. It contains several modules: I/V source for V-I or I-V measurements, input and output modules. These modules are inserted in a shielded rack, battery-operated and isolated in order to reduce interference signals and noise. IVVI rack is connected with the ADwin-GOLD<sup>34</sup> to a PC, which allows to operate the experiment with the LabVIEW program. In our experiments, current was measured while applying voltage to investigated structures.

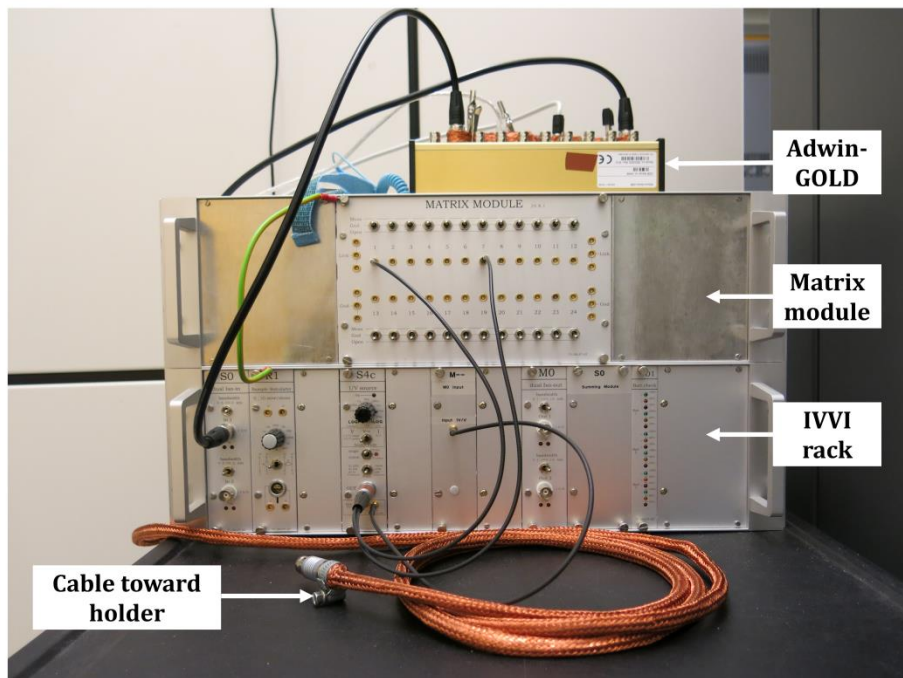


**Figure 2.8.** Electrical measurements setup.

### 2.3.2. Heating experiments

#### Holder

Figure 2.9 shows the heating holder, built in-house. The tip of it contains 4 pins, which are placed on the MEMS based heater (inset in Figure 2.9). Details of the MEMS heater preparation are reported elsewhere <sup>35</sup>. Four electrical lines go inside the holder to the connector. Connector is attached with the cable to the heating controller in order to set the temperature using the heating software. The heaters are calibrated with a pyrometer beforehand. The accuracy of temperature setting is  $< 5\%$  <sup>36</sup>. During the heating experiments drift can be diminished to approximately 0.1 nm/min due to localised heating and low power dissipation (several mW).

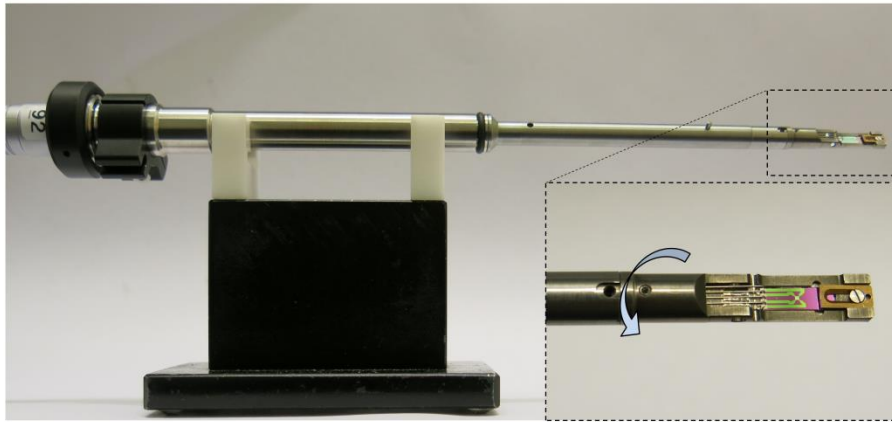


**Figure 2.9.** Heating holder for *in situ* experiments.

### 2.3.3. Joint electrical – heating experiments

In order to perform experiments under both dynamic conditions, i.e. heating and voltage applying, systems explained in sections 2.3.1 and 2.3.2 should be combined. The holder for electrical measurements was used with chips contained bridge and heating spiral (for details see Chapters 5 and 6). Four contacts corresponded to the heater spiral are connected from the Matrix module via adaptor box with the heating controller. Contacts for electrical measurements connected to the IVVI rack as in normal electrical measurements.

## References

- 1 Hawkes, P. W. in *Advances in imaging and electron physics* Vol. 123 1-23 (Elsevier Science, 2002).
- 2 Williams, D. B. & Carter, C. B. *Transmission Electron Microscopy*. (2009).
- 3 de Broglie, L. Researches on the quantum theory. *Ann. Phys.* **3**, 22-128 (1925).
- 4 Knoll, M. & Ruska, E. Electron Microscope. *Z. Phys.* **78**, 318-339 (1932).
- 5 Ruska, E. The development of the electron microscope and of electron microscopy. *Reviews of Modern Physics* **59**, 627-638 (1987).
- 6 Hirsch, P. B., Howie, A., Nicholson, R. B., Pashley, D. W. & Whelan, M. J. *Electron Microscopy of Thin Crystals*. (Krieger Huntington NY, 1977).
- 7 Kisielowski, C. & al., e. Detection of single atoms and buried defects in three dimensions by aberration-corrected electron microscope with 0.5-Å information limit. *Microscopy and Microanalysis* **14**, 469-477 (2008).
- 8 Williams, D. B. & Carter, C. B. in *Transmission Electron Microscopy* Vol. 1 Ch. 9, 141-158 (2009).
- 9 Cowley, J. M. *Diffraction Physics*. (Elsevier, 1995).
- 10 Williams, D. B. & Carter, C. B. in *Transmission Electron Microscopy* Vol. 1 Ch. 9, 158-161 (2009).
- 11 Williams, D. B. & Carter, C. B. in *Transmission Electron Microscopy* Vol. 3 Ch. 22, 371-403 (2009).
- 12 Thomas, J. & Gemming, T. in *Analytical Transmission Electron Microscopy* 115-137 (Springer, 2014).
- 13 Zhang, C., Xu, Q., Peters, P. J. & Zandbergen, H. The use of a central beam stop for contrast enhancement in TEM imaging. *Ultramicroscopy* **134**, 200-206 (2013).
- 14 Binning, G., Quate, C. F. & Gerber, C. Atomic Force Microscope. *Phys. Rev. Lett.* **56**, 930-934 (1986).
- 15 Khoury, M. & Ferry, D. K. Effect of molecular weight on poly(methyl methacrylate) resolution. *J. Vac. Sci. Technol. B* **14**, 75-79, doi:10.1116/1.588437 (1996).
- 16 Saka, H., Kamino, T., Ara, S. & Sasaki, K. In Situ Heating Transmission Electron Microscopy. *MRS Bulletin* **33**, 93-100 (2008).

- 17 Sairam K Malladi, Q. X., Marijn A van Huis, Frans D Tichelaar, K Joost Batenburg, Emrah Yücelen, Beata Dubiel, Aleksandra Czyrska-Filemonowicz, Henny W Zandbergen. Real-Time Atomic Scale Imaging of Nanostructural Evolution in Aluminum Alloys. *Nano Lett* **14**, 384-389 (2013).
- 18 Malladi, S. R. K. *In-situ TEM Studies: Heat-treatment and Corrosion*, TU Delft, Delft University of Technology, (2014).
- 19 Frank, J. *Electron Tomography—Three Dimensional Imaging with the Transmission Electron Microscope*. (Plenum Press, 1992).
- 20 Marc De Graef, M. A. W., Michael E. McHenry, and Yimei Zhu. In-situ Lorentz TEM Cooling Study of Magnetic Domain Configurations in Ni<sub>2</sub>MnGa. *Transactions on Magnetism* **37**, 2663-2665 (2001).
- 21 Golberg, D. & Bando, Y. in *In-situ Electron Microscopy at High Resolution* (ed F. Banhart) Ch. 6, 187-228 (World Scientific Publishing Co. Pte. Ltd., 2008).
- 22 Creemer, J. F. *et al.* Atomic-scale electron microscopy at ambient pressure. *Ultramicroscopy* **108**, 993-998 (2008).
- 23 Gai, P. L., Sharma, R. & Ross, F. M. Environmental (S)TEM Studies of Gas?Liquid?Solid Interactions under Reaction Conditions. *MRS Bulletin* **33**, 107-114 (2008).
- 24 Sairam Malladi, C. S., Qiang Xu, Tom de Kruijff, Emrah Yücelen, Frans Tichelaar, Henny Zandbergen. Localised corrosion in aluminium alloy 2024-T3 using in situ TEM. *Chemical Communications* **49**, 10859-10861 (2013).
- 25 Rudneva, M. *In situ Electrical Measurements in Transmission Electron Microscopy*, TU Delft, (2013).
- 26 Golberg, D., Mitome, M., Kurashima, K. & Bando, Y. In situ electrical measurements and manipulation of B/N-doped C nanotubes in a high-resolution transmission electron microscope. *Journal of Electron Microscopy* **52**, 111-117, doi:DOI 10.1093/jmicro/52.2.111 (2003).
- 27 Stefan Meister, D. T. S., Mark A. Topinka, Andrew M. Minor, and Yi Cui. Void Formation Induced Electrical Switching in Phase-Change Nanowires. *Nano Lett* **8**, 4562-4567 (2008).
- 28 Kiener, D. & Minor, A. M. Source truncation and exhaustion: insights from quantitative in situ TEM tensile testing. *Nano Lett* **11**, 3816-3820 (2011).
- 29 Wang, B., Tomar, V. & Haque, A. In-situ TEM mechanical testing of nanocrystalline zirconium thin films. *Materials Letters* **152**, 105-108 (2015).

- 30 Legros, M. In situ mechanical TEM: Seeing and measuring under stress with electrons. *Comptes Rendus Physique* **15**, 224-240 (2014).
- 31 Zhang, X. F. in *In-situ Materials Characterization: Across Spatial and Temporal Scales* (eds A. Ziegler, H. Graafsma, X.F Zhang, & J.W.M. Frenken) Ch. 3, 59-102 (Springer, 2014).
- 32 Butler, E. P. & Hale, K. F. in *Practical Methods in Electron Microscopy* Vol. 9 (Elsevier, 1981).
- 33 Martin, C. A., Smit, R. H. M., van Egmond, R., van der Zant, H. S. J. & van Ruitenbeek, J. M. A versatile low-temperature setup for the electrical characterization of single-molecule junctions. *Rev Sci Instrum* **82**, 053907, doi:Doi 10.1063/1.3593100 (2011).
- 34 ADwin. <<http://www.adwin.de>>
- 35 van Huis, M. A. *et al.* Atomic Imaging of Phase Transitions and Morphology Transformations in Nanocrystals. *Advanced Materials* **21**, 4992, doi:DOI 10.1002/adma.200902561 (2009).
- 36 DensSolutions. <<http://denssolutions.com/products/heating/>>



---

# Chapter 3

---

## The Use of STEM Imaging to Analyze Thickness Variations

Scanning transmission electron microscopy imaging is applied to analyze the electromigration-induced thickness variations of thin polycrystalline films. It is shown that a high angle annular dark field (HAADF) detector is required to minimize the effect of diffraction contrast. A further reduction of the diffraction contrast can be obtained using a tilt series. By comparison of corresponding STEM and AFM images a direct correlation between the intensity of the STEM signal obtained with the HAADF detector and the real thickness value was found. STEM in combination with a tilt series can determine the material distribution in polycrystalline metallic films and can accurately measure shape of nanogaps formed by electromigration.

This chapter is based on: Rudneva, M.; Kozlova, T.; Zandbergen, H.W. *The use of STEM imaging to analyse thickness variations due to electromigration-induced mass transport in thin polycrystalline nanobridges*. *Ultramicroscopy* **2013**, 134, 155-159

### 3.1. Introduction

Characterization and understanding of failure mechanisms and electrical transport properties are crucial for the further development of micro- and nanoelectronics. Ten-nanometer-scale metallic wires are increasingly being used for such studies and applications. Passing an electric current through such wires can destroy them due to electromigration<sup>1</sup>. Elsewhere we reported the possibility to follow the electromigration process in Pt<sup>2</sup> and in Pt–Pd nanobridges<sup>3</sup> using *in situ* transmission electron microscopy (TEM) in bright field TEM (BF-TEM) and scanning TEM (STEM) modes.

For accurate measurements of material transport due to electromigration, the contrast in TEM images should be interpreted correctly. As was previously discussed in Chapter 2 section 2.1.1, in BF-TEM images of polycrystalline thin films, two competing types of contrast exist: mass-thickness contrast and diffraction contrast, which arises from the difference in grains orientation. This complicates the determination of the real thickness of such samples. Applying *in situ* STEM imaging of the electromigration process facilitates the study of mass transfer in polycrystalline films, but diffraction contrast can still influence the thickness analysis.

In this Chapter the STEM method to analyze the thickness distribution in polycrystalline Pt–Pd nanobridges is shown. Also, the ways of minimization of diffraction contrast contribution to the STEM signal intensity are discussed.

### 3.2. Experiment

Polycrystalline metallic Pd–Pt nanobridges with thicknesses of 15–20 nm were produced by e-beam evaporation on 100-nm-thick freestanding silicon nitride membrane. Details of the sample fabrication process can be found in Chapter 2 section 2.2. Figure 3.1(a) shows the scanning electron microscopy (SEM) image of the chip with 24 nanobridges connected to 100-nm-thick gold contacts. Figure 3.1(b) shows the magnified bridge, inset corresponds to BF-TEM image of the same nanobridge. It's clear that imaging was done after the electromigration process (the bridge is broken).

Prior to analyzing the thickness distribution in thin metal lines, we performed electromigration experiments in two modes of voltage applying: bias-ramping mode and feedback-control (FBC) mode. In the bias-ramping mode the voltage increases uniformly with the constant speed (was set to 15 mV/s) up to the maximum predefined value (or till the nanobridge break). In the FBC mode the nanobridge resistance is monitored while voltage increases, and when the measured resistance exceeds the threshold value (predefined by operator), the voltage drops<sup>4</sup>. The detailed description of *in situ* electrical measurements setup can be found in Chapter 2 section 2.3.1.

(S)TEM imaging was performed using a FEI Titan microscope operated at 300 kV and equipped with a Fischione 3000 annular dark-field detector (ADF). Samples were cooled to

approximately 100 K to minimize carbon contamination. For atomic force microscopy (AFM) imaging we used a Veeco AFM Nanoscope V in tapping mode.

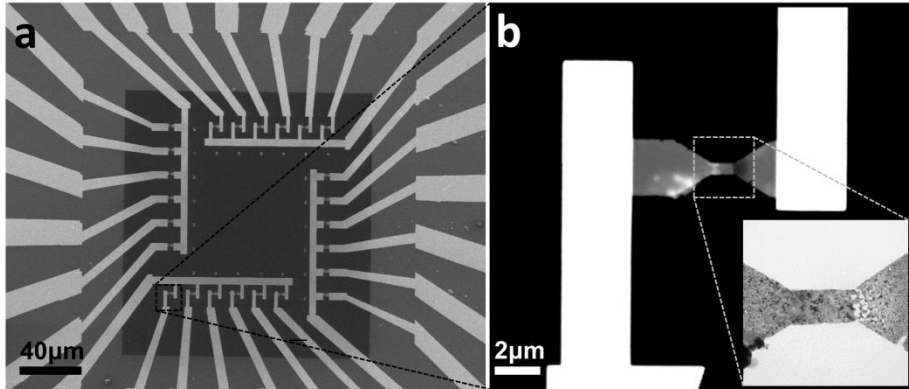


**Figure 3.1.** (a) SEM image of the central part of a  $2 \times 2$  mm<sup>2</sup> chip with gold contacts and metal bridges located in the black area in the middle (freestanding membrane); (b) magnified SEM image of fully electromigrated and thus broken bridge; inset shows BF-TEM image of the same bridge.

### 3.3. Results and discussion

#### 3.3.1. Grain growth due to the Joule heating

When an electric current is passed through the nanobridge, grain boundaries (GB) improvement and grain growth (GG) occur prior to electromigration due to Joule heating. Figure 3.2(a) shows the BF-TEM image of the bridge after the break with the non-uniform-sized grains distribution formed during the current passage through the structure. Initially, as-fabricated, bridges had a thickness of 20 nm and grain sizes were 5–10 nm. It is clear from Figure 3.2(a) that bigger grains (20–50 nm in diameter) have formed in the center of the bridge and in adjacent contacts due to the Joule heating<sup>5</sup>, whereas grains located far from the bridge center remain unchanged.

This effect of GB improvement and GG can be also seen in the I–V plot as an upward change in the I–V slope (see Figure 3.2(b)). The drop of differential resistance can be explained by diminishing of electron–GB scattering due to the smaller number of grain boundaries after the grain growth. More details on the grain growth process will be discussed in Chapter 5.

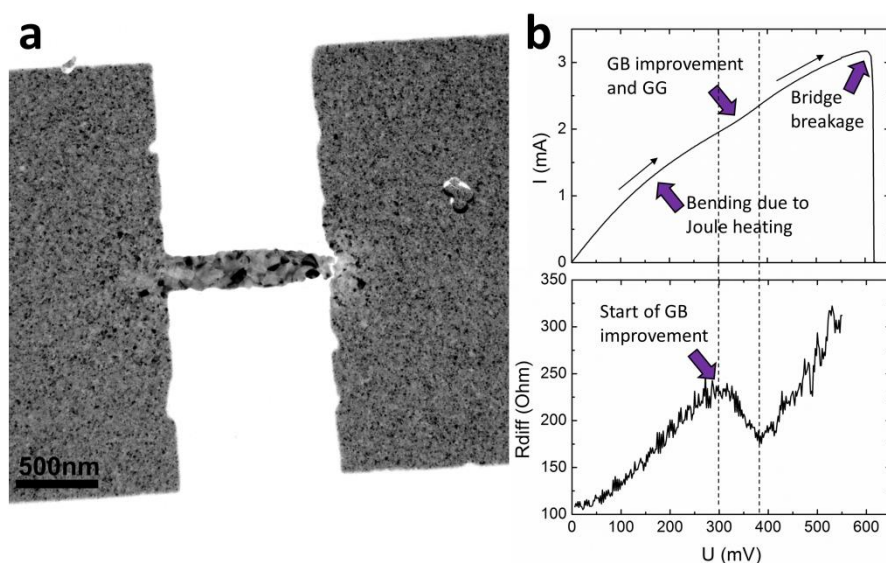


**Figure 3.2.** (a) Bright-field TEM image of the nanobridge after grain growth. (b) Characteristic I–V profile and corresponding differential resistance of the typical *in situ* electromigration experiment. The initial increase in the differential resistance due to Joule heating is followed by a decrease induced by grain growth in the sample. Ongoing increase of the voltage leads to electromigration and subsequent bridge breakage.

### 3.3.2. The ways of mass-thickness contrast enhancement: camera length decrease and averaging through tilt series

It was shown by Kozlova et al.<sup>3</sup> that electromigration in Pt–Pd nanobridges displaces material from the cathode side toward the anode side of the bridge. Consequently, this results in an inhomogeneity of the bridge thickness after the electromigration process has ended. The analysis of mass transfer is hampered—as mentioned in the introduction—by diffraction contrast. Figure 3.2(a) shows a BF TEM image of a nanobridge after grain growth but before electromigration with still almost equal film thickness. The significant difference in contrast in this image is only due to diffraction contrast and thus it is clear that a BF image cannot be used to determine thickness. In order to minimize the effect of diffraction contrast, we obtained ADF STEM images of the bridge after breakage with several values of camera lengths between 363 and 29 mm. Images obtained at two outermost camera lengths are presented in Figure 3.3(a) (for 29 mm) and Figure 3.3(b) (for 363 mm) at  $\alpha = 0^\circ$  tilt angle. It is evident that, in the STEM image obtained at a camera length of 363 mm, the gray levels not only correspond to the thickness variation in the sample but also the grains orientations (low zone axis-oriented grains appear brighter). The STEM image acquired with a shorter camera length (Figure 3.3(a)) demonstrates much more uniform contrast on the sides of the sample (contact pads) where thickness is equal, although a small number of grains is still

recognizable. Nevertheless the thickness variation in the sample can be determined from the variation in the STEM signal intensity (the brighter the area, the thicker it is).

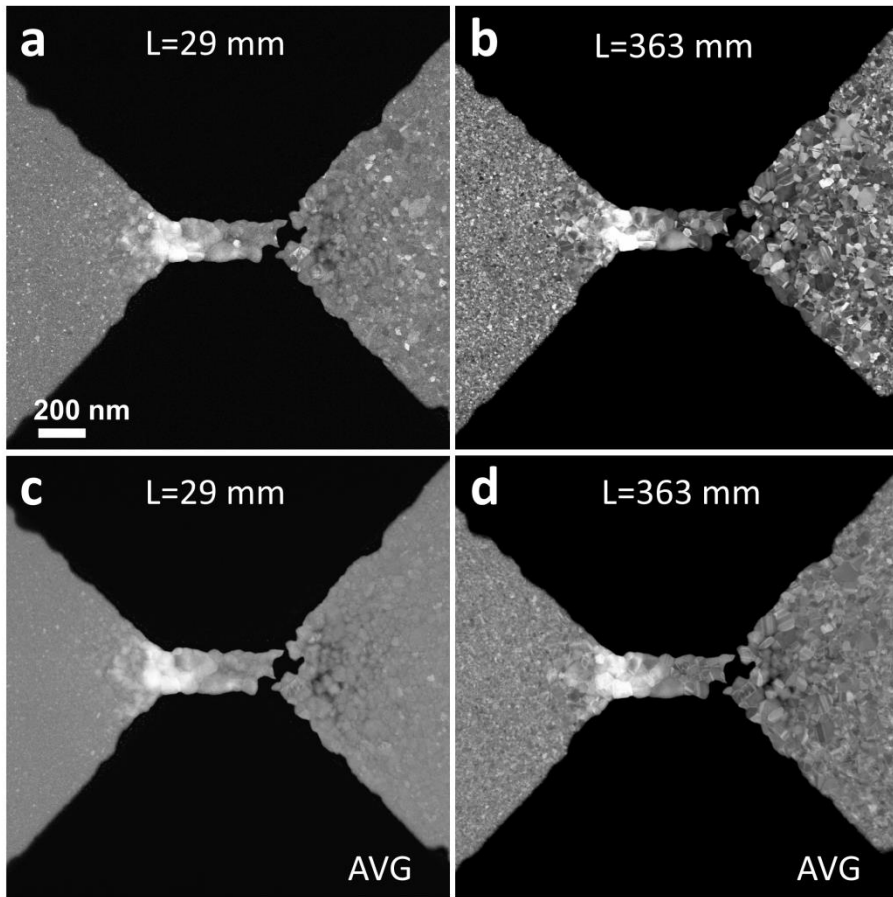


**Figure 3.3.** (a) and (b) ADF STEM images of the bridge after breakage obtained for camera lengths of 29 and 363 mm, respectively. Tilt angle is 0°. (c) and (d) Averaged STEM images over the tilt series from  $-5^\circ$  to  $5^\circ$  with a step of  $1^\circ$  for the same camera lengths.

The STEM images obtained for the smallest possible camera length of 29 mm still show some diffraction contrast, resulting in a number of visible grains. To further minimize the effect of the diffraction contrast in STEM, we recorded a tilt series for the same camera lengths with an  $\alpha$  tilt from  $-5^\circ$  to  $5^\circ$  with steps of  $1^\circ$ . We aligned and averaged the obtained series of images using ImageJ<sup>6,7</sup>. The results of this averaging are presented in Figure 3.3(c) and (d). For the short camera length (29 mm) the contrast in a contact pads area become almost uniform and individual grains are difficult to distinguish. For a camera length of

$L=363$  mm, the quality of a tilt-averaged image is similar to that of the single image obtained at  $L=29$  mm. It is evident that a tilt series is very useful for reducing the effect of diffraction contrast.

Whereas the use of the small camera length for thickness determination has a clear advantage of much less diffraction contrast, the STEM setting leads to much less counts on the HAADF detector and a longer exposure time is required to record each frame. For example for the *in situ* TEM recording of electromigration process in nanobridges we used a frame rate of about 10–15 fps, whereas for quantitative analysis of the STEM images, we used a rate of 3 fps or less, thus slowing down the image frequency of the *in situ* study of the thickness variation.

The difference in the diffraction contrast for STEM images obtained at different camera lengths can in part be explained by considering the part of the diffraction pattern that is imaged on the HAADF detector. Figure 3.4 presents an intensity line profile collected over a typical diffraction pattern for a polycrystalline Pt bridge (shown in the inset). The position of the inner radius of the ADF detector is superimposed over the line profile and indicated by red lines for camera lengths  $L=363$  mm and  $L=160$  mm. Note that, although there are no diffraction lines beyond  $40 \text{ nm}^{-1}$ , diffraction contrast is still evident in the STEM images. This is due to the higher probability for incoherent elastic scattering to large angles for the grains in a low-index orientation. Thus diffraction contrast cannot be prevented completely.

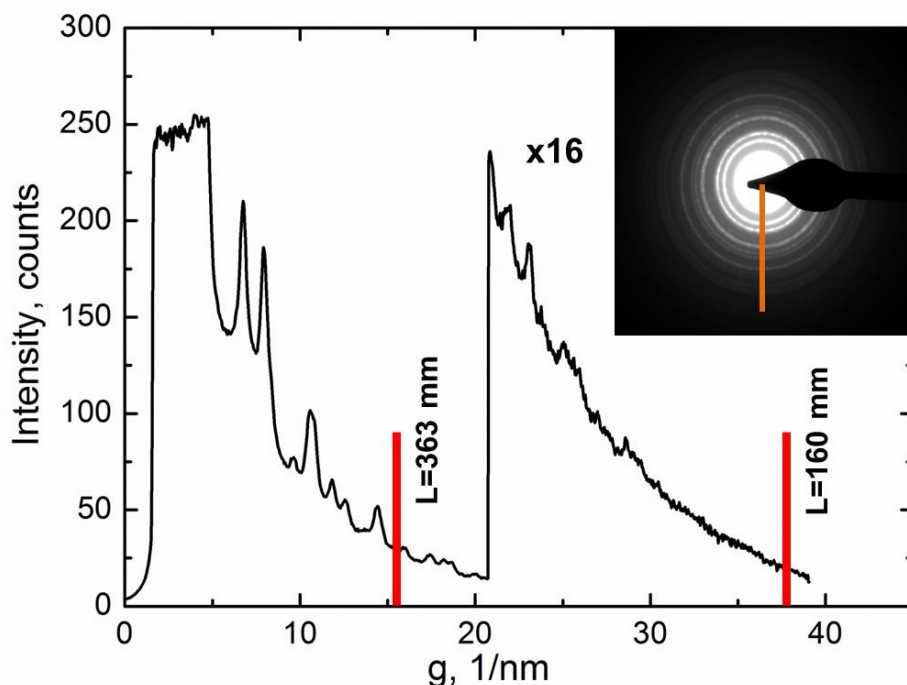


**Figure 3.4.** (a) Line profile of intensity collected over the diffraction pattern shown in the inset along orange line. vertical red lines. Positions of the inner angle of the HAADF detector of 16 and 38 mrad

correspond to a camera length of 363 and 160 mm, respectively<sup>8</sup>. The one obtained with a camera length of 29 mm (200 mrad) used in our STEM images above is not shown because it falls outside of this graph range.

### 3.3.3. STEM and AFM imaging correlation

In order to directly correlate the intensity of the STEM image and the local thickness of the metal film, we used an atomic force microscopy (AFM) to image a nanobridge morphology after electromigration (Figure 3.5(a)). The corresponding STEM image and 3D reconstruction of the bridge from it are presented in Figure 3.5(c–d). As can be seen, the brightest area in the STEM image corresponds well to the area with the biggest thickness, whereas the area with voids corresponds to the region with the lowest intensity in the STEM image. Line-thickness profiles obtained from an AFM image (Figure 3.5(b)) and from the 3D reconstruction of the STEM image (Figure 3.5(e)) demonstrate a direct correlation between the sample thickness measured with an AFM tip and the intensity of the signal obtained with an HAADF detector.

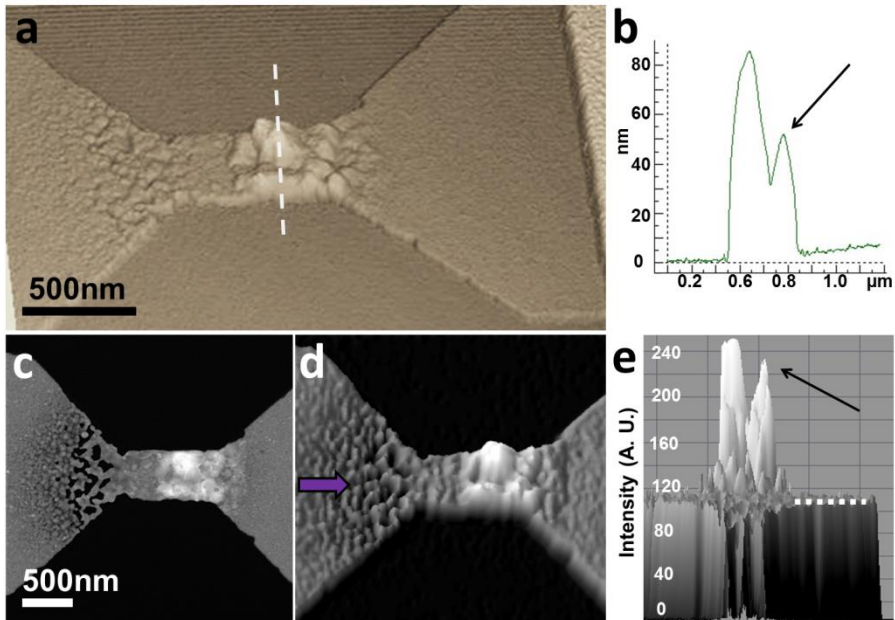


**Figure 3.5.** (a) 3D AFM image of the bridge showing the profile of material distribution after the electromigration process in the Pt–Pd nanobridge. (b) Thickness profile measured along the dashed line in (a). (c) STEM image of the bridge; (d) 3D reconstruction of (c); (e) Side view of (d) from the direction indicated by the purple arrow, it represents the thickness distribution; the dotted line corresponds to the original thickness of the sample, which is 20 nm.

### 3.3.4. STEM imaging of nanogaps

The direct correlation between the signal intensity in STEM imaging and the thickness of the sample can be used, for instance, to determine the material transfer due to electromigration and for the detailed analysis of the shape of the formed nanogaps<sup>9</sup>. The analysis of the STEM image of a nanogap created in FBC mode is shown in Figure 3.6. Figure 3.6(b) shows the thickness profile across the nanogap, whereas a 3D representation is shown in Figure 3.6(c). The intensity and brightness settings<sup>10</sup> were calibrated to reveal the actual gap size therefore a background level marked with red dashed line is visible in the height profile (Figure 3.6(b)). It was demonstrated previously<sup>11</sup> that the use of FBC mode instead of bias-ramping mode is more advantageous because it provides two symmetrical pointy contacts, which can be used, for example, for electrical transport measurements through single molecules<sup>12</sup>. In this type of study detailed knowledge of the exact shape of the nanogap is very useful. For instance, information about nanoelectrode separation as well as the 3D profile of the gap allows the typical tunnel contact area of the junctions to be estimated. For the nanogap presented in Figure 3.6, the distance between electrodes is 2.4 nm.

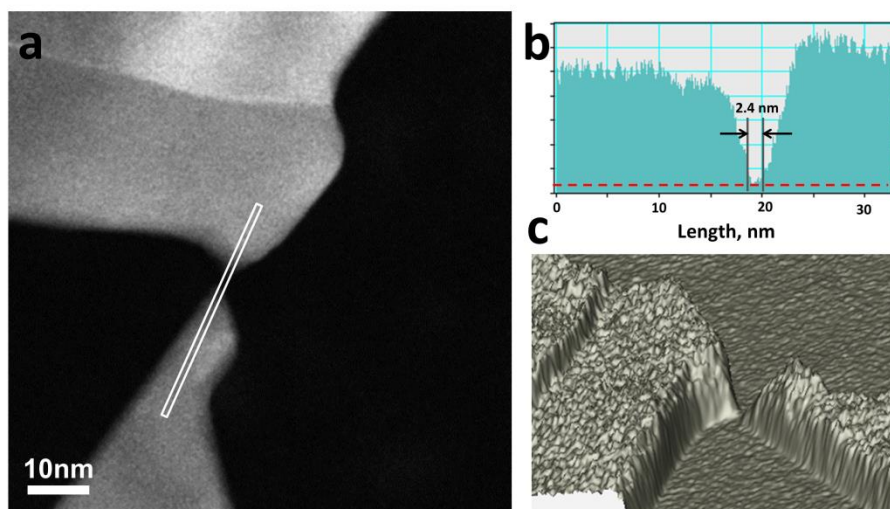


**Figure 3.6.** (a) STEM image of a nanogap obtained after the bridge breakage in FBC mode. (b) Thickness profile reconstructed along the white line in (a) with a width of 10 pixels, dashed red line marks the background level. (c) 3D reconstruction of the nanogap.

The lateral resolution of the AFM imaging of nanogaps is limited by the curvature of the scanning tip, which typically has a radius of 2 nm for ultrasharp tip<sup>13</sup>. Also the steepness of the nanoelectrodes complicates the accurate measurements of the nanogap depth. At the same time, scanning the sample with the focused electron beam in STEM mode allows more detailed information about the sample texture to be obtained at the nanoscale.

### 3.4. Conclusions

A comparison of STEM images obtained at different camera lengths reveals that a careful choice of this parameter is vital for an accurate estimation of the sample thickness. In the case of relatively high camera lengths, the various grains in a polycrystalline samples are clearly visible, which complicates the analysis of the height profiles. When a sufficiently short (typically less than 40 mm) camera length is used, the effect of the crystallographic orientation of the grains is small and this can be further minimized by averaging over a tilt series. In that case there is a good correlation between the intensity variation in the STEM image and the thickness distribution obtained by AFM. Given the small widths of gaps in relation to the depth of the nanoelectrodes, STEM analysis provides a much more reliable thickness profile, for which an AFM tip is not sharp enough.

### References

- 1 Ho, P. S. & Kwok, T. Electromigration in Metals. *Rep Prog Phys* **52**, 301-348, doi:Doi 10.1088/0034-4885/52/3/002 (1989).
- 2 Gao, B. *et al.* In situ transmission electron microscopy imaging of grain growth in a platinum nanobridge induced by electric current annealing. *Nanotechnology* **22**, doi:Doi 10.1088/0957-4484/22/20/205705 (2011).
- 3 Kozlova, T., Rudneva, M. & Zandbergen, H. In situ TEM and STEM studies of reversible electromigration in thin palladium-platinum bridges. *Nanotechnology* **24**, 505708 (2013).
- 4 Strachan, D. R. *et al.* Controlled fabrication of nanogaps in ambient environment for molecular electronics. *Appl Phys Lett* **86**, doi:Doi 10.1063/1.1857095 (2005).
- 5 McGarrity, K. S., Gao, B. & Thijssen, J. M. Simulation of Joule annealing in nanoscale Pt wires. *Computational Materials Science* **50**, 3043-3049, doi:DOI 10.1016/j.commatsci.2011.05.026 (2011).
- 6 Schneider, C. A., Rasband, W. S. & Eliceiri, K. W. NIH Image to ImageJ: 25 years of image analysis. *NatureMethods* **9**, 671-675 (2012).
- 7 ImageJ. <<http://imagejdocu.tudor.lu/>>
- 8 Rudneva, M. *In situ Electrical Measurements in Transmission Electron Microscopy*, TU Delft, (2013).

- 9 Park, H., Lim, A. K. L., Alivisatos, A. P., Park, J. & McEuen, P. L. Fabrication of metallic electrodes with nanometer separation by electromigration. *Appl Phys Lett* **75**, 301-303 (1999).
- 10 LeBeau, J. M. & Stemmer, S. Experimental quantification of annular dark-field images in scanning transmission electron microscopy. *Ultramicroscopy* **108**, 1653–1658 (2008).
- 11 Rudneva, M. *et al.* In-situ transmission electron microscopy imaging of electromigration in Pt nanowires. *Microscopy and Microanalysis* **11** (2012).
- 12 Ferry Prins, F., Shaikh, A. J., van Esch, J. H., Eelkemab, R. & van der Zant, H. S. J. Platinum-nanogaps for single-molecule electronics: room-temperature stability. *Phys. Chem. Chem. Phys* **13**, 14297-14301 (2011).
- 13 Girod, S. *et al.* Real time atomic force microscopy imaging during nanogap formation by electromigration. *Nanotechnology* **23** (2012).

---

# Chapter 4

---

## Reversible Electromigration in Pd–Pt Nanobridges

We investigated the reversible electromigration in Pd–Pt nanobridges by means of *in situ* electron microscopy. Real-time nanometer-scale imaging with scanning transmission electron microscopy (STEM) was used to determine the direction of material transport. For high current densities ( $3 - 5 \times 10^7$  A/cm<sup>2</sup>), material transport occurs from the cathode towards the anode side, indicating a negative effective charge. The electromigration is dominated by atom diffusion at grain boundaries on the free surface. The reversal of material transport upon a change of the electric field direction could be the basis of a memristor.

This chapter is based on: Kozlova, T.; Rudneva, M.; Zandbergen, H.W. *In situ TEM and STEM studies of reversible electromigration in thin palladium–platinum bridges*. *Nanotechnology* **2013**, *24*, 505708

**Patent:** Kozlova, T.; Rudneva, M.; Zandbergen, H.W. *A memristor based on electromigration in metal alloy*, Netherlands NL 2010887, Issued May 29, **2013**

## 4.1. Introduction

An *in situ* TEM study of electromigration processes in thin polycrystalline bridges allows the changes caused by the electromigration process to be imaged down to the atomic scale. According to atomic approach, the introduction to which was given in Chapter 1 in section 1.1.2, while passing current through the metallic bridge, atoms will move from their crystal lattice position due to the electromigration force. Since atoms at the surface and at grain boundaries have a smaller binding energy, these atoms are most likely to be electromigrated. The electromigration force is assumed to be the sum of two terms: the electrostatic force (direct force on an atom or ion) field and the electron-wind force. The wind-force corresponds to the momentum transfer from electrons to atoms in scattering processes, such as grain-boundary scattering, surface scattering, scattering on point defects or phonon scattering<sup>1,2</sup>. Grain-boundary scattering process dominates over surface scattering when the grain size is smaller than the mean free pass (MFP) of electrons in material and smaller than the film thickness<sup>3</sup>. Because atoms move under the electric field, they can be considered to have an effective charge<sup>2</sup>.

The place of the bridge failure due to electromigration often indicated as the location of maximum atomic flux divergence (AFD)<sup>4</sup>. AFD is the result of all forces on the atoms, namely the direct force, the electron-wind force, the thermal gradient and mechanical stresses<sup>3</sup>. The thermal stress is due to Joule heating. Mechanical stress has two components: one due to different thermal expansion of the metal and supportive layer, and one arising from a change in the mass distribution due to electromigration-induced mass transport.

Electromigration in pure palladium (Pd) has not yet been investigated; to our knowledge there is only one publication to date on the current sustainability of Pd thin films<sup>5</sup>. The effect of adding a second element to the current sustainability has been investigated in particular for Al<sup>6</sup> and Cu<sup>7</sup>. In general the concentration of the second element was up to 2%. The second elements ranged from the ability to form a compound with the host element to solid solutions or insolubility. In most cases an increased electromigration resistance was obtained<sup>1</sup> and this was attributed mainly to a strong enrichment of the second phase at the grain boundaries. The effect of Pd and Pt alloying on the electromigration behavior has not yet been reported. These elements are both noble metals from the platinum group. They have quite different masses and form a solid solution over the entire composition range.

In this Chapter we report *in situ* transmission electron microscopy (TEM) and scanning TEM (STEM) results for electromigration in Pd–Pt (10 at.%) nanobridges with different geometries. We focus in particular on the direction of material migration in relation to the electric current direction and show that material transfer occurs from the cathode towards the anode side and that transport can be reversed by changing the current direction.

## 4.2. Experiment

Polycrystalline Pd–Pt nanobridges with a thickness of 15 nm were produced by e-beam evaporation from a Pd–Pt alloy source onto a 100-nm-thick freestanding silicon nitride membrane. The contacts towards the nanobridges were made with a 97-nm-thick layer of Au and a 3-nm-thick adhesion layer of Cr. All details of sample preparation are given in Chapter 2 section 2.2. A scanning electron microscopy (SEM) image of the chip is shown in Figures 4.1(a–b). The  $2 \times 2$  mm<sup>2</sup> chip has 28 Au contacts (white lines in Figure 4.1(a)), which allow connection of the Pd–Pt bridges to electrical contacts of the electromigration holder. The bridges had different lengths (500–1000 nm) and widths (200–500 nm). Figure 4.1(c) shows a schematic image of bridges with various geometries of contact pads, which are also made of Pd–Pt. The total resistance of the structures—including the resistance of bridges, contact pads and leads—before applying an electric current was between 100 and 200 Ohm.

For *in situ* electrical measurements, the wire-bonded chip fixed on Al<sub>2</sub>O<sub>3</sub> chip carrier was placed into the TEM electromigration holder, the tip of which is shown in Figure 4.1(d). The electromigration process in nanobridges was investigated by *in situ* TEM using a FEI Titan microscope operating at 300 keV. The experiments were conducted in bias-ramping mode, i.e. a uniform increase in voltage from 0 V to a maximum of 350–600 mV (this was chosen in each separate experiment), followed by a decrease back to 0 V, a subsequent increase into the negative range (–350 to –600 mV), followed by a decrease back to the original starting point of 0 V. We will henceforth call this a “loop”. If the bridge did not break after one loop, further loops were applied with an increase in the maximum voltage until the bridge broke. Throughout these cycles the rate of the voltage ramp is set to 15 mV/s, which is slow enough for us to observe the morphology changes *in situ* without making the experiments too time consuming. The bias-ramping mode is used to perform accelerated experiments. As we conduct our experiments *in situ* inside the TEM, the desired experiment duration is less than one hour. Such accelerated experiments allow a good evaluation of the critical current density and—more importantly—it enables us to visualise the electromigration process. Clearly, the temperature gradient along the bridge will be different from non-accelerated tests. Part of the holder was cooled with liquid nitrogen. Thus all experiments were performed with the chip at ~100 K to prevent beam-induced carbon contamination on the sample. Note that, due to Joule heating, the measured bridge is warmer. We recorded the footage of *in situ* electromigration experiments in TEM mode directly from the computer screen with a frame rate of 10–15 fps. TEM Imaging & Analysis (TIA) software was used to record STEM footage with a frame rate of 3 fps. To check the effect of the electron beam, experiments were also performed in the absence of an electron beam. No electron beam effect could be detected.

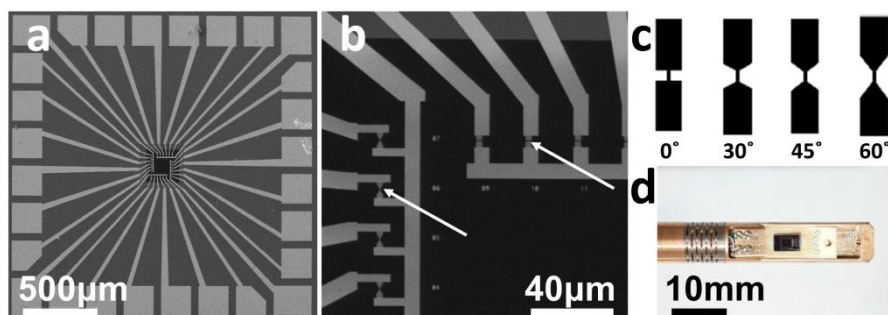


**Figure 4.1.** (a) SEM image of a  $2 \times 2 \text{ mm}^2$  chip with Au contacts and Pd–Pt bridges located in the black area in the middle (freestanding membrane). (b) Magnified view of a membrane corner, so that bridges (indicated with white arrows) and contacts are clearly visible. (c) Schematic view of Pd–Pt bridges with different geometries of the contact pads. (d) Tip of the holder used for the *in situ* electrical measurements with the chip mounted on top of an  $\text{Al}_2\text{O}_3$  carrier.

## 4.3. Results and discussion

### 4.3.1. Electromigration visualisation in TEM mode

Figure 4.2 shows snapshots of the real-time TEM footage (the entire film is available online <sup>8</sup>) recorded while passing an electric current through a Pd–Pt bridge (200 nm wide and 1000 nm long). The as-fabricated Pd–Pt bridge is polycrystalline with an average grain size of 10 nm (Figure 4.2(a)). In Figure 4.2(b) bigger grains are visible in the bridge; those grains were formed during the preceding current annealing when the applied voltage was increased to 400 mV. The rest of the TEM images in Figure 4.2 correspond to three voltage loops: the maximum voltage in the first loop (c–d) was 450 mV, in the second one (e–f) it was 470 mV, and in the third one (g–h) it was 500 mV. When the voltage was increased in the third loop to 500 mV, the bridge broke near the cathode side. The current density at the moment when electromigration starts is estimated to be  $3 \times 10^7 \text{ A/cm}^2$ . A typical  $I$ – $V$  curve of the loop is shown in Figure 4.2(i). Arrows in the images correspond to the direction of electrons from the cathode (–) to the anode (+). The electromigration results shown in Figure 4.2 are similar for all bridges, including those with other geometries (variations in lengths, widths and angles between bridges and contacts were explained above).

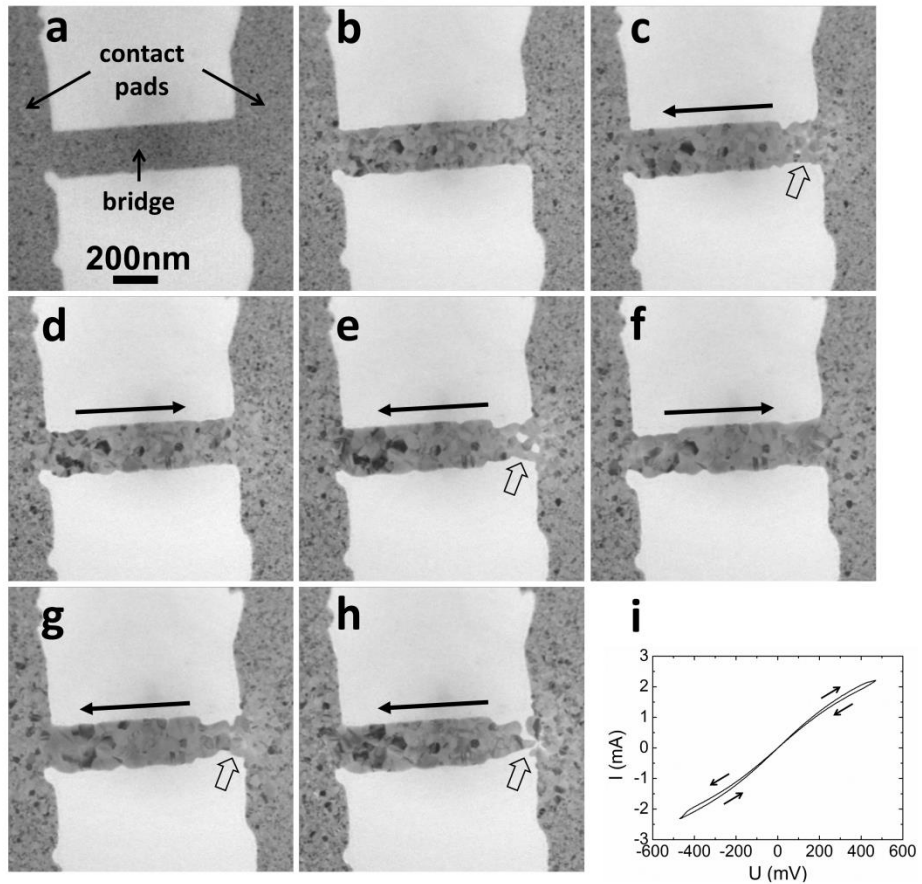


**Figure 4.2.** Snapshots from the TEM footage showing the reversible electromigration process. (a) TEM image of the initial configuration of the bridge. (b) TEM image of the Pd–Pt bridge after some preliminary grain growth. During electromigration, voids form on the cathode side (shown with wide arrow) (c, e, g, h) and are subsequently refilled (d, f) due to the changing of current direction. Black arrows indicate the direction of electrons. (i) Typical  $I$ - $V$  curve for one loop in bias ramping mode.

#### 4.3.2. Electromigration visualisation in STEM mode

Figure 4.3 shows snapshots of the STEM footage (the entire film is available online <sup>8</sup>), taken during *in situ* electrical measurements. Similar to Figure 4.2, the images in Figure 4.3 correspond to three loops of voltage increase ((a): initial view of the bridge, (b–c): first loop, (d–f): second loop, (g–h): first part of the third loop until the bridge breaks) in the bias-ramping regime. The maximum voltages were 500 mV (b–c), 520 mV (d–f) and 540 mV (g–h), respectively. The current density at the moment when electromigration starts is estimated to be  $4 \times 10^7$  A/cm<sup>2</sup>. The bridge shown has a length of 1000 nm and a width of 500 nm. The STEM images were obtained with a medium camera length (117 mm) in order to record

images of a good quality with a minimum of diffraction contrast, and thus to allow a contrast change to be attributed to a change in thickness<sup>9</sup>. The frame rate of the STEM footage was selected at 3 fps to achieve an acceptable image quality for the selected camera length.

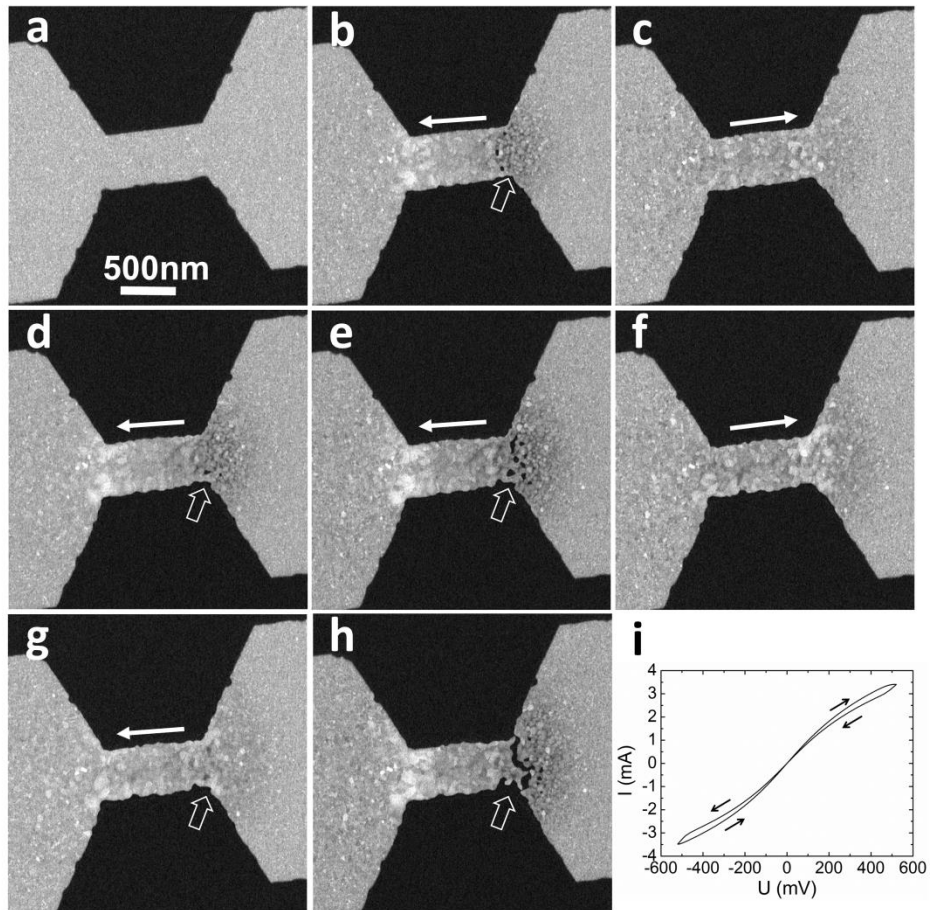


**Figure 4.3.** Snapshots from the STEM footage showing the direction of material transfer. (a) Initial view of the bridge. During electromigration, voids form on the cathode side (shown with wide arrow) and material accumulates on the anode side (b, d–e, g–h). When the current is reversed, the voids are refilled (c, f). Arrows indicate the direction of electrons. (i) Typical  $I$ – $V$  curve for one loop in the bias mode.

As can be seen in Figures 4.3(a) and (b), increasing the voltage to 500 mV causes voids to form at the cathode side (darker areas). At the same time, the sample thickens and hillocks form at the anode side (lighter areas). Changing the current direction caused the voids to refill and even hillocks to grow on the former cathode side (which is now the anode side). In summary, repeating the voltage loops leads to reverse material transport from the cathode to the anode side. We conducted experiments on bridges with different geometries, and

observed the process of reversible electromigration in every case. Both methods for electromigration visualisation – TEM and STEM – have advantages and disadvantages. TEM is used to determine the dynamics of grain growth (due to the diffraction contrast), and STEM is powerful for showing the material transfer (due to the mass-thickness contrast).

#### 4.3.3. Material transfer analysis

To analyze in detail the material transfer as a function of time, data from the STEM footage was processed using ImageJ software<sup>10</sup>. Figure 4.4(a) shows the contrast change along the bridge axis, which corresponds to changes in thickness as a function of time. It is a representation of the raw footage (the original duration of the footage was 100 s) recorded for one voltage loop with a maximum voltage of 520 mV for the sample presented in Figure 4.3. We applied a Gaussian blur with a radius of 20 pixels (115 nm) to each frame of the footage. The Gaussian blur was applied to reduce the effect of diffraction contrast; thus the contrast variation truly represents the thickness variation along the bridge. Afterwards, we extracted central lines from each frame (the dashed line shown in Figure 4.4(b)) and put them all together in one image (Figure 4.4(a)) where every horizontal line in Figure 4.4(a) corresponds to a line in the corresponding footage frame. The upper part of Figure 4.4(a) corresponds to the initial state of the bridge prior to electromigration and shows the uniformity of the bridge thickness. One of the first STEM snapshots from this area is presented in Figure 4.4(b). The middle part of Figure 4.4(a) represents the electromigrated state of the bridge with mass transferred from the cathode (right side) to the anode (left side), indicating a negative effective charge. The corresponding image is shown in Figure 4.4(c). The bottom area in Figure 4.4(a) corresponds to the situation after the current flow was reversed, where transport of the material toward the right (anode) side is observed as the voids are completely refilled and even a small hillock forms (see Figure 4.4(d)).

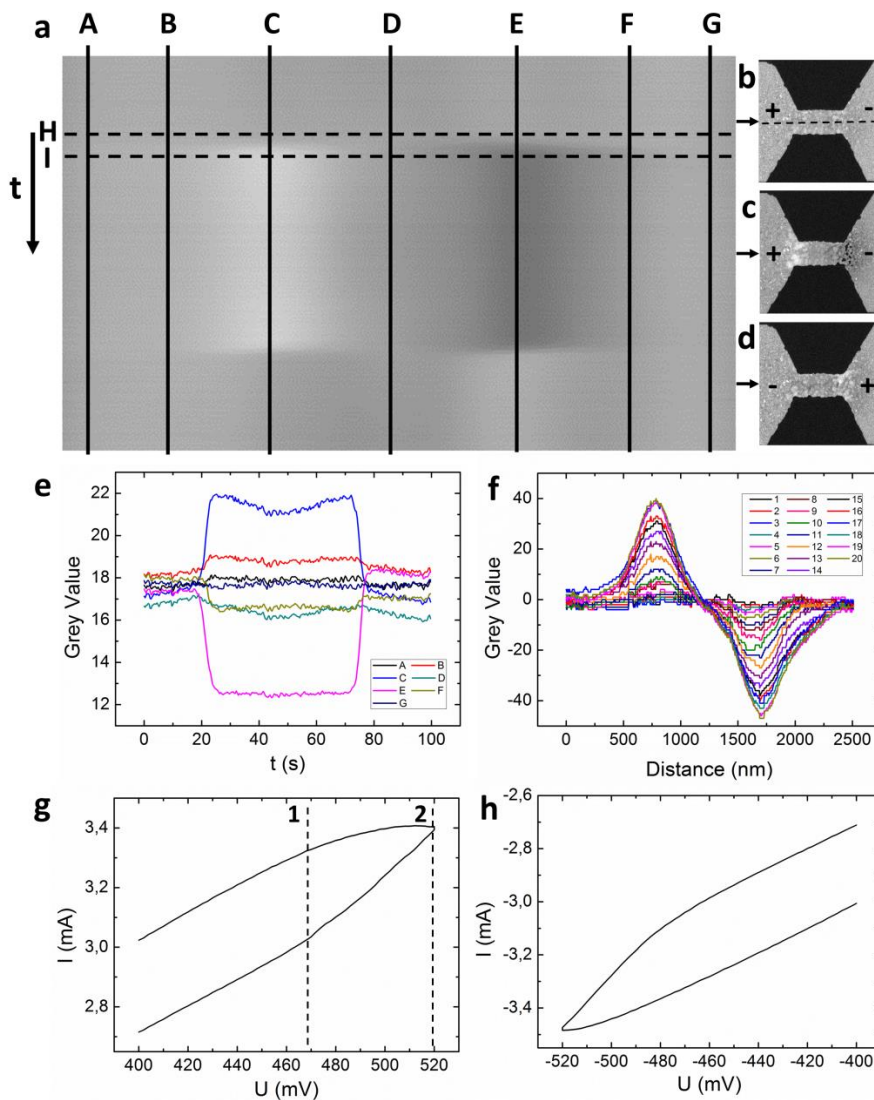


**Figure 4.4.** (a) Thickness changing along the bridge axis as a function of time; vertical lines indicate where the intensity profiles (e) were taken. (b–d) Snapshots from the STEM footage taken during electromigration at the times indicated by the arrows. (e) Gray-value change along lines A–G indicated in (a). (f) Gray-value change along the horizontal lines taken between lines H–I indicated in (a) with a step of 1 frame. (g, h) Increased areas of  $I$ – $V$  plot (in Figure 4.3(i)) near the maximum and the minimum voltages, respectively.

The vertical black lines in Figure 4.4(a) indicate where the intensity profiles shown in Figure 4e were taken. Lines C and E correspond to the ends of the Pd–Pt bridge. The distance between them is 1000 nm, which is equal to the bridge length. Lines C and E in Figure 4.4(e)

have large plateaus in the middle, and their maximum and minimum intensity levels are a result of material addition and depletion, respectively. Figure 4.4(f) shows the gray-value change along the horizontal lines taken between lines H and I in Figure 4.4(a) with a step of one pixel, corresponding to one third of a second. These data show the change in contrast compared to line H obtained by subtraction. Before the material transfer (close to line H in Figure 4.4(a)), the intensity is uniform along the entire bridge, but afterwards (close to line I in Figure 4.4(a)) light and dark areas appear, which indicate regions of material addition and depletion, respectively. The total period of material transfer takes approximately 18 frames; i.e. with a frame rate of 3 fps, the duration is approximately 6 s. In the  $I$ - $V$  curve in Figure 4.4(g) this period is indicated by lines 1 and 2, whereby line 1 corresponds to the voltage at the beginning and the end of material transfer and line 2 to the maximum voltage in the cycle. Figure 4.5 shows the graph of differential resistance vs. time during one loop; this plot can be also used to identify the start and the duration of the electromigration process.

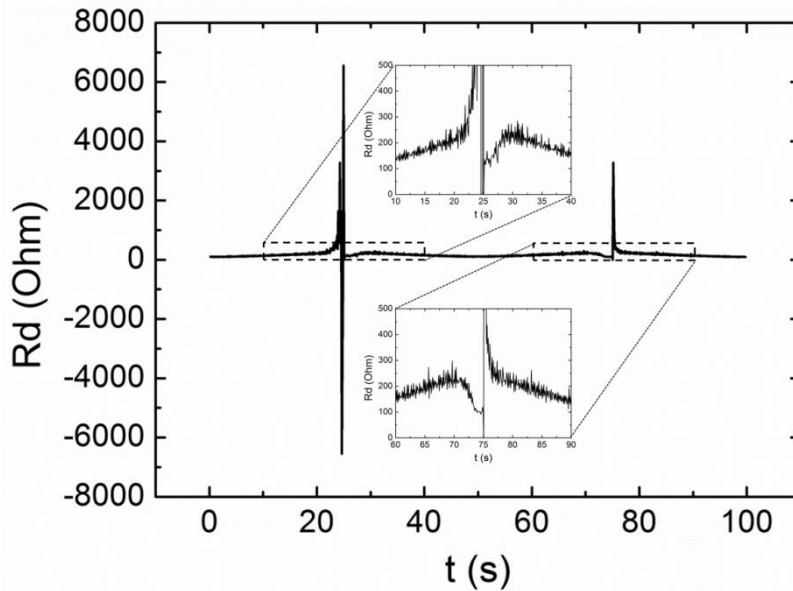


**Figure 4.5.** Differential resistance vs. time during one loop in a bias ramping mode with the maximum volatage 520 mV. Correspond to the  $I$ - $V$  curve shown in Figure 4.3(i).

The process of void and hillock formation and refilling starts quite abruptly, as evident from the sharp contrast changes in profiles C and E. These abrupt starts of the material transfer indicate the existence of a threshold value for electromigration. When this threshold value with a current density of approximately  $3 \times 10^7$  A/cm<sup>2</sup> is exceeded, electromigration starts and evolves rapidly. Yang *et al.*<sup>5</sup> report that Pd micro-stripes, which have lengths of 100–1000  $\mu$ m, widths of 2.2–3.5  $\mu$ m and thicknesses of 40–80 nm, are stable when the current density reaches 80–90% of the failure current density ( $0.8$  to  $1 \times 10^7$  A/cm<sup>2</sup>), which is in

agreement with our results for Pd–Pt bridges. Lines A and G in Figures 4.4(a) and 4.4(e) indicate places that are not affected by electromigration, because of their lower current density and lower temperature due to the contact pads acting as heat sinks. Lines B and F represent places in the contact pads where some material transport still occurs. In summary, mass transfer occurred within a Pd–Pt bridge and in close proximity to it (between lines B and F in Figure 4.4(a)). Line D, corresponding to the middle of the bridge, shows that there is almost no change in thickness in this part of the bridge. This is also visible in Figure 4.4(f), where all lines have a crossover in the middle part of the bridge. Changes in thickness do occur in the rest of the bridge, as can be seen most clearly in Figure 4.4(f). In the case of a reduction in thickness we see no grain boundary grooving in most of the bridge area (see also next paragraph).

#### 4.3.4. Grain boundaries grooving

Figure 4.6 shows STEM images (the entire film is available online <sup>8</sup>) of one of the contact pads during electromigration. It is evident that changes during electromigration occur mostly at the grain boundaries at the contact pads. Material transport starts with grooving of the grain boundaries from the surface, followed by further depletion down to the substrate and a subsequent widening. Note that some of the grain boundaries are not grooved; we suggest that these are low-energy grain boundaries, and that the fastest grooving grain boundaries have a high energy. If the current is reversed, the grooves at the grain boundaries are refilled and the initial configuration is almost obtained. In contrast with grain boundary grooving at the contact pad next to the “entrance” of the bridge, there is no grooving on the bridge itself. In this area, in addition to out-diffusion in the direction of the electron flow, there is in-diffusion from the atoms arriving from the contact pad, whereby the last flux is strong enough to prevent grooving. This is in agreement with the refilling of the grooves with reversible electromigration. Presumably the atoms that are expelled from the lattice—mainly at the grain boundaries—hop over a couple of atom sites <sup>11</sup>, are trapped at a high-energy site, and can be expelled again from this location, and so on.

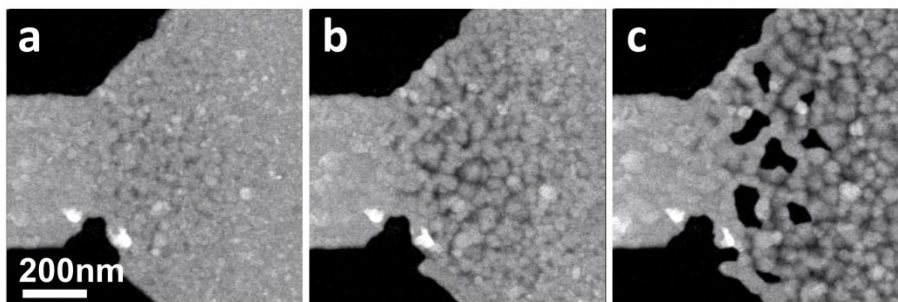


**Figure 4.6.** Snapshots from the STEM footage showing the grain boundaries grooving on the contact pad near the cathode side during electromigration.

#### 4.3.5. Bridge breakage due to the Joule heating

To investigate further the effect of Joule heating on the nanobridge morphology, we apply the alternative current (AC) of different frequencies (2–100 Hz) to several bridges. When AC is applied to the bridge, the changes in a bridge morphology are due to the symmetrical component of thermomechanical stress, which lead to material transfer from the middle part of the bridge towards the contact pads. A typical example of bridge breakage is presented in Figure 4.7. In Figure 6a one can see large grains formed due to Joule heating; then, in Figure 4.7(b), voids start to expand from the middle of the bridge, and finally the bridge breaks in the middle, as shown in Figure 4.7(c). As the bridges broke at the center in all cases where AC was applied, we conclude that the atomic flux divergence is maximum in this area. With the wire being hottest in the center the likelihood of atoms being kicked out by the electron current is highest, resulting in a thinning down in the center, with material transport in both directions of the bridge. In the case of DC measurements we observe material transport only from cathode to anode, from which we conclude that all material transport in our experiments was driven by the electromigration force (the sum of the direct and the electron-wind forces) and non-symmetrical mechanical stress.

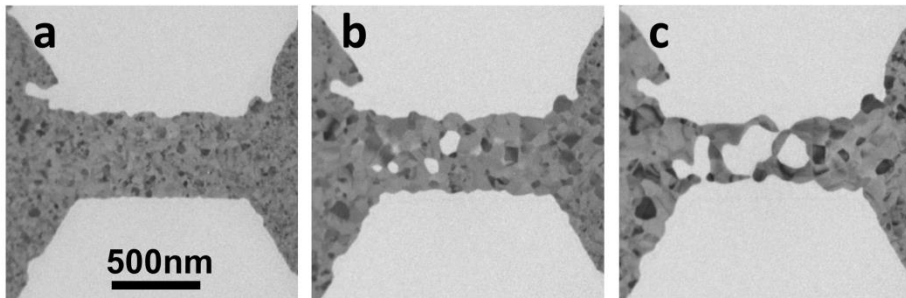


**Figure 4.7.** Snapshots from the TEM footage showing the bridge breakage process during AC passage.

#### 4.4. Conclusions

The *in situ* TEM experiments have shown clearly and consistently that electromigration with a DC current in Pd–Pt nanobridges removes material from the cathode side of the nanobridge and from the neighboring contact. The electromigrated atoms are deposited mainly at the end of the bridge and on the neighboring contact pad, where hillocks are formed. If the current is reversed, the opposite occurs: material is removed from the hillock area, and previously depleted areas are filled with material again. Material transport during electromigration can be imaged best with *in situ* STEM. The critical current density for bridge breakage is  $3 - 5 \times 10^7 \text{ A/cm}^2$ . We investigated many bridges with different geometries, and consistently observed the same effect of reversible electromigration. Continuation of this process with loops in which the maximum voltage is gradually increased ultimately breaks the bridge at the cathode side.

The behavior of the Pd–Pt alloy is quite different from the pure elements Pt and Pd. The electromigration of Pt and Pd is very similar: after a recrystallization (which resembles that of the Pd–Pt alloy) the bridge gradually becomes narrower until a nanogap is formed, whereby grain boundary grooving is not a dominant feature. Such a narrowing of the nanobridge has also been observed for Au<sup>12,13</sup>. For the Pd–Pt alloy the dominant change is grain boundary grooving, where the outer shape of the nanobridge is maintained.

A controllable resistance change is the basic principle of a memristor. For this it is essential that the outer shape of the bridge be maintained, for which the use of an alloy such as Pd–Pt has a major advantage over pure elements such as Pt, Pd and Au. With the latter elements, the width of the nanobridge decreases locally and cannot be restored in a controllable way. In the case of the Pd–Pt alloy, if we restrict the maximum voltage to a value high enough for material transfer but not enough for bridge breakage, the depletion and refilling of material can be repeated many times. We have tried 15 loops, all of which showed quite a strong material transfer observed by STEM imaging and obtained only a small difference in the bridge shape between the start and final loop. Note that these experiments are quite crude; we inspected the sample visually for any major changes, which could be done in a much more controllable manner such that the sustainability would be much higher. As the material transfer takes place between the first and second parts of the bridge, it is much better for a memristor application to compare the change in conductance of these two parts rather than the conductance over the entire bridge, which can be done by adding a metallic contact to the middle of the bridge. We filed a patent on using the metal alloy for a memristor based on electromigration<sup>14</sup>.

## References

- 1 Ho, P. S. & Kwok, T. Electromigration in Metals. *Rep Prog Phys* **52**, 301-348, doi:10.1088/0034-4885/52/3/002 (1989).
- 2 Fiks, W. B. On the mechanism of the mobility of ions in metals. *Sov. Phys. - Solid State* **1**, 14-28 (1959).
- 3 Durkan, C. *Current at nanoscale. An introduction to Nanoelectronics.*, (2007).
- 4 Tan, C. M. & Roy, A. Electromigration in ULSI interconnects. *Materials Science and Engineering R* **58**, 1-75 (2007).
- 5 Yang, Y., Xu, S. Y., Xie, S. S. & Peng, L. M. Current sustainability and electromigration of Pd, Sc and Y thin-films as potential interconnects. *Nano-Micro Lett* **2**, 184-189, doi:DOI 10.5101/nml.v2i3.p184-189 (2010).
- 6 Hu, C.-K. *et al.* Electromigration drift velocity in Al-alloy and Cu-alloy lines. *J. Electrochem. Soc.* **143**, 1001-1006 (1996).

- 7 Barmak, K., Cabral, C., Rodbell, K. P. & Harper, J. M. E. On the use of alloying elements for Cu interconnect applications. *J. Vac. Sci. Technol.* **B 24(6)**, 2485-2498, doi:10.1116/1.2357744 (2006).
- 8 Kozlova, T., Rudneva, M. & Zandbergen, H. In situ TEM and STEM studies of reversible electromigration in thin palladium-platinum bridges. *Nanotechnology* **24**, 505708 (2013).
- 9 Rudneva, M., Kozlova, T. & Zandbergen, H. The use of STEM imaging to analyze thickness variations due to electromigration-induced mass transport in thin polycrystalline nanobridges. *Ultramicroscopy* **134**, 155-159, doi:10.1016/j.ultramic.2013.05.022 (2013).
- 10 ImageJ. <<http://imagejdocu.tudor.lu/>>
- 11 Huntington, H. B. & Grone, A. R. Current-Induced Marker Motion in Gold Wires. *J Phys Chem Solids* **20**, 76-87, doi:Doi 10.1016/0022-3697(61)90138-X (1961).
- 12 Heersche, H. B., Lientschnig, G., O'Neill, K. & van der Zant, H. S. J. In situ imaging of electromigration-induced nanogap formation by transmission electron microscopy. *Appl Phys Lett* **91**, doi:Doi 10.1063/1.2767149 (2007).
- 13 Johnson, S. L., Sundararajan, A., Hunley, D. P. & Strachan, D. R. Memristive switching of single-component metallic nanowires. *Nanotechnology* **21**, 125204 (2010).
- 14 Kozlova, T., Rudneva, M. & Zandbergen, H. W. A memristor based on electromigration in metal alloy, NL 2010887. Netherlands patent (2013).



---

# Chapter 5

---

## The Origin of Increased Resistivity in Platinum Nanobridges

*In situ* transmission electron microscopy (TEM) has been applied to correlate changes in resistance with morphological transformations in polycrystalline Pt nanobridges as the substrate is heated to 500°C. In the temperature range from 150 to 260°C, grain boundary improvement occurs without grain growth, resulting in a decrease of the reflection coefficient from 10 to 6%. At 260°C the process of grain growth starts, which gradually leads to a further reduction of the electrical resistance by 37%. After grain growth, the temperature coefficient of resistance (TCR) was found to be  $1.47 \times 10^{-3} \text{ }^\circ\text{C}^{-1}$ , which is 2.5 times smaller than the TCR for bulk Pt. The total resistance was considered to be electron scattering on phonons, grain boundaries, surface and point defects. Our results show that scattering on point defects yields around 40% of the total nanobridge resistivity.

This chapter is based on: Kozlova, T.; van Ruitenbeek, J.M.; Zandbergen, H.W. *The origin of increased resistivity in platinum nanobridges studied by in situ TEM*, submitted.

## 5.1. Introduction

In micro and nano-electronics, thin metallic lines are important components. Upon applying a current, the resistivity of these lines should be stable over time in order to produce reproducible output. The resistance of thin polycrystalline material can be explained by electron scattering on phonons, lattice imperfections (impurities, interstitials or vacancies), grain boundaries or surface/interface. Several processes occur as the temperature increases: (a) the number of phonons increases (almost linearly with temperature); (b) the number of vacancies/interstitials decreases; (c) grain boundaries anneal and their number decreases due to grain growth; (d) surface roughness decreases, driven by the minimisation of the surface energy. Only the first process is reversible; the other processes lead to irreversible changes in the nanowire characteristics.

If only phonons are taken into account, the resistance  $R$  will increase with temperature  $T$  in accordance with the equation

$$R = R_0(1 + \beta(T - T_0)), \quad (5.1)$$

where  $\beta$  is the temperature coefficient of resistance (TCR),  $R_0$  is the resistance at room temperature ( $T_0$ ). In the temperature range up to 400°C the nonlinear components of  $R(T)$  are negligible and thus  $R$  increases linearly with  $T$ , directly related to the linear increase in phonon density.

The contribution of electron scattering on lattice imperfections will depend strongly on their type and number (and thus can vary strongly depending on how the samples were prepared). Scattering on grain boundaries and surface lead to increased resistance in polycrystalline material versus single crystals.

The grain boundary scattering can change when the film is heated because grain growth process lead to a lower number of grain boundaries<sup>1,2</sup>. Using the Mayadas–Shatzkes (MS) theory<sup>3</sup> the probability of elastic scattering of conduction electron from the grain boundary (reflection coefficient  $K$ ) can be determined from the equation

$$f(\alpha) = \frac{\rho_{bulk}}{\rho_{film}} = 3 \left[ \frac{1}{3} - \frac{\alpha}{2} + \alpha^2 - \alpha^3 \ln \left( 1 + \frac{1}{\alpha} \right) \right], \quad (5.2)$$

where  $\rho_{bulk}$  and  $\rho_{film}$  are the electrical resistivity of the bulk material and the polycrystalline film,  $\alpha = \frac{l_{bulk}}{d} \frac{K}{1-K}$ ,  $l_{bulk}$  is the bulk electron mean free path (MFP), and  $d$  is the average grain size.

Note that equation (5.2) neglects the surface scattering. Tellier and Tossier<sup>4</sup> derive the following analytical expression for the film TCR ( $\beta$ ):

$$\frac{\beta}{\beta_{bulk}} = 1 + \frac{g(\alpha)}{f(\alpha)}, \quad (5.3)$$

where  $\beta_{bulk}$  is the bulk TCR and  $g(\alpha) = -\frac{3}{2}\alpha + 6\alpha^2 + \frac{3\alpha^3}{1+\alpha} - 9\alpha^3 \ln\left(1 + \frac{1}{\alpha}\right)$ .

The effect of surface scattering is modelled by Lacy<sup>5</sup> for the limit that the thickness of the thin film is smaller than the bulk MFP for electrons. He proposed the following theoretical relationship between bulk and thin film electrical resistivity:

$$\rho_{film} = \frac{\rho_{bulk}}{p[1-\ln p]}, \quad (5.4)$$

where  $p = \frac{a/2}{l_{bulk}}$ ,  $0 < p \leq 1$ , where  $a$  is the film thickness.

## 5.2. Experiment

We used a microelectromechanical system (MEMS) heater as substrate for metal nanobridges, which allows to measure the bridge resistance as a function of temperature of the MEMS heater, while recording TEM images of the bridge. Polycrystalline Pt nanobridges (the average grain size of which is 5 nm) with a thickness of 15 nm were produced by e-beam evaporation onto the centre of a 600-nm-thick SiN membrane (see Figure 5.1). The centre (approx.  $150 \times 150 \mu\text{m}^2$ ) of this membrane is surrounded by a Pt heater spiral. Details of the MEMS heater preparation are reported elsewhere<sup>6</sup>. The Pt nanobridge has a length of 1000 nm, a width 500 nm and tapered contact pads (angle of  $30^\circ$ ) and was connected to Au leads. The total resistance of the structures (including the resistance of bridges, contact pads and leads) at room temperature before applying an electric current was in the range of 200 – 250 Ohm.

Morphological changes in the nanobridges at elevated temperatures were investigated by *in situ* TEM using a FEI Titan microscope operating at 300 keV. The chip carrier was positioned in a special home-built TEM holder, the tip of which is shown in Figure 5.1(c). The holder is connected to an electrical setup ("TVVI rack"<sup>7</sup>). The four contacts of the heater spiral were linked to a heating controller in order to set the temperature (heaters were calibrated with a pyrometer), and the remaining two contacts were used to apply voltage and measure the current on the sample. The resistance change as a function of the bridge temperature was investigated by taking I/V measurements in a range of  $\pm 50$  mV. This voltage is so small that it does not result in a significant temperature increase by Joule heating. The I/V measurements were taken at temperature increments of  $10^\circ\text{C}$  (from RT up to  $500^\circ\text{C}$ ).

Owing to the 600-nm-thick silicon nitride membrane under the nanobridge in our chip configuration, it is not possible to measure quantitatively the grain size evolution in the polycrystalline bridge during heating. To determine the grain growth with temperature, a 15-nm-thick Pt film was deposited on top of the heater having 20-nm-thin windows in the SiN membrane. The grain growth was monitored during the temperature rise from RT to  $500^\circ\text{C}$  with increments of  $20^\circ\text{C}$  and keeping the temperature constant during one minute.

Small cracks are present in the polycrystalline Pt nanobridges (see Figure 5.2(c)) due to the stress relaxation of the Pt film on the SiN during fabrication; these cracks can also lead to a smaller TCR. We estimate that the cracks' effect on the total bridge resistance leads to a resistance increase of up to 30%. In the remaining text our resistance values are corrected for the cracks.

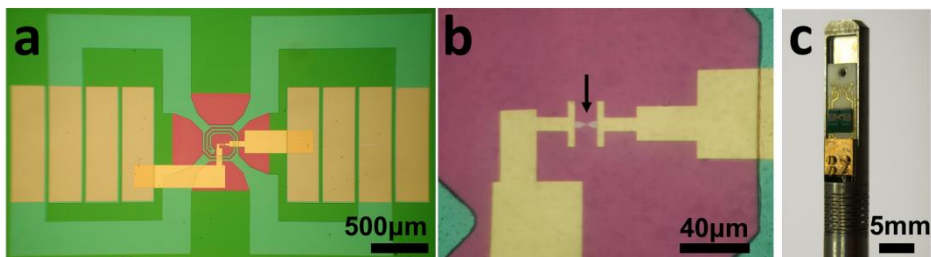


**Figure 5.1.** (a) Optical image of a ( $4 \times 3 \text{ mm}^2$ ) MEMS heating chip with additional Au contacts toward the Pt bridge located in the purple area in the middle (freestanding membrane). (b) Magnified view of the membrane centre with the bridge (indicated by the black arrow). (c) The tip of the holder used for *in situ* heating/electrical measurements with the chip mounted on top of an  $\text{Al}_2\text{O}_3$  chip carrier.

### 5.3. Results and discussion

#### 5.3.1. Electrical resistance change of Pt nanobridge during heating

Figure 5.2(a) shows the change in the electrical resistance,  $R$ , of a Pt nanobridge on a 600-nm-thick SiN support during heating from RT to  $500^\circ\text{C}$  and a subsequent decrease to RT in steps of  $10^\circ\text{C}$ . Two heating cycles were done. Figure 5.2(b) shows the temperature dependence of the resistance derivative ( $dR/dT$ ) as a function of temperature for the first heating cycle. A polynomial trend line is added for easier data visualisation. Figure 5.2(c) shows a TEM image of the nanobridge at RT; individual grains in the polycrystalline bridge are hard to distinguish due to the thick SiN support.

To determine the grain sizes in the 15-nm-thick Pt film and the grain growth as a function of temperature, films deposited on 20-nm-thick SiN were heated; this thickness is small enough to distinguish individual grains. Figures 5.2(d–h) correspond to the image series of the same film area during heating. We used annular dark-field STEM imaging with the big camera length (460 mm) because this imaging technique enhances the contrast between the grains<sup>8</sup>. All images of the series taken every  $20^\circ\text{C}$  are shown in Appendix A5.

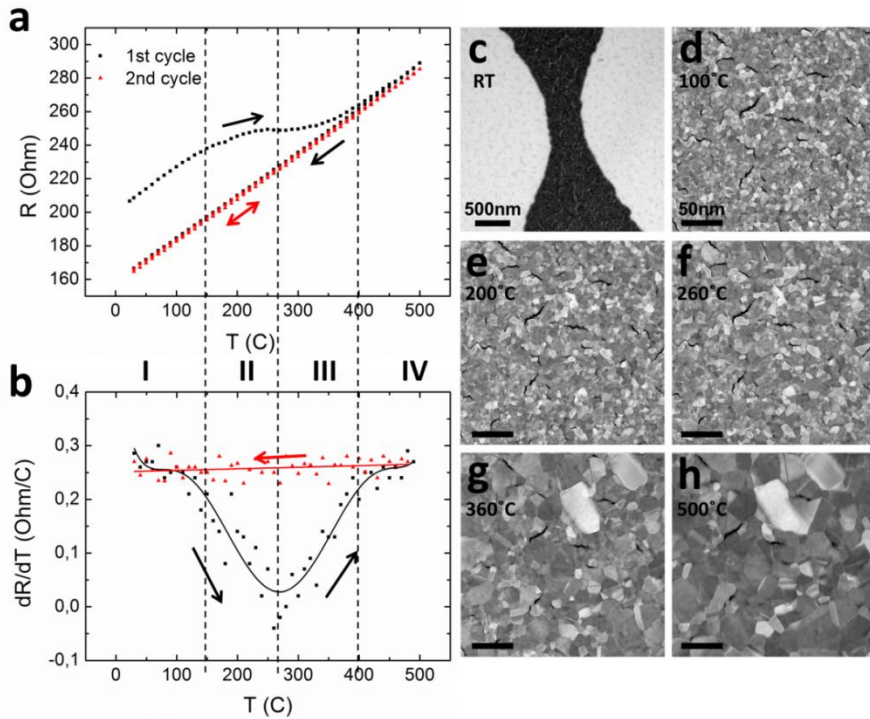


**Figure 5.2.** (a) Electrical resistance change of a Pt nanobridge during a heating cycle; first cycle shown by black arrows and symbols, second shown in red. (b)  $dR/dT$  during the first heating (black dots and arrows) and cooling (red dots and arrow) cycle; a polynomial trend line is added for data visualisation. (c) TEM image of the bridge at RT. (d–h) STEM image series of the grain growth; the temperature is indicated in each image.

To discuss the data in Figures 5.2(a–b) we divide the  $R(T)$  profile into four intervals: (I) 23–150°C; (II) 150–260°C; (III) 260–400°C; (IV) 400–500°C. In Interval I, which starts with the as-prepared bridge, the resistance increases linearly to 150°C with  $dR/dT = 0.25 \frac{\text{Ohm}}{\text{C}}$  and no grain growth occurs (Figure 5.2(d)). The grain size is approximately 5 nm. In Interval II the  $R(T)$  dependence starts to deviate from a linear behaviour:  $dR/dT$  drops gradually to almost zero near 260°C. Figure 5.2(e) shows that the average grain size at 260°C is almost the same as at 100°C. In Interval III, grain growth starts from about 260°C (Figure 5.2(f)) and the average grain size increases to  $\sim 30$  nm at 360°C (Figure 5.2(g)).  $dR/dT$  increases slowly and reaches a plateau of  $0.25 \frac{\text{Ohm}}{\text{C}}$  at 400°C. In Interval IV grain coarsening continues but becomes progressively slower, resulting in grains ranging from 20 to 100 nm at 500°C (Figure 5.2(h)).  $dR/dT$  is constant at  $0.25 \frac{\text{Ohm}}{\text{C}}$ . Data obtained for five other bridges show the same nonlinear behaviour during the first heating cycle.

In the second half of the first cycle the resistance decreases linearly with decreasing temperature (Figure 5.2(a)). The corresponding  $dR/dT$  is almost constant at  $0.25 \frac{\text{Ohm}}{^\circ\text{C}}$  (plotted in red in Figure 5.2(b)). During cooling to RT no additional grain growth occurs and resistance drops to 165 Ohm (versus 208 Ohm of the as-prepared sample). In the second heating-cooling cycle (shown in Figure 5.2(a) in red) the resistance follows the cooling line of the first cycle. Subsequent cycles do not lead to any further change.

### 5.3.2. The origin of increased resistivity in thin metallic films

The resistance of the nanobridge is determined by (a) electron-phonon interaction, (b) electron-point defect interaction (extended defects such as dislocations are not taken into account here), (c) electron-grain boundary (GB) interaction, and (d) electron-surface interaction (taking the Pt-SiN interface also as a surface).

The electron-phonon interaction is the main component at elevated temperatures. Above the Debye temperature, which is 240 K for Pt, it is approximately linear with temperature because the phonon density increases linearly with temperature. The interaction with a phonon leads to a scattering of the direction of the electrons, from  $\mathbf{k0}$  to  $\mathbf{k1}$ . Over the mean free path (MFP) the electrons are accelerated to an excess energy of approx. 0.5 meV, whereas the phonon Debye energy is around 20 meV. For a Pt single crystal the average distance between electron interactions with phonons is about 23 nm at room temperature<sup>9</sup>.

The electron-point defect interactions depend on the type of point defects (impurity, interstitial or vacancy) and their density. The number of interstitial atoms and vacancies changes with temperature, whereas electron-impurity interactions are temperature independent, except in the case of out-diffusion. If the electron is scattered elastically by a point defect ( $|\mathbf{k0}|=|\mathbf{k1}|$ ), the momentum is conserved by either a movement of the point defect or by the whole lattice. In the case that the collision is inelastic ( $|\mathbf{k0}| \neq |\mathbf{k1}|$ ) the electron loses (or gains) energy by creating (or annihilating) one or more phonons in order to maintain energy conservation. The scattering probability of the defect depends very much on the type of point defect. For instance in the case of Pt, a Fe atom will scatter much more than a Pd atom.

The effect of the electron-GB interaction will depend on the nature of the grain boundary and its effective width (the number of disordered atoms), for instance due to strain and point defects decorating the GB. For instance a (111) twin boundary in the FCC lattice shows almost no scattering<sup>10</sup>. Like in the interactions with point defects, the collision can be elastic or inelastic. The change in energy of the electron in the GB scattering process requires the interaction with a phonon to conserve momentum and energy. Alternatively, this energy can be transferred to atoms on a GB, which allows it to overcome the energy barrier and move to a lower energy position (in other words, the grain boundary improves). Note that theoretical studies<sup>11,3</sup> of electron-GB interaction assume that all grain boundaries are perpendicular to the nanobridge direction and moreover are all of the same nature. In reality

the grain boundaries have random orientations and different grain boundary structures, so they will actually show a wide distribution of the transmittance.

The electron–surface interaction can be specular or diffusive. In the case of specular scattering there is no increased path length of the electron and thus no increase in resistance. When diffuse scattering occurs, the resistance changes.

Note that phonons also interact elastically as well as inelastically with other phonons, point defects, GBs and the surface. Owing to the scattering of phonons by point defects and grain boundaries, the heat conduction will be reduced and thus the bridge will be hotter.

Our samples differ in three aspects from a bulk sample: there can be more point defects, there are many more grain boundaries, there is a surface and the Pt–SiN interface. As mentioned above, the bulk MFP of electrons in Pt at RT is 23 nm<sup>9</sup>, which is higher than the mean grain size (5 nm) and film thickness (15 nm). From Drude’s relation,  $\rho l = \text{const}$ , the effective MFP in our as-prepared Pt polycrystalline films ( $l_{eff}$ ) is estimated to be 6.7 nm ( $\rho_{bulk} = 105 \text{ n}\Omega \times \text{m}$ ,  $\rho_{film}$  was found to be  $361 \text{ n}\Omega \times \text{m}$ ), whereas sample annealing at 500°C results in an increase of the MFP at RT to only 8.4 nm ( $\rho_{film}$  was taken to be  $286 \text{ n}\Omega \times \text{m}$ ). This relatively small increase in the MFP compared to the big increase in the grain size from 5 to about 50 nm indicates that GBs are not the main component in the MFP decrease. We suggest that a grain boundary and a surface have a similar effect on the resistance because scattering at the surface is similar to scattering at a grain boundary in terms of its effect on the resistance. As the mean free path after annealing is still smaller than the film thickness we conclude that the enhanced number of point defects during film fabrication using e-beam evaporation is the main cause of the decrease in the MFP compared to that of bulk Pt.

The total bridge resistivity ( $\rho_{total}$ ) can be taken as a sum of four components: electron scattering on phonons ( $\rho_{e-ph}$ ), point defects ( $\rho_{e-pd}$ ), grain boundaries ( $\rho_{e-GB}$ ) and surface ( $\rho_{e-s}$ ):

$$\rho_{total} = \rho_{e-ph} + \rho_{e-pd} + \rho_{e-GB} + \rho_{e-s} = \frac{R_{e-ph}}{l_{e-ph}(T)} + \frac{R_{e-pd}}{l_{e-pd}} + \frac{R_{e-GB}}{l_{e-GB}(T)} + \frac{R_{e-s}}{a}, \quad (5.5)$$

where  $R$  is a coefficient that shows the resistance change during interactions and  $l$  is the effective MFP between scattering events of these four types of scattering.

### 5.3.3. Estimation of the four contributions to the total resistivity

In Figure 5.3 a schematic representation of the four components of total bridge resistivity (taken from Figure 5.2(a)) is shown as a function of temperature. Upon heating of the sample the contribution of the GBs changes. Initially, grain boundary improvements occur. It is a process of reorganisation of atoms at the GB in order to occupy positions of minimal energy; at that moment there is no visible changes in grains sizes. Then the GG process starts, which leads to further resistance reduction. With further increasing of temperature the grain

growth process slows, which can be explained by the grain boundary inhibition near the free surface and the film–substrate interface<sup>12,13</sup>. The size of electron–phonon scattering in Figure 5.3 was taken from bulk data. The effects of the point defects (in the further discussion only impurities are considered) and surfaces on the resistance are taken to be temperature independent, assuming their scattering probability and number do not depend on temperature. Using equation (5.4) we estimate the surface impact in the total resistivity to be  $47 \text{ n}\Omega \times m$ . The remaining resistivity  $130 \text{ n}\Omega \times m$  is attributed to point defects formed during nanobridge production.

The surface scattering impact on the total resistivity can also be estimated from other considerations. If we assume the same electron–surface and electron–GB interaction coefficients ( $R_{e-s} = R_{e-GB}$ ), the resistivity ratio can be calculated from equation (5.5) to be

$$\rho_{e-s} / \rho_{e-GB} = l_{e-GB}(T) / a, \tag{5.6}$$

which yields  $\rho_{e-s} = 23 \text{ n}\Omega \times m$ , and  $l_{e-GB}(T)$  was taken to be 5 nm.

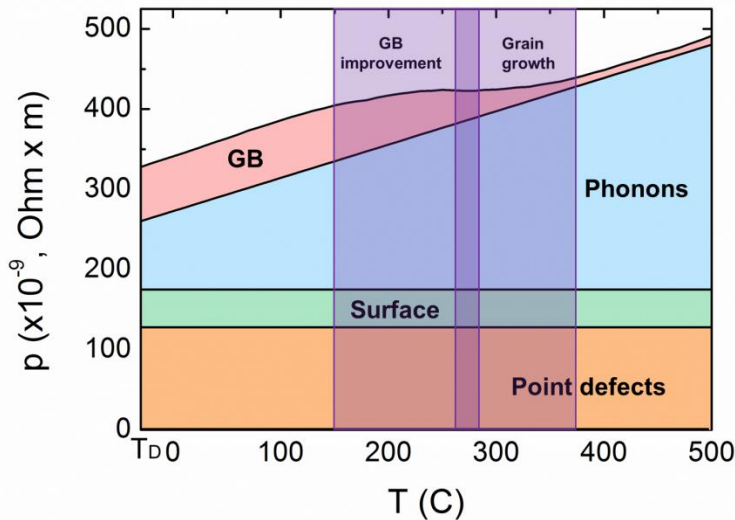


**Figure 5.3.** Representation of the four contributions to the total resistivity of a thin polycrystalline film.

In temperature Interval I the resistance increases linearly with temperature (Figure 5.2(a)) and can be fitted (equation 5.1) with  $R_0 = (208.5 \pm 0.4) \Omega$ ,  $\beta = (1.06 \pm 0.02) \times 10^{-3} \text{ }^\circ\text{C}^{-1}$  using  $T_0 = 30^\circ\text{C}$ .  $\beta$  for the bulk Pt is  $\beta_{bulk} = 3.92 \times 10^{-3} \text{ }^\circ\text{C}^{-1}$ <sup>14</sup>, thus almost 3.5 times higher. The smaller conductivity for a thin film compared to that of bulk material is generally explained by additional grain boundary and surface scattering of the conduction electrons<sup>3,15</sup>. Our  $\beta$  value is consistent with the literature<sup>16,17</sup>.

Using equations (5.2) and (5.3), and including only the contributions of the phonons and grain boundaries (see Figure 5.3) because the MS model does not include the effects of the surface and point defects, we calculate the reflection coefficient  $K$  and TCR as a function of the resistivity ratio  $\rho_{bulk}/\rho_{film}$  in Figure 5.4. Using  $\rho_{bulk}/\rho_{film(e-ph,e-GB)} = 0.6$ , the reflection coefficient is  $K = 0.1$ , which means that 10% of the electrons are scattered back on the grain boundaries. In this approach the TCR is estimated to be  $2.4 \times 10^{-3} \text{ }^\circ\text{C}^{-1}$ , which is much higher than the experimental data fitting performed with equation (5.1) ( $\beta = 1.06 \times 10^{-3} \text{ }^\circ\text{C}^{-1}$ ). This difference is easily explained: in the case of the smaller TCR the total resistance includes electron scattering on point defects and the surface, whereas in the MS model these factors are excluded.

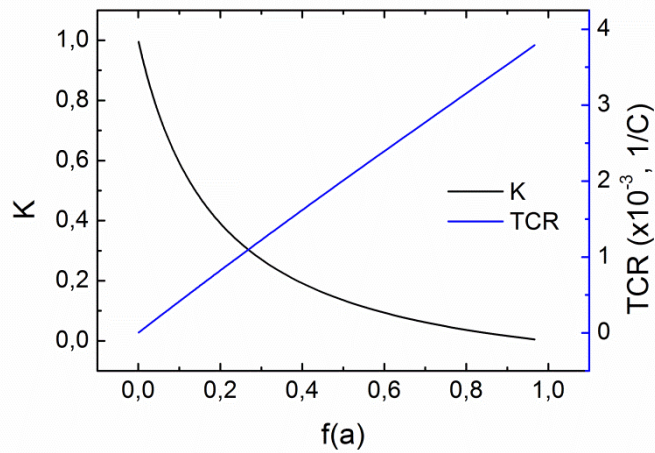


**Figure 5.4.** Reflection coefficient ( $K$ ) and TCR dependence on the resistivity ratio  $f(\alpha) = \rho_{bulk}/\rho_{film}$ , plotted based on MS theory, equations (5.2) and (5.3).

In Interval II the grain size remains the same (Figure 5.2(e)) while  $dR/dT$  drops gradually (Figure 5.2(b)). We explain this by a reduction of defects in and close to the grain boundaries, and thus the electron transmittance is increased, resulting in a smaller  $dR/dT$ . The reflection coefficient of "improved" grain boundaries is  $0.06$ , and the TCR is  $2.8 \times 10^{-3} \text{ }^\circ\text{C}^{-1}$  ( $\rho_{bulk}/\rho_{film(e-ph,e-GB)} = 0.7$  was taken from the experiment).

The grain growth process starts at  $260^\circ\text{C}$  (Figure 5.2(f)). Obviously there is sufficient energy for atoms or groups of atoms to change their position from one lattice to the lattice of the adjacent grain. As different types of grain boundaries exist in a polycrystalline film, the overall grain growth process develops gradually. Owing to the grain growth the bridge resistance decreases gradually, which is not immediately clear from Figure 5.2(a) because we apply a heating ramp, which leads to a simultaneous resistance increase owing to enhanced phonon scattering. At  $\sim 260^\circ\text{C}$  these two processes compensate each other, resulting in  $dR/dT = 0$ .

In Interval IV further grain growth occurs, but  $R(T)$  shows a linear  $T$  dependence (see Figure 5.2(a)). At 500°C the average grains size reaches 50 nm. No grain growth was observed during cooling to RT. Using Drude's relation, the MFP increases from 4.9 to 8.4 nm between 500°C and RT, respectively.

After the first cycle (fit gives  $R_0 = (164.4 \pm 0.2)\Omega$ ,  $\beta = (1.475 \pm 0.004) \times 10^{-3} \text{ }^\circ\text{C}^{-1}$ ) the TCR for the bridge in the second heating cycle is approximately 1.4 times bigger than TCR for the as-prepared bridge at the beginning of the first cycle, which is due to grain boundary improvement and grain growth<sup>18</sup>. Note that the derivative of the resistance with temperature ( $dR/dT$ ), is nearly the same as at the start of the first cycle because the larger TCR  $\beta$  is compensated by the smaller resistance  $R_0$ .

#### 5.3.4. Experiment limitation

In our experiments we were restricted in terms of achievable temperature to 500°C, because the gold of the leads starts to migrate into the bridge area at around 550°C, which causes irreproducible results and occasional bridge destruction. Figure 5.5 shows TEM images of a Pt bridge during substrate temperature increase. After temperature raise till 600°C the gold conglomerations are clearly visible as a black dots (marked with arrows in Figure 5.5(b)), and while temperature maintained at 600°C during 2 minutes new conglomerations are formed (Figure 5.5(c)).

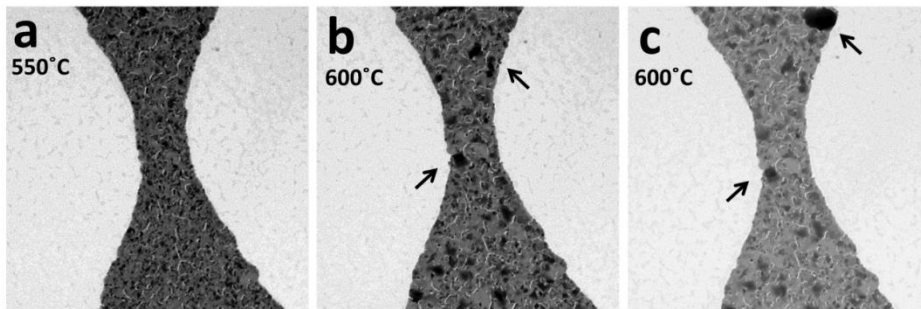


**Figure 5.5.** TEM images of a Pt bridge showing gold migration from the contact pads during temperature increase. (a) View of the bridge at 550°C. (b) Gold conglomerations (dots with black contrast indicated with arrows) are formed after temperature raise till 600°C. (c) View of the bridge after keeping it at 600°C during 2 minutes – new conglomerations are formed and grown.

In heating experiments reported above we applied an external heat source to heat the Pt nanobridge. But we can also achieve a local heating of the nanobridge by passing a relatively high current through the bridge, resulting in Joule heating. An obvious advantage of local Joule heating is that the Au leads remain at room temperature and thus there is no Au

diffusion to the nanobridge, which was the main limitation of the external heating experiments. A disadvantage is that there is a thermal gradient in the nanobridge, allowing no straightforward comparison of the Joule heating and overall heating. The next chapter will be devoted to electromigration investigation under both heating conditions – Joule heating and external heating.

## 5.4. Conclusions

Our experiments directly correlate sample heating with the number of grains in the nanobridge, allowing us to determine the electron–GB scattering contribution to resistance. It is evident that there are two effects: grain boundary improvements and the reduction of the number of grain boundaries, and we can estimate both of them. Our results indicate that the effect of the grain boundaries on the resistance increase is overestimated in the literature and the effect of the point defects is underestimated. Furthermore, theoretical models often do not include the change of grain boundaries reflectance during heating, different reflectances for the grain boundaries and increased number of point defects in thin films over the bulk material.

## References

- 1 Thompson, C. V. Structure evolution during processing of polycrystalline films. *Annual Review of Materials Science* **30**, 159-190, doi:DOI 10.1146/annurev.matsci.30.1.159 (2000).
- 2 Holm, E. A. & Foiles, S. M. How Grain Growth Stops: A Mechanism for Grain-Growth Stagnation in Pure Materials. *Science* **328**, 1138-1141, doi:DOI 10.1126/science.1187833 (2010).
- 3 Mayadas, A. F., Shatzkes, M. & Janak, J. F. Electrical resistivity model for polycrystalline films: the case of specular reflection at external surfaces. *Appl Phys Lett* **14**, 345, doi:10.1063/1.1652680 (1969).
- 4 Tellier, C. R. & Tosser, A. J. An extension of the Cottey conduction model. *Thin Solid Films* **52**, 53-61 (1978).
- 5 Lacy, F. Developing a theoretical relationship between electrical resistivity, temperature, and film thickness for conductors. *Nanoscale Research Letters* **6:636** (2011).
- 6 van Huis, M. A. *et al.* Atomic Imaging of Phase Transitions and Morphology Transformations in Nanocrystals. *Advanced Materials* **21**, 4992, doi:DOI 10.1002/adma.200902561 (2009).

- 7 Martin, C. A., Smit, R. H. M., van Egmond, R., van der Zant, H. S. J. & van Ruitenbeek, J. M. A versatile low-temperature setup for the electrical characterization of single-molecule junctions. *Rev Sci Instrum* **82**, 053907, doi:Doi 10.1063/1.3593100 (2011).
- 8 Rudneva, M., Kozlova, T. & Zandbergen, H. The use of STEM imaging to analyze thickness variations due to electromigration-induced mass transport in thin polycrystalline nanobridges. *Ultramicroscopy* **134**, 155-159, doi:10.1016/j.ultramic.2013.05.022 (2013).
- 9 Zhang, Q. G. *et al.* Influence of grain boundary scattering on the electrical properties of platinum nanofilms. *Appl Phys Lett* **89**, 114102 (2006).
- 10 Barmak, K. *et al.* *Journal of Vacuum Science and Technology A* **32**, 061503 (2014).
- 11 McGarrity, K. S., Gao, B. & Thijssen, J. M. Simulation of Joule annealing in nanoscale Pt wires. *Computational Materials Science* **50**, 3043-3049, doi:DOI 10.1016/j.commatsci.2011.05.026 (2011).
- 12 Burke, J. E. & Turnbull, D. Recrystallization and Grain Growth. *Progress in Metal Physics* **3**, 220-292, doi:Doi 10.1016/0502-8205(52)90009-9 (1952).
- 13 Rost, M. J., Quist, D. A. & Frenken, J. W. M. Grains, Growth, and Grooving. *Phys. Rev. Lett* **91**, 4 (2003).
- 14 Platinum Metals Reveiw. (2010).
- 15 Fan, P., Yi, K., Shao, J.-D. & Fan, Z.-X. Electrical transport in metallic films. *J Appl Phys* **95**, 2527-2531 (2004).
- 16 Zhang, X. *et al.* Thermal and electrical properties of a suspended nanoscale thin film. *International Journal of Thermophysics* **28**, 33-43, doi:DOI 10.1007/s10765-006-0135-1 (2007).
- 17 Lacy, F. Developing a theoretical relationship between electrical resistivity, temperature, and film thickness for conductors. *Nanoscale Research Letters* **6**, 1-14, doi:Doi 10.1186/1556-276x-6-636 (2011).
- 18 Dellinger, J. H. *Temperature coefficient of copper*. Vol. 7 (Bulletin of the Bureau of Standarts, 1910).

## Appendix A5

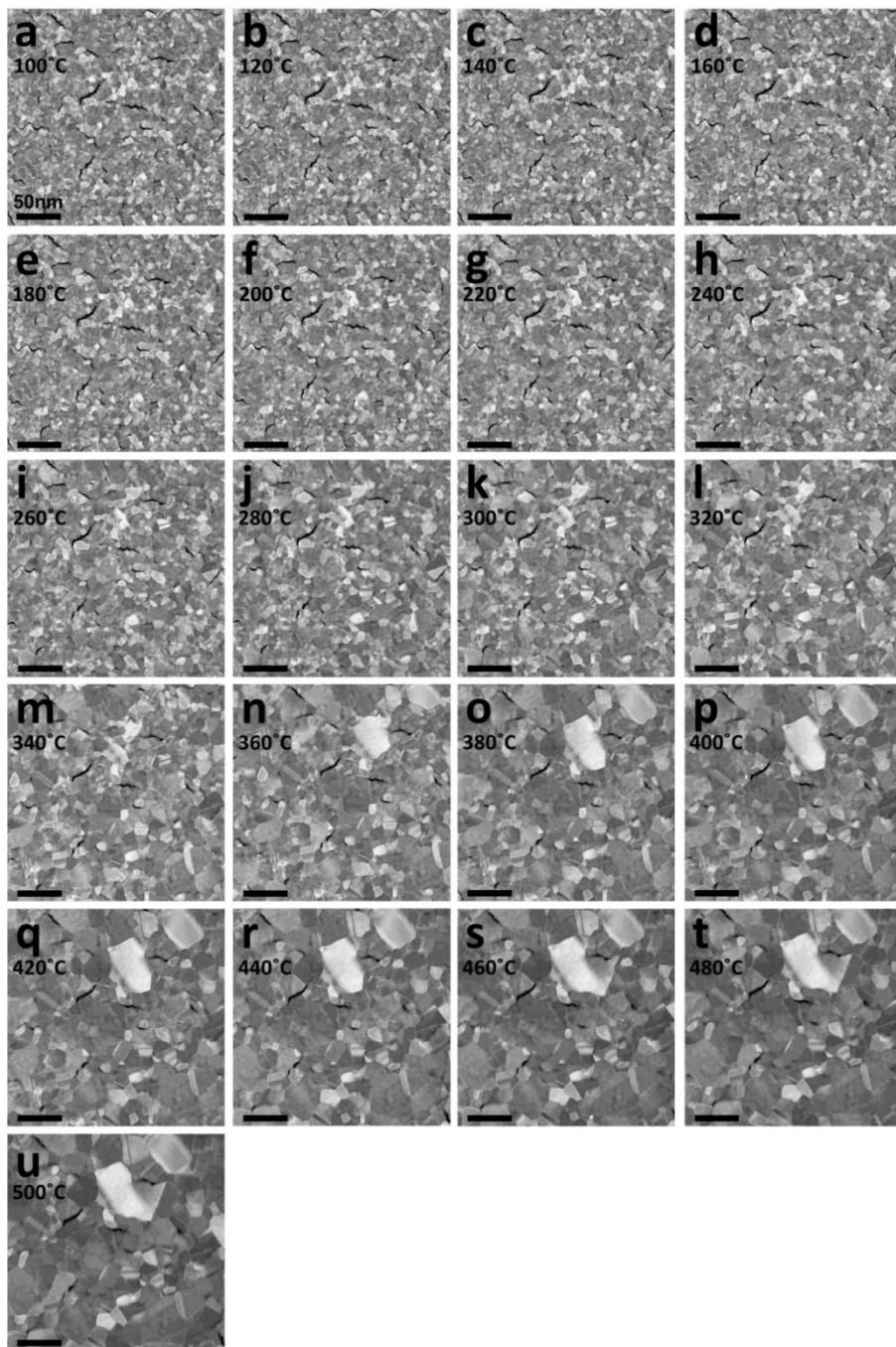


**Figure A5.** Snapshots from the STEM footage of grain growth in 15-nm-thick Pt film, temperature is indicated in each image, scale bar corresponds to 50 nm.



---

# Chapter 6

---

## Electromigration in Pt Nanobridges at Different Substrate Temperatures

We used a combination of *in situ* TEM, a MEMS-based heater as a substrate and a dedicated biasing sample holder to study the temperature dependence of electromigration in Pt nanobridges (500 nm wide, 15 nm high and 1000 nm long). Local temperature increase of the Pt bridge due to the Joule heating was determined by observing melting of Bi film deposited on the back side of SiN membrane. We visualised changes in the nanobridges under both dynamic conditions, i.e. heating (substrate temperatures up to 660 K) and current passage. Our electromigration experiments at various substrate temperatures (100, 300, 420 and 660 K) show the same tendency: Material transport occurs from the cathode to the anode side, which can be explained by the electron-wind force. In all cases the bridge breaks due to the formation of a neck closer to the cathode side. At 300, 420 and 660 K, voids and the neck form at the cathode contact pad simultaneously. The higher the temperature, the bigger the voids size. As expected, at higher temperatures a lower power is needed to break the nanobridge.

## 6.1. Introduction

When a current is passed through a metal, its temperature increases due to the Joule heating. Temperature rise in turn increases the displacement probability of atoms from their lattice position, which leads to the easier electromigration activation<sup>1</sup>. The bridge temperature (as well as displacement probability of atoms) can be changed not only by electric current passage but also by external substrate heating. For a displacement from the atomic lattice, atoms have to overcome the crystal lattice energy barrier. For the majority of metals, including Pt, the electromigration force is controlled mainly by electron-wind force, which corresponds to the momentum transfer from charge carriers (electrons) to atoms in scattering processes. As a result, material transfers in the direction of the anode<sup>2</sup>.

In the Chapter 5 we have reported on the electrical resistance change of individual Pt nanobridges during heating. Similar to many publications that show a resistivity-thickness dependence for films with thicknesses less than the bulk mean free path for electrons<sup>3,4,5</sup>, we also observed that the resistance increases ~4 times. Upon heating the nanobridge by an external heat source or by Joule heating, we first observed a drop in resistance because of the improvement of the grain boundary (GB), i.e. an increase of the GB's transmittance. The GB improvement is a process of reorganisation of atoms at and near the grain boundary towards "ideal crystal lattice" positions, which have a lower energy. This leads to a decrease in the bridge resistance due to less electron-atom interactions. Note that, apart from the scattering of electrons on non-ideal lattice positions near the GB, also the GB itself will scatter with probability which depends on the nature of the grain boundary, strain and impurity atoms decorating the GB.

A second drop occurred due to grain growth (GG)<sup>6,7</sup>. Grain growth is the process of grains size increase in a polycrystalline material at high temperatures. Due to the reduction in the number of grain boundaries internal crystal energy decreases. Grain growth is thermally activated process because atoms require access energy to overcome the energy barrier to hop to a lower energy position. Owing to the fewer number of GBs to scatter the electrons, the total bridge resistance diminishes. The GG process is stopped by inhibiting GBs near the free surface and the film-substrate interface<sup>8,9</sup>. Considering all contributions to the resistance, i.e. electron scattering on phonons, GBs, surface and point defects, we concluded that the strongest increase in resistance of thin films is due to point defects<sup>10</sup>.

*In situ* electromigration studies allow the correlation of morphological transformations of the metallic structures with the current/voltage values. Such studies become more important because of the trend to downscale metallic contact lines to nanometer sizes in devices. To our knowledge, the influence of substrate temperature on bridge morphology during electromigration has not yet been reported, only results concerning room temperature (RT) and liquid nitrogen temperature (around 100 K)<sup>2,11,12</sup>. In this Chapter we report on *in situ* TEM results of electromigration in Pt nanobridges at substrate temperatures ranging from 100 K to 660 K.

## 6.2. Experiment

The electromigration process in Pt nanobridges at elevated substrate temperatures was investigated by *in situ* TEM using a FEI Titan microscope operating at 300 keV. Figure 6.1(a) shows the schematic view of a 15-nm-thick Pt nanobridge with a length of 1000 nm, a width 500 nm and tapered contact pads (angle of 30°). Bridges with different angles of tapered contact pads were investigated (30°, 45°, 60° and 90°) at 100 K and RT substrate. We observed no noticeable influence of the angle on the electromigration process. Contacts to the nanobridges were made with a 100-nm-thick layer of Au on a 3-nm-thick adhesion layer of Cr (Figure 6.1(a–b)). Initial resistance of the structures, including bridge, contact pads and leads, is in the range of 200 – 250 Ohm. These structures were produced by e-beam metal evaporation onto a MEMS (micro-electro-mechanical-system) heater with a flat 600-nm-thick SiN centre (approx.  $150 \times 150 \mu\text{m}^2$ ), shown in Figure 6.1(c). Details of the heater preparation are reported elsewhere<sup>13</sup>.

The MEMS heater with Pt nanobridge was fixed onto an  $\text{Al}_2\text{O}_3$  chip carrier, and six contacts (four for the heater spiral and two for electrical measurements) were attached to the chip carrier by means of standard wire bonding technique. The chip carrier was placed in a special home-built TEM holder, the tip of which is shown in Figure 6.1(d). The holder is connected to an electrical setup (“IVVI rack”<sup>14</sup>). This holder allows one to combine heating experiments and electrical measurements. The contacts connected to the heater spiral – which was calibrated with a pyrometer before use – were linked to a heating controller box in order to regulate the substrate temperature. A voltage was then applied to the sample through the remaining two contacts and current was measured. More details on sample fabrication and joint electrical–heating experiments are given in sections 2.2 and 2.3.3 in Chapter 2.

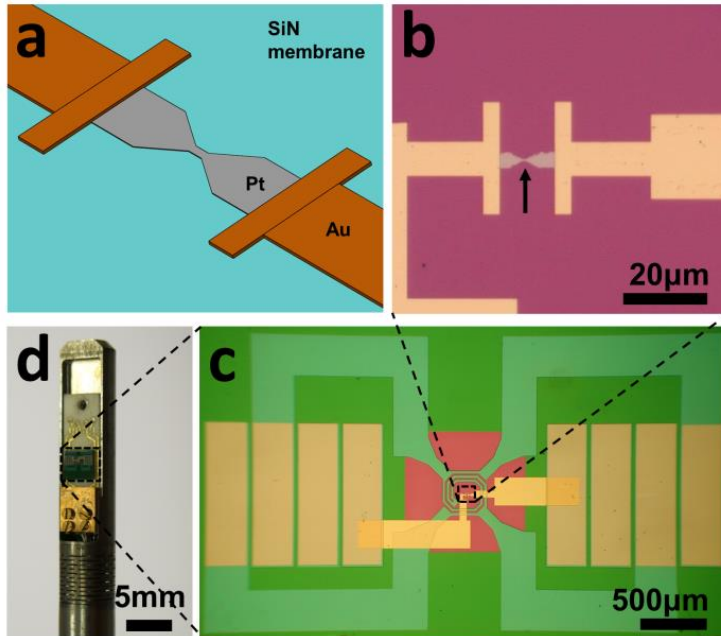


**Figure 6.1.** (a) Schematic view of a Pt nanobridge with gold contacts on a SiN membrane. (b) Optical image of the membrane centre with the Pt bridge indicated by the black arrow. (c) Optical image of a MEMS chip (4×3 mm<sup>2</sup>); four contacts for the heater spiral and two for electrical measurements of the bridge, purple area in the middle is a freestanding SiN membrane. (d) Tip of the TEM holder, built in-house, used for *in situ* heating/electromigration experiments with the MEMS chip fixed on an Al<sub>2</sub>O<sub>3</sub> chip carrier.

Electromigration was investigated at several substrate temperatures (indicated as  $T_s = 100, 300, 420$  and  $660$  K). To allow the system to equilibrate, the sample was maintained at the target value for 3 minutes after reaching the set temperatures. This time was enough to reach a stable resistance value because grains grow until their maximum size at the set conditions. The  $I$ - $V$  measurements were performed in bias-ramping mode, i.e. a gradual increase from 0 V to a predefined value of 400–800 mV, followed by a decrease back to 0 V, and continuation into the negative voltage range, after which a new cycle with higher maximum voltage was performed. The speed of the voltage ramp is 15 mV/s; hence a total loop takes 100 to 200 seconds.

The influence of carbon contamination on bridge resistance formed during beam illumination at  $T_s = 100$  K is negligible, which is confirmed by the zero conductivity value after the bridge breaks. If  $T_s = 300$  K, the small conductivity, which corresponds to the carbon contamination ring, remains after the bridge breaks. In order to minimize that “contamination conductivity”, the sample should be illuminated as little as possible. At  $T_s = 420$  and  $660$  K, the carbon contamination formation is strongly suppressed. To confirm this, we focused the

electron beam on a bridge at a temperature of 420 K. A resistance check for 15 minutes shows that the value is constant.

TEM and STEM movies were recorded during electromigration at fixed temperatures of the heater. For better data representation, the images shown in this Chapter were taken during the experiment with longer exposure times.

### 6.3. Results and discussion

In typical electromigration studies to examine ageing under application conditions, experiments take from several hours to many months. However, here we report accelerated electromigration experiments, where voltage cycles were used that take only several minutes. During such cycles the voltage and, as a result, the temperature, is constantly changing at the speed of 15 mV/s. Therefore, the system has no time to reach an equilibrium state because at least several minutes are needed to achieve a stable bridge resistance at fixed voltage. Hence, although the actual grain sizes can be directly correlated with the applied voltage in our experiment, they cannot be directly compared with conventional ageing studies. Nevertheless *in situ* accelerated experiments yielded valuable information about the electromigration.

#### 6.3.1. Electromigration at $T_s = 100$ K

Figure 6.2 shows TEM images of the bridge during bias voltage applied at  $T_s = 100$  K. The bridge with  $60^\circ$  tapered contact pads is on a 100-nm-thick SiN membrane. Grain growth is observed (Figure 6.2(b)) due to the Joule heating during the first voltage cycle. The  $I$ - $V$  curve bends in a voltage range of 300–400 mV during the first voltage increase, shown with black in Figure 6.2(e). In that segment the differential resistance of the bridge decreases, which can be clearly seen in Figure 6.2(f). During the second ramping cycle the  $I$ - $V$  curve (shown in red in Figure 6.2(e)) follows the line of voltage decrease during the first cycle. At a certain voltage (580 mV) material is removed from the sides of the bridge, which leads to a “neck formation” of the bridge, Figure 6.2(c). Finally, the bridge breaks at high current density ( $4 \times 10^7$  A/cm<sup>2</sup>), Figure 6.2(d). This result corresponds to the experiments reported previously by our group and others<sup>15,16</sup>.

We interpret that the bending of the  $I$ - $V$  curve at 300 mV during the first cycle is due to GB improvement<sup>10</sup>. As the voltage is increased further, the GG process starts. Owing to an overlap of GBs improvement and GG regimes, the voltage at which grain growth starts cannot be identified precisely, but is in a range 300–400 mV.

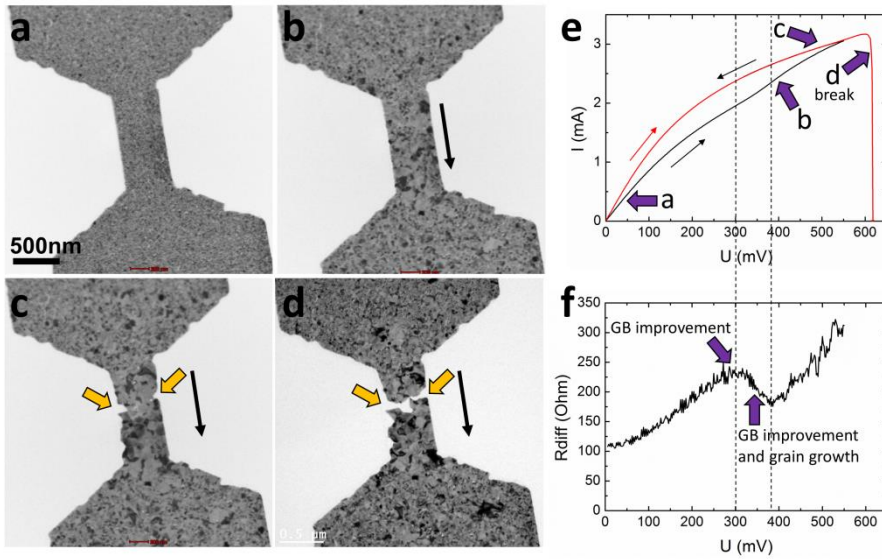


**Figure 6.2.** Snapshots from a TEM movie showing Pt nanobridge at 100 K before electromigration (a), after the GG during the first bias-ramping cycle (b). Yellow arrows indicate the presence of a neck, which is formed during the electromigration (c) and, finally, due to this neck thinning the bridge breaks (d). Black arrows indicate the direction of electrons. (e)  $I$ - $V$  curves for two voltage cycles applied to the bridge: The black line corresponds to the first cycle during which GBs improvement and GG occur; the red line shows the second cycle during which the bridge breaks. Purple arrows labelled a–d correspond to the moments at which images (a–d) were taken. (f) Differential resistance versus voltage of the 0 to +600 mV part of the first cycle clearly shows the voltage at which GB improvement starts.

### 6.3.2. Local temperature determination

In order to determine locally the raise of bridge temperature due to the Joule heating during current passage, 15-nm-thick Bi layer was deposited on the back side of SiN membrane under the Pt bridge. Melting point of bulk Bi is around 545 K, and this temperature is expected to be even lower for thin films<sup>17,18</sup>. Figure 6.3 shows the snapshots taken from a TEM movie of Pt nanobridge ( $0.2 \times 1$   $\mu\text{m}^2$ ) during current passage. First, the highest temperature is reached in the middle of the bridge which can be clearly seen from the place where Bi film starts to melt (indicated by the red arrow in Figure 6.3(b)). Then with the current increase, the temperature increases. The perimeter of the melting circle corresponds to the line with the melting temperature of Bi, while at the centre the temperature is higher. After the bridge breakage (Figure 6.3(g-i)) Joule heating stops and the Bi melting circle is not changing further.

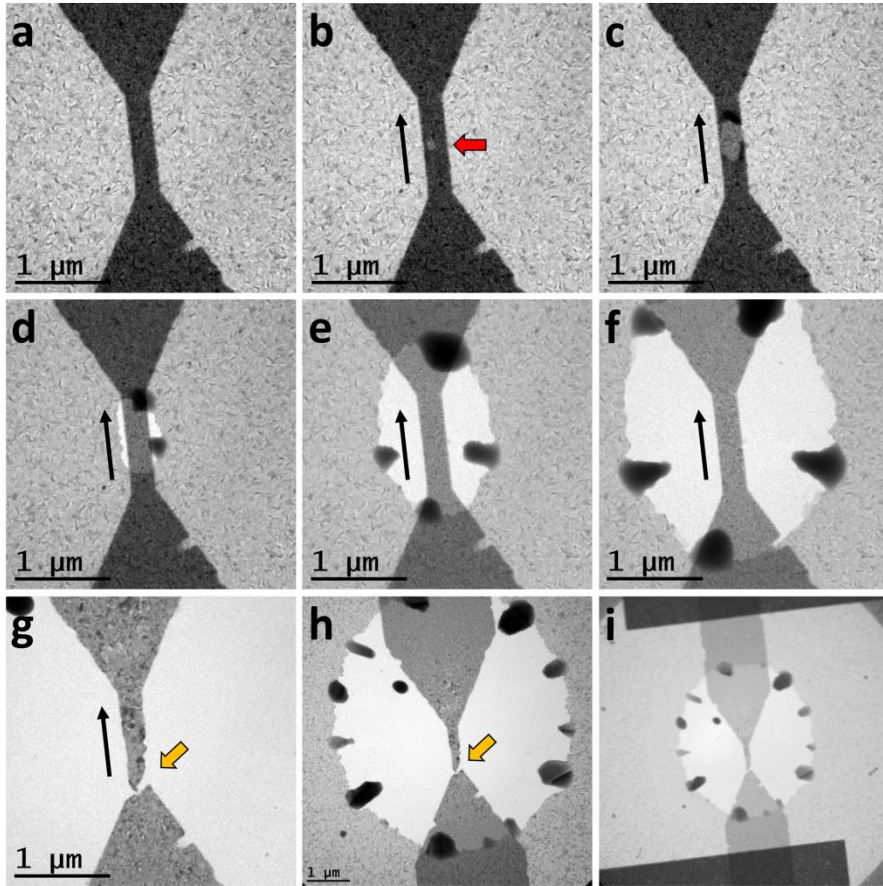


**Figure 6.3.** Snapshots from the TEM movie showing melting of deposited under the Pt nanobridge Bi film during current passage. (a) TEM image of the Pt bridge before electromigration, initial substrate temperature is 100 K. (b) The place where Bi melting starts indicated by the red arrow. Black arrow indicates the direction of electrons. (c-f) Melting circle growth due to the temperature raise with current increase. (g-i) TEM images of the bridge right after the breakage at different scales, the place of breakage is indicated by the yellow arrow.

The temperature profile created by electric current depends on the Joule heating and the rate of energy loss to surroundings. In experimental structures considered in Figure 6.3 the narrowest part (Pt bridge) experiences highest Joule heating (due to the biggest current density), Pt contact pads act as a heat sinks. But the temperature profile is not symmetric with respect to the bridge and slightly shifted toward the anode side (Figure 6.3(i)). It can be explained by non-symmetrical bridge positioning with respect to the Au contacts during structure fabrication, while they also act as a heat sinks.

### 6.3.3. Electromigration at $T_s = 300$ K

Electromigration at  $T_s = 300$  K shows similar results as at  $T_s = 100$  K: The bridge breaks close to the cathode side due to neck formation. Simultaneously with the neck formation, voids also form on the negative contact pad at 850 mV. The starting bridge resistance is higher than that at  $T_s = 100$  K due to higher substrate temperature. During imaging, a carbon contamination ring was formed due to the e-beam illumination of nanobridge, which resulted in a non-infinite measured resistance after the bridge breakage (see Figure 6.4). In order to prevent contamination the substrate temperature should be lowered to  $\sim 100$  K or raised to 420 K or more.

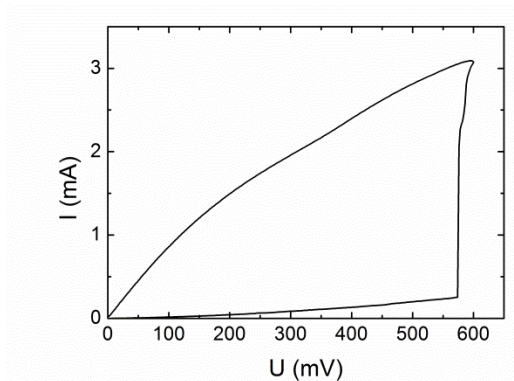


**Figure 6.4.** I–V curve for the voltage cycle applied to the bridge at RT substrate. After the bridge breakage at 600 mV the total structure resistance is not infinite, but approximately 3 kOhm.

### 6.3.4. Electromigration at $T_s = 420$ K

Figure 6.5(a–e) shows snapshots of the real-time STEM movie recorded during bias ramping at  $T_s = 420$  K. To identify thickness changes due to Pt displacement, high-angle STEM imaging was used, which allowed the visualisation of material transfer, i.e. the thicker the area, the brighter it appears in the STEM image<sup>12</sup>. Six voltage loops with the maximum voltages in the range of 500 – 850 mV were applied in a row. Figure 6.5(g) shows the positive half-cycles of corresponding  $I$ – $V$  curves. The wide arrow indicates the shift of  $I$ – $V$  curves during annealing, which corresponds to the differential resistance decrease with each voltage cycle. The differential resistance starts to diminish at approximately 350 mV, suggesting that the temperature at that point reaches the GB's improvement temperature. Note that this voltage is higher than for the sample at  $T_s = 100$  K, which is due to the different membrane thickness, i.e. 100 nm for 100 K vs 600 nm for 420 K. For better visualisation of resistance changes after each voltage cycle, current values were plotted separately along the line  $U = 300$  mV (dashed line in Figure 6.5(g)). Figure 6.5(h) shows the result, from which it is clear that the current achieved in each subsequent cycle increases, and this indicates the decrease in the resistance.

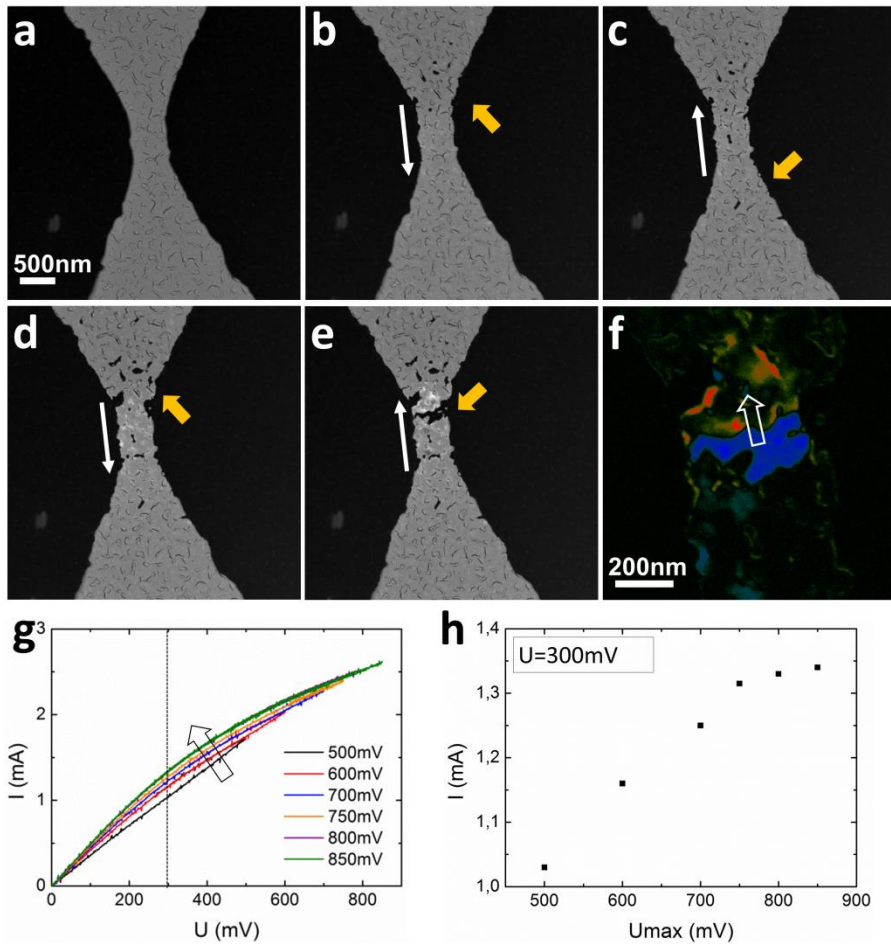


**Figure 6.5.** Snapshots from the STEM movie showing material transfer during electromigration at  $T_s = 420$  K. (a) STEM image of the Pt bridge before electromigration. (b–d) Yellow arrows indicate the formation of voids at the cathode side; white arrows indicate the direction of electrons from the cathode (–) to the anode (+) side. (e) STEM image of the bridge right after the breakage, the place of breakage is indicated by the yellow arrow. (f) The result of subtraction images (e) and (d), i.e. only the central part of the bridge, is shown in a colour-coding schema. (g)  $I$ – $V$  curves for several loops (only positive part shown) in the bias-ramping mode; different colours in the plot correspond to each subsequent loop with gradually increased maximum voltage;  $I$ – $V$  curves shift due to the GG, shown by the wide arrow. (h) Current values taken at 300 mV as a function of maximum voltages applied in corresponding cycles, i.e. current value taken along the dashed line in the inset.

Figures 6.5(b–c) and (d–e) correspond to the two last voltage loops with the maximum voltages 800 and 850 mV where the material transfer is clearly visible. In Figure 6.5(b) voids can be seen on the contact pad near the cathode side (shown by a yellow arrow) and the contrast changes indicate that the removed material transferred toward the bridge centre (in

the direction of electron wind). This formation of voids occurs at approximately 2 mW (800 mV and 2.5 mA). Note that this is observed during continuous voltage increase, and that with a constant voltage over a longer time, voids form at a lower voltage. After the polarity is reversed, existing voids are not refilled as in the case of a Pd–Pt alloy<sup>11</sup>, but additional holes form near the new cathode side, Figure 6.5(c). During the next  $U(\text{max}) = 850$  mV cycle, the existing voids grow, new ones form and removed material accumulates within the bridge, Figure 6.5(d), forming hillocks. These thicker areas appear as brighter areas in the bridge. During the second half of the  $U(\text{max}) = -850$  mV cycle, the bridge broke, Figure 6.5(e). For better visualisation of material transport, we subtracted two images taken after and just before the break occurred, Figures 6.5(e) and (d), respectively. Figure 6.5(f) shows the result of the subtraction (only the central part of the bridge) in colour-coding schema: The blue region indicates the area from which material was transferred; the red and yellow areas represent the formed hillocks, i.e. the thick area. The direction of material transfer indicated by white arrows corresponds to the electron wind from the cathode to the anode side.

### 6.3.5. Electromigration at $T_s = 660$ K

Figure 6.6(a–g) shows snapshots from the TEM movie of the electromigration process at  $T_s = 660$  K. Note that at this temperature, which is higher than the GG start at  $260^\circ\text{C}$ <sup>10</sup>, grain growth occurs so rapidly, i.e. the grains reach their maximum size in just 3 minutes, that this electromigration study starts with a nanobridge with fairly large grains (the bridge was kept at 660 K before the start of electromigration). The maximum voltage is 700 mV in the first cycle shown, Figure 6.6(b–c), 750 mV in the second cycle, Figure 6.6(d)–(e) and 800 mV in the third cycle, Figure 6.6(f–g). The bridge breaks at 700 mV during the second half of the third cycle.

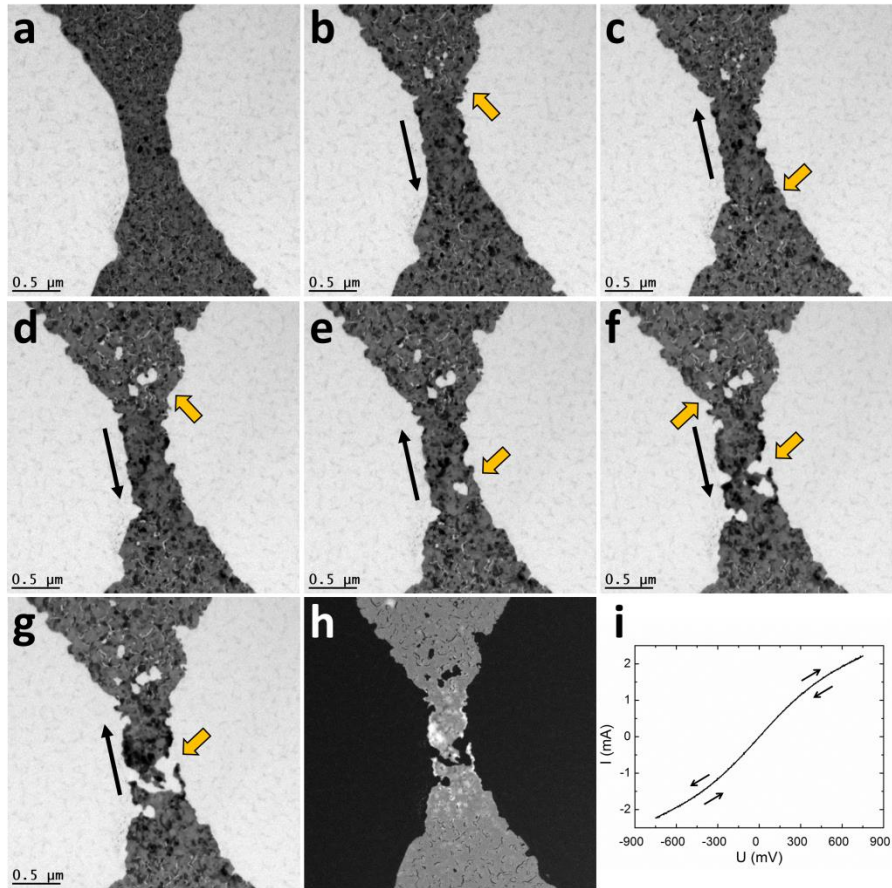


**Figure 6.6.** Snapshots from the TEM movie showing the bridge break during electromigration at 660 K. (a) Initial TEM view of the Pt bridge at 660 K. Yellow arrows indicate voids forming at the cathode side (b–e). Upon polarity change, voids are not refilled and additional ones form at the cathode side. Black arrows indicate the direction of electrons. (f) At sufficiently high temperatures, voids form on both sides of the bridge. (g) TEM and (h) STEM images of the broken bridge, the place of breakage is indicated by yellow arrow. (i) Typical  $I$ - $V$  curve for one loop in the bias-ramping mode.

As in the experiment at 420 K, Figure 6.5, voids start to form near the cathode side but at lower power  $\sim 1.4$  mW (700 mV and 2 mA). In the last 800 mV cycle, which corresponds to sufficiently high temperatures, voids form on both sides of the bridge. Voids are not refilled when the voltage polarity is changed; rather, the material is transported in the direction of electrons and piles up near the bridge centre, see the STEM image after the breakage in Figure 6.6(h). Figure 6.5(i) shows the  $I$ - $V$  curve of the  $U(\text{max}) = 750$  mV voltage loop. The  $U(\text{max}) = 800$  mV cycle follows the same curve in the first half, confirming the absence of grain growth.

### 6.3.6. Critical power of the bridge break

Our experiments show that, with an increase of the substrate temperature, we need a lower current as well as a lower voltage for voids to occur, a neck to form and the nanobridges to break, see Figure 6.7. This is to be expected because the higher temperature adds potential energy to the atoms so they can easily overcome the crystal lattice energy barrier and leave their original positions. Note that the critical current, voltage and power values can vary from sample to sample due to different biasing history. If the bridge broke during the first cycle, the breakage power is relatively high. While if the bridge was preliminary deformed by passing the current which is not enough to cause the bridge breakage (like in Figure 6.6(f)), that system can break in the next voltage cycle at lower power.

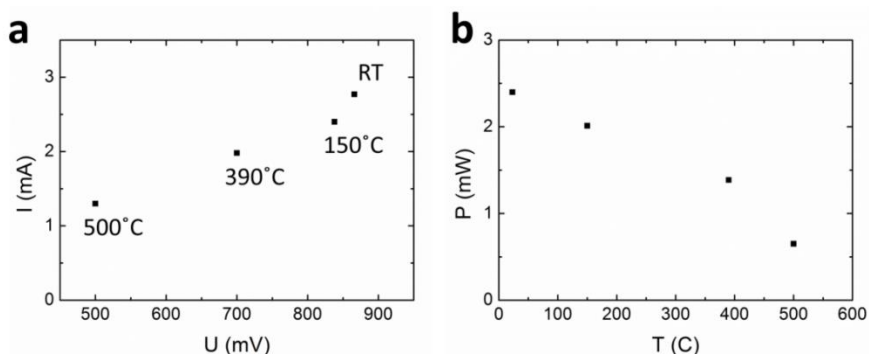


**Figure 6.7.** (a) Critical current and voltage parameters for different ambient temperatures of the bridge. (b) Critical power versus temperature.

### 6.3.7. Comparison of different substrate temperature regimes

When the substrate temperature is below the GBs improvement temperature and the GG temperature, the effect of passing a current causes these phenomena first, resulting in a change of the resistance. If the substrate temperature is above the GG temperature, the only effects on the resistance are Joule heating and the displacement of Pt, i.e. Pt removal from the voids and the neck and subsequent deposition of this Pt elsewhere results in hillocks. These hillocks form primarily in the middle of the bridge. This material rearrangement will increase the resistance locally near voids and the neck and decrease it near the hillocks. As the total bridge resistance can be considered a combination of resistances including the areas of voids and hillocks, it is not easy to predict whether these shape changes lead to an overall increase or decrease of the resistance. In general we see almost no effect of the material rearrangement in the early part of this process.

Figure 6.8 shows a schematic view of the bridges after breaking at  $T_s = 100, 420$  and  $660$  K. To summarise, in all substrate temperature regimes the bridges start to form a neck near the cathode side and the neck becomes narrower until the nanobridges break. During electromigration at  $300, 420$  and  $660$  K, voids form at the cathode contact pad roughly

simultaneously with the neck, whereas no voids form at 100 K. The voids are much bigger in the case of electromigration at 660 K than at 420 or 300 K. As a result, the volume of deposited material is greater in the case of  $T_s = 660$  K. The material of the voids and part of the neck accumulates in the bridge central area.

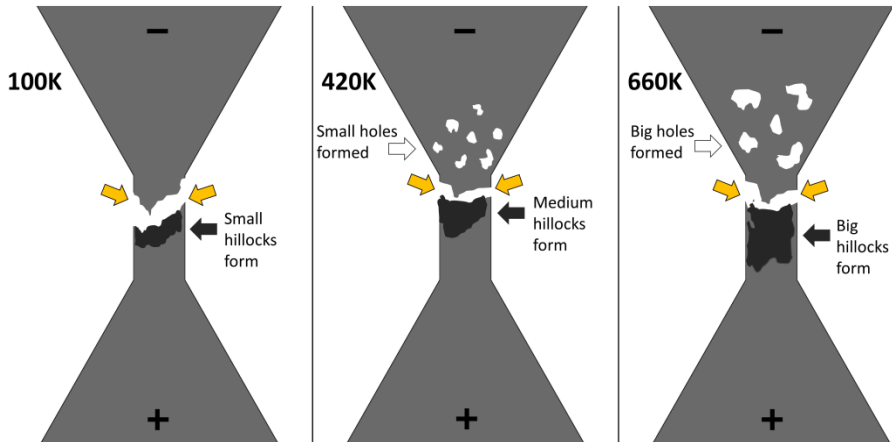


**Figure 6.8.** Schematic view of the bridge after breaking at temperatures 100, 420 and 660 K. Voltage polarity, locations of holes and hillocks as well as the place of breakage are indicated.

The non-reversible process of voids and neck formation can be caused by high nanobridge temperatures due to substrate and Joule heating, the film tends to minimise the surface energy<sup>19</sup>. In the absence of a current no void formation was observed at temperatures up to 500°C<sup>10</sup>, so we concluded that voids formation starts at higher temperatures. Locations of voids and neck depend on the bias polarity, which indicates the influence of the electromigration effect on bridge breakage. However, we did not observe a preferential direction of voids growth.

### 6.3.8. Change of the bridge resistance due to the grain growth

To determine the resistance evolution due to grain growth without the effect of resistance increase due to Joule heating, the bridge resistance was measured as a function of the maximum voltage applied in a bias-ramping cycles. Figure 6.9(a) shows the results of Joule heating at  $T_s = 300$  K for two different nanobridges: (I) an as-prepared nanobridge with small grains, (II) a nanobridge with big grains formed during two preceding heating cycles of annealing to 770 K by substrate heating only. Resistance measurements after each voltage cycle were taken at very low voltage to prevent Joule heating. The initial resistances of the two nanobridges are not identical, which is due to the difference in the grain sizes.

For nanobridge I the resistance remains constant until the voltage cycle of 400 mV, where it starts to drop. Upon following higher-voltage cycles, the resistance continues to drop

due to further GG. Before the breakage, the resistance reaches 130 Ohm at 900 mV, corresponding to a resistance drop of 37%. This result is in good agreement with previous studies<sup>10,16</sup> of a 30% of resistance drop during bias-ramping applied to polycrystalline Pt bridges of similar dimensions. For nanobridge II the initial resistance is 162 Ohm and this value is observed to be constant up to the 700 mV cycle. During the cycle with a maximum voltage of 800 mV, the resistance decreases until 150 Ohm. Nanobridges I and II broke in the tenth cycle at 950 mV and in the ninth cycle at 850 mV, and the resistance became infinite. Comparing the two bridges, we find that the resistance of Nanobridge I decreases during the cycle with a maximum voltage of 400 mV, and the resistance of Nanobridge II decreases during the 700 mV cycle. We conclude that 400 mV voltage corresponds to the temperature at which the GBs improve and GG starts, i.e. 150–260°C, and 700 mV corresponds to the voltage at which the temperature of the bridge reaches 500°C and additional GG occurs.

Figure 6.9(b) shows  $I$ - $V$  values plotted for bias-ramping cycles for nanobridge I with maximum voltages of 300, 400, 600 and 800 mV. The resistance decrease corresponds to the  $I$ - $V$  slope increase indicated by the wide arrow in Figure 6.9(b). Moreover, it should be noted that the voltage increase and decrease in the first half of each bias-ramping cycle do not follow the same line, see the inset in Figure 6.9(b), indicating a small resistance reduction due to GG. A similar resistance decrease, i.e. an increase of the  $I$ - $V$  slope, can be seen in Figure 6.5(g) during electromigration at 420 K. Figure 6.9(c) shows  $I$ - $V$  for the 600 mV cycle; the voltage increase and decrease follow the same line, indicating no GG during that cycle.

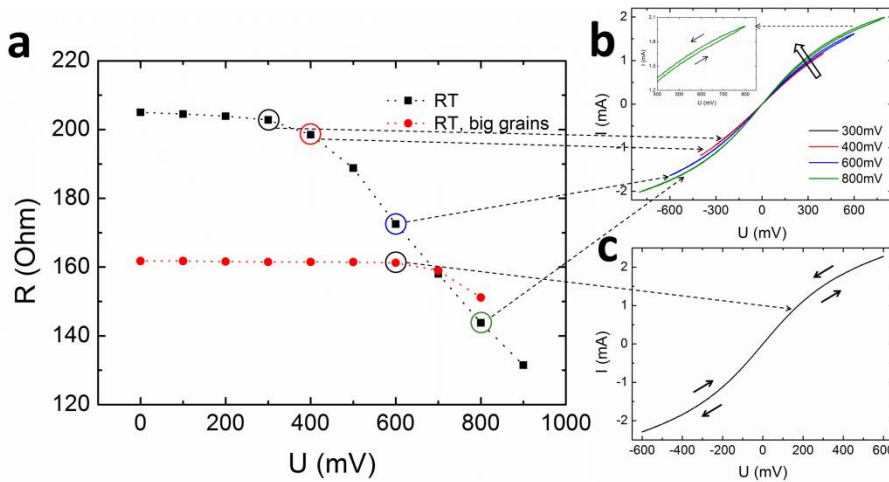


**Figure 6.9.** (a) Bridge resistance at RT and low voltage as a function of the maximum voltage applied in a bias-ramping cycle. The data points correspond to two different bridges – as-fabricated (black squares) and big grains formed after two preliminary heating cycles (red circles). (b)  $I$ - $V$  curves of the voltage cycles applied to the as-fabricated bridge with maximum values 300, 400, 600, 800 mV; the wide arrow indicates the direction of slope change. Inset: magnified view of the 800 mV cycle near the maximum voltage value. (c)  $I$ - $V$  curve of the voltage cycle (up to 600 mV) applied to the bridge with the big grains; directions of voltage increase/decrease marked by arrows.

## 6.4. Conclusions

We have presented a combination of local substrate heating and electromigration experiments. This new combination of using a MEMS heater to heat the substrate under the Pt nanobridge and electrical leads to perform electrical measurements allow for *in situ* TEM experiments on the electromigration at a range of temperatures. The electromigration experiments were performed at 100, 300, 420 and 660 K, but other temperatures can also be used. To our knowledge, there are no previously reported *in situ* electromigration experiments at high ambient elevated temperatures.

At high substrate temperatures we found the similar tendency of material transport from the cathode side due to electron-wind force as at liquid nitrogen temperature. At temperatures higher than 300 K, voids formation is enhanced near the contact pad at the cathode side. These voids are not refilled when the polarity of the bias voltage is changed. In the case of a substrate temperature increase, the process of voids formation is enhanced. In addition, we estimated the critical power at which the bridge breaks, and the results show that a lower power is needed to break the nanobridge at higher substrate temperatures.

The local nanobridge temperature during current passage was measured by using low melting Bi thin film deposited on the back side of SiN membrane. The temperature profile was shown to be dependent on the bridge positioning with respect to Pt and Au contacts.

## References

- 1 Ho, P. S. & Kwok, T. Electromigration in Metals. *Rep Prog Phys* **52**, 301-348, doi:Doi 10.1088/0034-4885/52/3/002 (1989).
- 2 Huntington, H. B. in *Diffusion in solids* (ed A.S. Nowick) (Academic Press, INC., 1975).
- 3 Barnat, E. V., Nagakura, D., Wang, P. I. & Lu, T. M. Real time resistivity measurements during sputter deposition of ultrathin copper films. *J App Phys* **91**, 1667-1672 (2002).
- 4 Zhang, W. *et al.* Influence of the electron mean free path on the resistivity of thin metal films. *Microelectronic Engineering* **76**, 146-152 (2004).
- 5 Lacy, F. Developing a theoretical relationship between electrical resistivity, temperature, and film thickness for conductors. *Nanoscale Research Letters* **6**, 1-14, doi:Doi 10.1186/1556-276x-6-636 (2011).
- 6 Thompson, C. V. Structure evolution during processing of polycrystalline films. *Annual Review of Materials Science* **30**, 159-190, doi:DOI 10.1146/annurev.matsci.30.1.159 (2000).

- 7 Holm, E. A. & Foiles, S. M. How Grain Growth Stops: A Mechanism for Grain-Growth Stagnation in Pure Materials. *Science* **328**, 1138-1141, doi:DOI 10.1126/science.1187833 (2010).
- 8 Burke, J. E. & Turnbull, D. Recrystallization and Grain Growth. *Progress in Metal Physics* **3**, 220-292, doi:Doi 10.1016/0502-8205(52)90009-9 (1952).
- 9 Rost, M. J., Quist, D. A. & Frenken, J. W. M. Grains, Growth, and Grooving. *Phys. Rev. Lett* **91**, 4 (2003).
- 10 Kozlova, T., Ruitenbeek, J. M. & Zandbergen, H. W. The origin of increased resistivity in platinum nanobridges studied by *in situ* TEM. *in prep.* (2015).
- 11 Kozlova, T., Rudneva, M. & Zandbergen, H. In situ TEM and STEM studies of reversible electromigration in thin palladium-platinum bridges. *Nanotechnology* **24**, 505708 (2013).
- 12 Rudneva, M., Kozlova, T. & Zandbergen, H. The use of STEM imaging to analyze thickness variations due to electromigration-induced mass transport in thin polycrystalline nanobridges. *Ultramicroscopy* **134**, 155-159, doi:10.1016/j.ultramic.2013.05.022 (2013).
- 13 van Huis, M. A. *et al.* Atomic Imaging of Phase Transitions and Morphology Transformations in Nanocrystals. *Advanced Materials* **21**, 4992, doi:DOI 10.1002/adma.200902561 (2009).
- 14 Martin, C. A., Smit, R. H. M., van Egmond, R., van der Zant, H. S. J. & van Ruitenbeek, J. M. A versatile low-temperature setup for the electrical characterization of single-molecule junctions. *Rev Sci Instrum* **82**, 053907, doi:Doi 10.1063/1.3593100 (2011).
- 15 Rudneva, M. *et al.* In-situ transmission electron microscopy imaging of electromigration in Pt nanowires. *Microscopy and Microanalysis* **11** (2012).
- 16 Gao, B. *et al.* In situ transmission electron microscopy imaging of grain growth in a platinum nanobridge induced by electric current annealing. *Nanotechnology* **22**, doi:Doi 10.1088/0957-4484/22/20/205705 (2011).
- 17 Zayed, M. K. & Elsayed-Ali, H. E. Melting and solidification study of as-deposited and recrystallized Bi thin films. *J Appl Phys* **99** (2006).
- 18 Gladkikh, N. T., Bogatyrenko, S. I., Kryshchal, A. P. & Anton, R. Melting point lowering of thin metal films (Me = In, Sn, Bi, Pb) in Al/Me/Al film system. *Applied Surface Science* **219**, 338-346 (2003).

- 19 Thompson, C. V. Solid-state dewetting of thin films. *Annu. Rev. Mater. Res.* **42**, 399-434 (2012).



---

# Chapter 7

---

## Towards *in situ* TEM Investigations of Nanoparticles under Dynamic Conditions

This chapter is devoted to prospective of *in situ* TEM observations of nanoparticles under dynamic conditions, *i.e.* heating and current passage. We chose spin-crossover materials as model object to analyse, their imaging was done using STEM-HAADF mode in order to enhance contrast and minimise beam damage. Spin-crossover nanoparticles can be positioned between metallic contacts created on top of the MEMS heater using a dielectrophoresis method. The steps toward a correlation of the morphology of such nanoparticles simultaneously with the memory effect features in the conductivity will be described. Finally, we touch upon the remaining challenges and future directions to follow.

This chapter is based on: Dugay, J.; Gimenez-Marques, M.; Kozlova, T.; Zandbergen, H.W.; Coronado, E.; van der Zant, H.S. *Spin switching in electronic devices based on 2D assemblies of spin-crossover nanoparticles*. *Advanced Materials* **2015**, *27*(7), 1288-93

## 7.1. Introduction

Combination of electrical measurements and heating/cooling experiments with *in situ* TEM imaging is of high importance in various fields of research, one of them is molecular electronics. Indeed, metallic nanogap electrodes formed on a MEMS heater can be used as contacts to the trapped particles or molecules, allowing their shape transformations to be visualised while measuring their electrical properties during heating/cooling temperature cycles. It should be noted that Pt electrodes already proved to be a promising material to achieve a better thermal stability of the nanogaps due to its lower surface mobility compared to that of gold<sup>1</sup>.

As a promising system for analysis, spin-crossover (SCO) materials can be concerned. In SCO materials the spin state changes from their ground state (low-spin state;  $S = 0$ ) to a metastable state (high-spin state;  $S = 2$ ) due to external stimuli, *i.e.* temperature, magnetic field, pressure or light irradiation change<sup>2-5</sup>. Due to elastic interactions between neighbouring SCO molecules, a thermal hysteresis cycle can be observed which leads to their potential memory applications in electronic devices<sup>6,7</sup>. A decrease in size of the SCO solid to the nanoscale should be done together with preserving the important memory effect near room temperature. Nanoparticles (NPs) made of  $[\text{Fe}(\text{Htrz})_2(\text{trz})](\text{BF}_4)$ , (Htrz = 1,2,4-triazole) are one of the most promising SCO systems as they present a large hysteresis loop ( $\sim 40\text{K}$ ) above room temperature<sup>8,9</sup>.

A challenging combination of electrical measurements during temperature increase with *in situ* TEM observations is expected to lead to a deeper understanding of the link between the memory effect features in the conductivity and the NPs morphology/assembling (*i.e.*, role of the metal-centers interactions within/between nanoparticles) and orientation (electrons flowing along/perpendicular to the metal-center chains). It could also reveal the smallest molecular network dimension retaining a memory effect in the conductivity.

A first step has been achieved in our work "Spin switching in electronic devices based on 2D assemblies of spin-crossover nanoparticles",<sup>10</sup> where we investigated the electrical transport properties of two-dimensional assemblies of  $[\text{Fe}(\text{Htrz})_2(\text{trz})](\text{BF}_4)$  SCO NPs with two different morphologies. By combining HAADF-STEM imaging with the electrical measurements (performed by means of a probe station), we correlated for the first time the shape of the thermal hysteresis loop in conductivity with the individual NPs morphology and their global arrangement. All details about NPs synthesis and electrical measurements can be found in the above-mentioned paper. Further in this Chapter the perspectives of *in situ* TEM studies and the achieved progress in that direction towards electrical investigation and visualization of spin-crossover nanoparticle(s) inside a TEM are discussed.

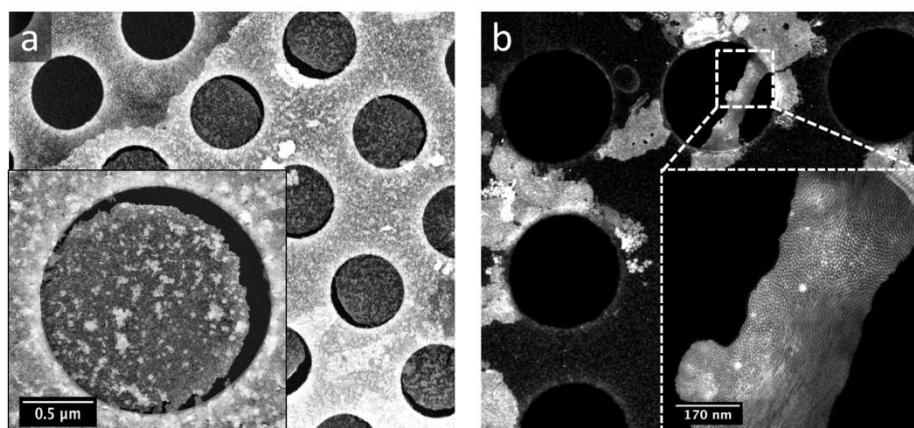
## 7.2. Achievements and difficulties in *in situ* TEM molecular electronic properties investigations

### 7.2.1. Visualisation of SCO NPs using TEM

The visualization of the SCO NPs was done using a FEI Titan microscope operating at 300 keV. In BF TEM mode only low-contrast images could be obtained due to very strong signal coming from central beam because many electrons pass through the SCO NPs without scattering. One of the typical BF TEM images of the SCO NPs is shown in Figure A7.1 in Appendix A7.

STEM imaging was used for two reasons: 1) to get a much better contrast and 2) to reduce the damage by the electron beam. Using a HAADF detector a high contrast was achieved due to enhancement of mass–thickness contrast which leads to sufficient difference between high intensity NPs separated by almost no-intensity gaps <sup>11</sup>. The reduction of electron beam induced damage by using STEM is generally observed and must be due to the use of a very narrow electron beam (e.g. 0.2 nm) versus a very broad beam (e.g. 200 nm and higher).

Free-standing ultrathin sheets of two batches of SCO NPs were prepared on top of holey carbon TEM grids. These sheets are composed of self-assembled monolayers of the SCO NPs, which were initially formed at a diethyleneglycol/octane interface and subsequently transferred on holey carbon grids using a stamping technique <sup>12</sup> or drop-casting method (see Figure 7.1).



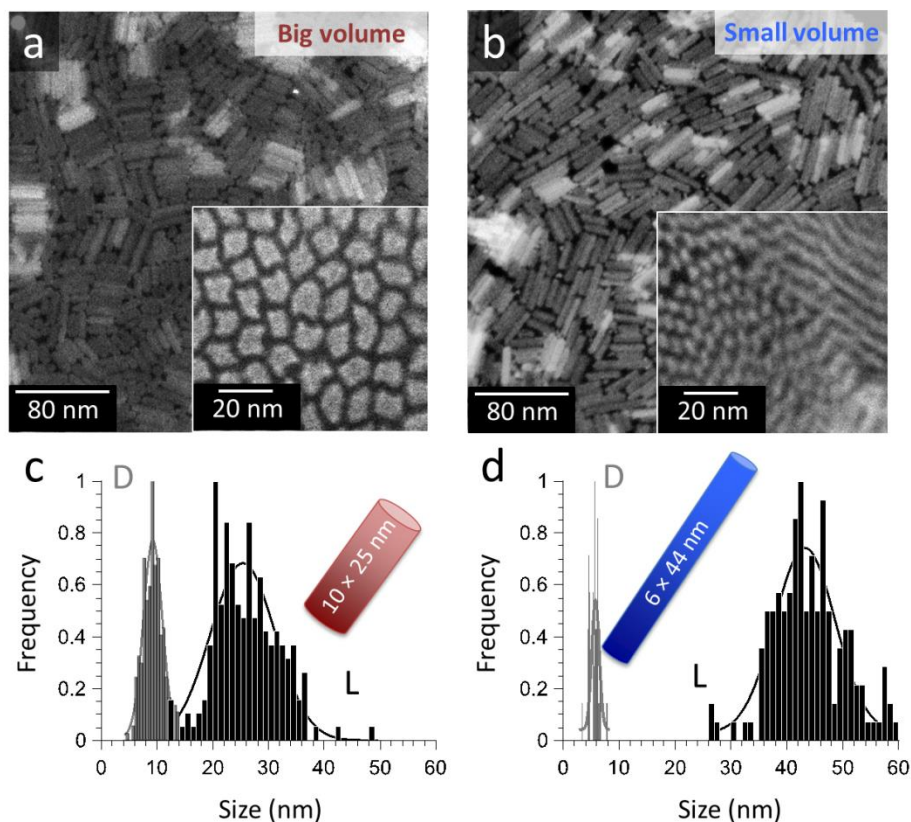
**Figure 7.1.** Low-magnification STEM-HAADF images of free-standing 2D sheets of SCO NPs prepared by stamping technique (a) and by drop-casting method (b) on holey carbon TEM grids. Insets show higher magnification of the free-standing sheets. Magnified views of this system are presented in Figure 7.2 (a).

Figure 7.2(a-b) shows STEM–HAADF images of the self-assembled monolayers of NPs with two different morphologies prepared by a stamping method. Both NPs display a rod-like shape, their size distribution analysis was done by means of the free ImageJ software<sup>13</sup>.

To get more detailed information of the cross sectional shapes of the NPs, free-standing sheets of vertically self-assembled monolayers were formed by means of a drop casting method on holey carbon TEM grids. At the locations of the holes in the C film, such a deposition method indeed promoted the formation of assemblies of NPs where the rod direction is parallel to the electron beam (see insets in Figures 7.2(a-b))<sup>14</sup>.

The two viewing directions allow for an accurate determination of the sizes of the two NPs batches (see size distribution analysis, Figure 7.2(c-d)). The SCO NPs systems possess two different volumes ( $V \approx 1960$  and  $1240 \text{ nm}^3$ , respectively) corresponding to lengths of 25 nm and 44 nm along the rod direction and average diameters of 10 nm and 6 nm, respectively.

Because the obtained single crystals are needle-shaped, we assumed that the rod-like shape of the NPs is linked to the chain-like structure of the family of iron(II)-triazole complexes, with the chains aligned along their longest dimension. Both NPs prepared by a stamping method are organized parallel to the sheet, which must be due to the strong capillary forces induced by the octane thin film during evaporation.



**Figure 7.2.** (a-b) STEM-HAADF images of free-standing 2D sheets of SCO NPs prepared by stamping technique. Insets show lateral self-assembly of NPs obtained by a drop-casting method. (c-d) Distributions of NPs diameters (D:  $9 \pm 3$  and  $6 \pm 2$  nm) and lengths (L:  $25 \pm 12$  and  $44 \pm 11$  nm) for SCO NPs systems referred to as 25/10 (big volume) and 44/6 nm (small volume).

### 7.2.2. Nanoparticles trapping

Prior to the NP electrical properties investigations, measurement contacts should be created. For the small NPs (with size around several nanometres) nanogaps can be made from the bridges using electromigration in FBC mode (Chapter 3, Figure 3.6). For bigger NPs, standard lithography can be implemented or gaps can be created by cutting of existing bridges with the focused ion beam (FIB) (typical minimum gap size is around 100 nm). A FIB cut would also give the advantage to measure a free-standing NP, avoiding interactions between the membrane and particle.

Figure 7.3 shows an example of hybrid  $([\text{Fe}(\text{Htrz})_2(\text{trz})](\text{BF}_4))$  SCO NPs stabilized by a  $\text{SiO}_2$  shell trapped via dielectrophoresis method between metallic electrodes (AC field trapping  $V_{pp} = 3$  V, frequency 10 kHz). The length of NPs is approximately 100 nm. Figure 7.3(a) presents a Pt nanogap created using electromigration where the distance between

electrodes is 10 nm. Figure 7.3(b) shows a larger gap created by a FIB cut. It should be noted, that when cutting is done from the top view, the actual distance between electrodes is bigger (200 nm) than the set value (100 nm) due to different sputtering rates between Pt and SiN and the beam spread. If the cutting is performed from the backside, the set value becomes equal to the real contact distance. In demonstrated examples the thickness of silicon nitride membrane under the bridge is 100 nm, which reduce their contrast in comparison with free-standing sheets.

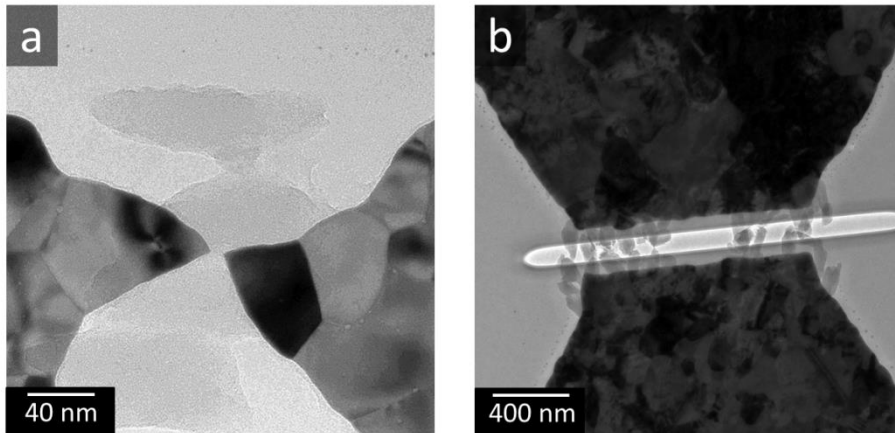


**Figure 7.3.** TEM images of NPs trapped between Pt contacts formed using FBC electromigration break (a) and FIB cutting (b).

As a first step, transport measurements of trapped particles shown in Figure 7.3(a) were done in a probe station. Figure 7.4 shows the NPs conductivity during three cycles of substrate temperature change. Thermal hysteresis loops in the conductance were obtained during sample heating with subsequent cooling. Transition from low-spin state to high-spin state during heating occurs at 357K, while during cooling opposite transition occurs around 340 K. It should be mentioned that in order to be above the electrical current detection limit, for described system at least 4 V voltage should be applied.

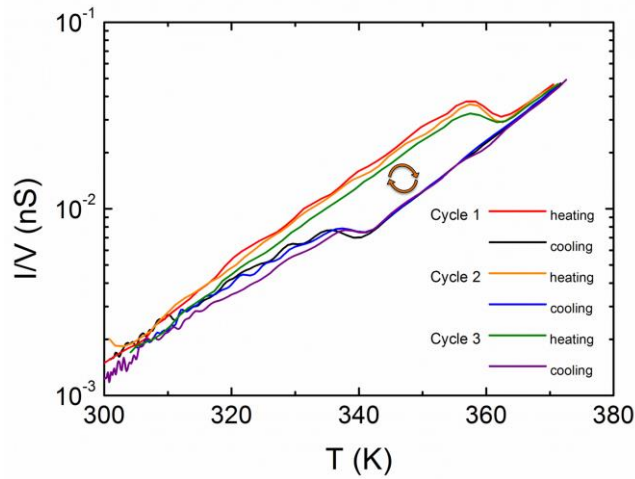


**Figure 7.4.** NPs conductivity change during 3 cycles of sample heating with subsequent cooling.

In order to measure the NPs resistance while heating together with TEM imaging, the holder for electrical measurements can be used. Initially, the system can be cooled to 100 K by placing the copper wires connected to the holder in a dewar filled with liquid nitrogen (for more details see Chapter 2 sections 2.3.1 and 2.3.3). As a substrate heating chips with bridges on top of it (cutted by FIB to produce the electrical contacts) should be used (Chapters 5 and 6).

### 7.2.3. Remaining challenges

For *in situ* TEM electrical properties investigations following difficulties can be listed: beam damage of structures, carbon contamination and contrast lowering due to SiN supporting membrane. Because of the NPs sensitivity to the beam, an accurate TEM observation remains a challenge. In this context, a compromise between dose lowering and a good signal to noise ratio should be found. We demonstrated that STEM imaging mode helped to diminish the damaging consequences of electron beam illumination for these NP systems.

Carbon contamination of investigated structures is another issue. It leads to a shortcut through the contamination ring and also carbon gradually reduces the contrast from the investigated structure. The contamination can be prevented by lowering the temperature down to 100 K or by heating the structures till 430 K. Sample cooling results in an ice formation (see Figure A7.2 in Appendix A7), which can be melted under the beam. But cooling can also lead to the nanogaps retraction, which can cause electrical contact breakage. NPs heating till 430 K before the imaging can lead to their damage because the critical temperatures for this kind of SCO compounds is between 340-380 K.

In order to receive the highest signal from NPs the substrate thickness should be minimized, in ideal case free-standing structures should be investigated. Figures 7.5 (a) and (b) show the images of SCO NPs on top of 100 nm and 20 nm SiN membrane, correspondingly. It's clear that 100 nm SiN is too thick to obtain the structural information from the sample, while 20 nm allows a proper signal to be recorded.

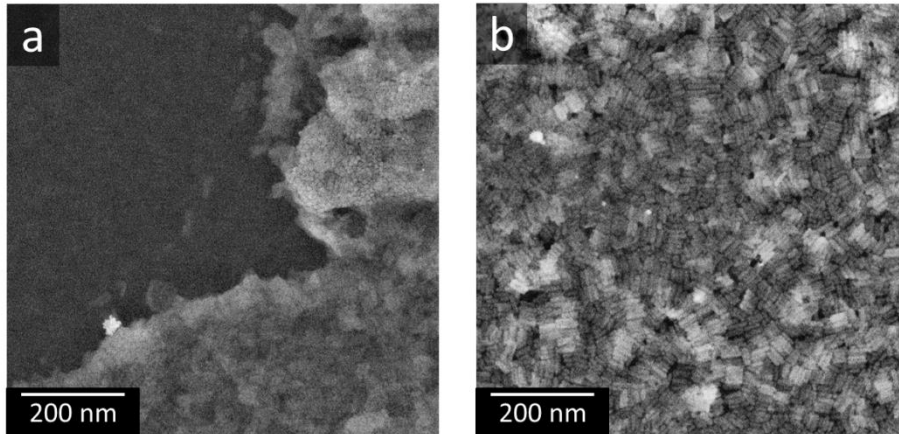


**Figure 7.5.** STEM images of sheets of SCO NPs prepared by stamping technique on top of (a) 100nm SiN membrane and (b) 20 nm SiN membrane.

Current heating chips patterned with electrical contacts on top of them have 400-nm-thick SiN membrane (the heating spiral is covered with 200 nm layers from both sides). The membrane can't be just simply thinned down by reactive ion etching (it will uncover the heating spiral and lead to the sample break due to induced stress). A possibility is to make a complete FIB cut from the back side, but this method requires addition of the alignment markers on the back side. Another solution can be the use of back-side lithography to local membrane removal under the nanogaps, this approach requires additional steps in fabrication process. Using back-side lithography free-standing contacts with several nanometers gaps can be created.

### 7.3. Conclusions

In summary, *in situ* TEM investigations of the thermal hysteresis loop in the conductivity of SCO NPs might be possible in the near future. Indeed, the use of a special TEM electrical holder and designed MEMS chips allow to perform electrical measurements while heating. STEM-HAADF imaging already successfully revealed the morphology of individual SCO NPs as well as their global arrangement. The positioning of the NPs between nanogaps produced by electromigration or FIB milling has been realized using dielectrophoresis method. There are

still some challenges remaining, like the membrane removal under the trapped NP or the beam influence (damage and carbon contamination) minimisation, which is now a work in progress.

## References

- 1 Prins, F., Shaikh, A. J., Esch, J. H. v., Eelkema, R. & Zant, H. S. J. v. d. Platinum-nanogaps for single-molecule electronics: room-temperature stability. **13**, 14297-14301, doi:10.1039/C1CP20555B (2011).
- 2 Gütlich, P., Goodwin, H. A., Létard, J.-F. & Guionneau, P. *Spin Crossover Transit. Met. Compd. III*. 1–19 (Springer Berlin, 2004).
- 3 Murray, K. S. & Kepert, C. J. in *SPIN CROSSOVER IN TRANSITION METAL COMPOUNDS IV* Vol. 233 195-228 (2004).
- 4 Real, J. A., Gaspar, A. B. & Muñoz, M. C. Thermal, pressure and light switchable spin-crossover materials. *Dalton Transactions*, 2062, doi:10.1039/b501491c (2005).
- 5 Gamez, P., Costa, J. S., Quesada, M. & Aromí, G. Iron Spin-Crossover compounds: from fundamental studies to practical applications. *Dalton Transactions*, 7845, doi:10.1039/b908208e (2009).
- 6 Kahn, O. & Martinez, C. J. Spin-Transition Polymers: From Molecular Materials Toward Memory Devices. *Science* **279**, 44-48, doi:10.1126/science.279.5347.44 (1998).
- 7 Larionova, J. *et al.* Towards the Ultimate Size Limit of the Memory Effect in Spin-Crossover Solids. *Angewandte Chemie* **120**, 8360–8364, doi:10.1002/ange.200802906 (2008).
- 8 Aromí, G., Barrios, L. A., Roubeau, O. & Gamez, P. Triazoles and tetrazoles: Prime ligands to generate remarkable coordination materials. *Coordination Chemistry Reviews* **255**, 485-546, doi:10.1016/j.ccr.2010.10.038 (2011).
- 9 Roubeau, O. Triazole-Based One-Dimensional Spin-Crossover Coordination Polymers. *Chemistry – A European Journal* **18**, 15230–15244, doi:10.1002/chem.201201647 (2012).
- 10 Dugay, J. *et al.* Spin Switching in Electronic Devices Based on 2D Assemblies of Spin-Crossover Nanoparticles. *Advanced Materials* **27**, 1288-1293, doi:10.1002/adma.201404441 (2015).

- 11 Rudneva, M., Kozlova, T. & Zandbergen, H. W. The use of STEM imaging to analyze thickness variations due to electromigration-induced mass transport in thin polycrystalline nanobridges. *Ultramicroscopy* **134**, 155-159, doi:10.1016/j.ultramic.2013.05.022 (2013).
- 12 Prins, F., Monrabal-Capilla, M., Osorio, E. A., Coronado, E. & van der Zant, H. S. J. Room-Temperature Electrical Addressing of a Bistable Spin-Crossover Molecular System. *Advanced Materials* **23**, 1545–1549, doi:10.1002/adma.201003821 (2011).
- 13 Rasband, W. S. ImageJ. <http://rsbweb.nih.gov/ij/> (2008).
- 14 Baranov, D. *et al.* Assembly of Colloidal Semiconductor Nanorods in Solution by Depletion Attraction. *Nano Lett* **10**, 743-749, doi:10.1021/nl903946n (2010).

## Appendix A7

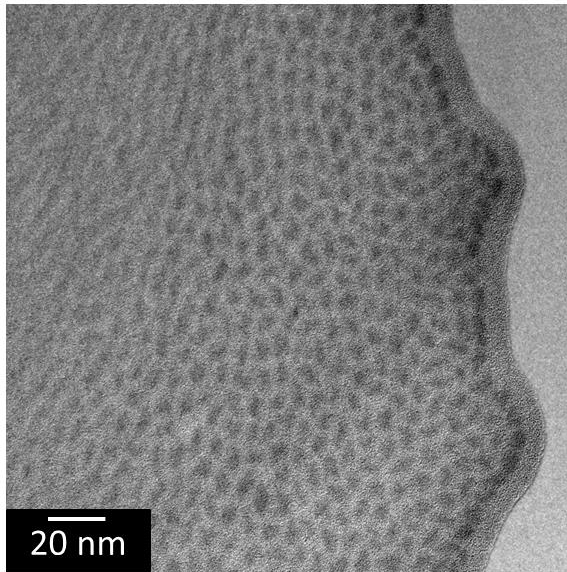


**Figure A7.1.** Typical BF TEM image of free-standing 2D sheet of SCO NPs prepared by drop-casting method on holey carbon TEM grid.

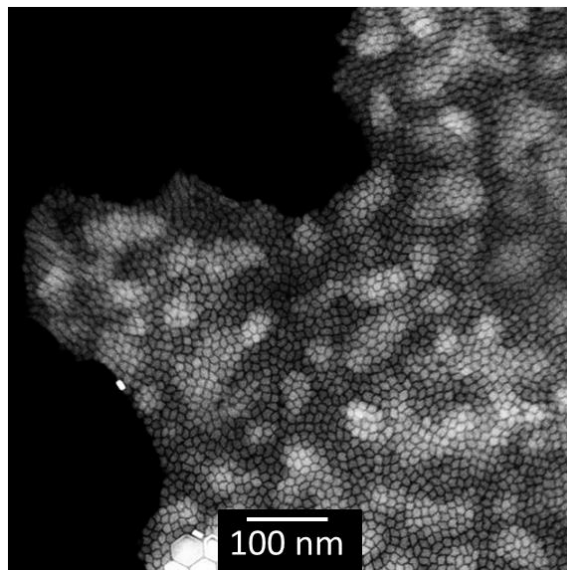


**Figure A7.2.** STEM image of free-standing sheet of NPs with ice formed on it due to the sample cooling.



# Summary

## *In situ* transmission electron microscopy investigations of electromigration in metals

Electromigration is a process in which a metallic contact line is thinned by passing a current through it; which occurs due to a gradual displacement of atoms, ultimately leading to destruction of the wire. Despite the active investigations on electromigration for over fifty years, until now there is no general theory of the process and many open questions in understanding this process at a fundamental level still remain. In order to understand the material transport under an applied electric field, many parameters should be considered: size of the structure, material, temperature, stress, microstructure (size of the grains, type of grain boundaries), and surface effects.

In this thesis, transmission electron microscopy (TEM) together with *in situ* electrical/heating measurements (which require special MEMS chips and TEM holders) was used for investigating electromigration in thin metallic (Pt, Pd–Pt alloy) nanobridges. This technique allows obtaining information about material under an applied electric field at atomic level, helping in understanding the process dynamics. In our experiments morphological transformations were recorded in real time at the nanoscale, along with the corresponding I–V while passing an electric current.

By using scanning transmission electron microscopy (STEM) imaging with high angle annular dark field (HAADF) detector, electromigration in Pd–Pt alloy nanobridges was shown to be quite different from the pure elements Pt and Pd. The electromigration of Pt and Pd is very similar: after recrystallization (also observed in Pd–Pt alloy), the bridge gradually becomes narrower and breaks. In case of alloy, the outer shape of the bridge is maintained while the material transport from the cathode to the anode is guided by the direction of electric field and is fully reversible. Material transport corresponds to the electron-wind force, indicating a negative effective charge. This principle of controllable reversible material transport in Pd–Pt alloy with the change in field polarity can be implemented in memristor applications.

The material properties under both dynamic conditions, i.e. heating and electric current passage, were investigated *in situ*. We found increased resistivity in Pt nanobridges and correlated the variation in resistance with morphological changes while heating the polycrystalline Pt films. During electromigration experiments, the bridge resistance changes due to two processes, Joule heating and electromigration. By measuring the resistance variation upon heating the substrate, these processes can be decoupled. This study also yielded the importance of surrounding temperature on the nanobridge: Despite the same tendency of material transport from the cathode to anode, higher temperature of the surroundings enhances the nanobridge breakage. The higher temperature adds potential

energy to the atoms so they can easily overcome the crystal lattice energy barrier and leave their original positions.

In general, besides describing the failure due to electromigration extensively in this thesis, the scope of expanding these *in situ* heating/electrical measurements in the TEM to other studies has been presented. For instance, developed system can be used in molecule electronic device studies of electrical properties of nanoparticles or molecules in combination with morphological changes visualizations at atomic level. It can be also implemented in memory-switching devices investigations or in one of the hot topics of lithium-ion batteries.

# Samenvatting

## *In situ* transmissie-elektronen-microscopie-onderzoek aan elektromigratie in metalen

Elektromigratie is een proces waarbij een metallische contactlijn dunner wordt doordat er stroom doorheen gaat; hetgeen ontstaat door een geleidelijke verplaatsing van de atomen, die uiteindelijk leidt tot het kapot gaan van de draad. Ondanks de vele onderzoeken naar elektromigratie in de afgelopen vijftig jaar, is er tot op heden geen algemene theorie voor het proces en blijven nog vele fundamentele vragen aangaande het begrip van het proces onbeantwoord. Om het materiaaltransport, veroorzaakt door het aangelegde elektrische veld, te begrijpen, zouden vele parameters in beschouwing genomen moeten worden: grootte van de structuur, materiaal, temperatuur, spanning, microstructuur (grootte van de korrels, type korrelgrens) en oppervlakte-effecten.

In dit proefschrift wordt transmissie-elektronen-microscopie (TEM) tegelijkertijd met in-situ-elektrische/hitte metingen (waarvoor speciale MEMS chips en TEM-houders nodig zijn) gebruikt voor het onderzoek aan dunne (Pt, Pd-Pt-legering) nanobridges. Met deze techniek is informatie over het metaal te verkrijgen terwijl er een elektrisch veld over wordt aangelegd, hetgeen helpt bij het begrijpen van de dynamica van het proces. In onze experimenten werden "live" vormveranderingen waargenomen op een schaal van nanometers samen met de corresponderende I-V karakteristiek van de stroom, die door het elektrische circuit liep.

Uit onderzoek met raster-transmissie-elektronen-microscopie afgebeeld op een grote hoek- ringvormige donker-veld detector bleek dat elektromigratie in een nanobridge bestaande uit een Pd-Pt-legering geheel andere eigenschappen vertoonde dan die bestaande uit de pure elementen Pt en Pd. De elektromigratie van Pt en Pd lijken erg op elkaar: na rekristallisatie (ook waargenomen voor de Pd-Pt-legering) wordt de brug geleidelijk smaller en breekt vervolgens. In het geval van de legering, blijft de uiterlijke vorm van de brug behouden, terwijl het materiaal van de kathode naar anode getransporteerd wordt, volgens de richting van het elektrische veld en is geheel reversibel. Materiaaltransport correspondeert met de elektron-windkracht, hetgeen een negatieve effectieve kracht aangeeft. Het principe van het regelbare reversibele materiaaltransport in Pd-Pt-legeringen door het veranderen van de polariteit kan gebruikt worden in memristor toepassingen.

De materiaaleigenschappen onder beide dynamische condities, t.w. verwarming en de passage van elektrische stroom, werden in-situ onderzocht. Wij vonden een verhoogde weerstand in Pt nanobridges en correleerden de variaties in weerstand met de vormveranderingen wanneer de poli-kristallijne Pt film verhit werd. Tijdens de elektromigratie-experimenten veranderde de weerstand door twee processen, Joule verwarming en elektromigratie. Door de variatie in weerstand te meten als functie van het verwarmen van het

substraat kunnen deze processen ontkoppeld worden. Deze studie gaf ook het belang aan van de omgevingstemperatuur op de nanobrug: Ondanks dezelfde trend van het materiaaltransport van de kathode naar de anode, verhoogt een hogere omgevingstemperatuur de kans op breken. De hogere temperatuur voegt potentiële energie toe aan de atomen zodat ze makkelijker de energie barrières in het kristal kunnen overschrijden en hun originele posities kunnen verlaten.

In het algemeen: behalve het uitgebreid beschrijven in dit proefschrift van falen door elektromigratie, wordt in dit proefschrift gepresenteerd hoe deze in-situ warmte/elektrische metingen binnen de TEM ook toegepast kunnen worden bij ander onderzoek. Bijvoorbeeld, het ontwikkelde systeem kan gebruikt worden voor molecuul-elektronisch-device-onderzoek naar de eigenschappen van nanodeeltjes of moleculen in combinatie met het zichtbaar maken van vormveranderingen op een atomaire schaal. Het kan ook toegepast worden bij onderzoek naar geheugen-schakel-devices of bij een van de belangrijke onderwerpen van lithium-ion-batterijen.

# Curriculum Vitae

Tatiana Kozlova

- 24 Feb, 1989      Born in Novokuznetsk, USSR
- 2005–2009      **Bachelor of Science** in Physics (Cum Laude)  
Novosibirsk State University, Russia
- 2009–2011      **Master of Science** in Physics (Cum Laude)  
Specialization: Physics of semiconductors and microelectronics  
Novosibirsk State University, Russia  
Thesis: "Aspects of local redistribution of the atomic steps near grooves on Si (111) surface"  
Promotor: Prof.dr. A.V. Latyshev
- 2011–2015      **Doctor of Philosophy** in Applied Physics  
Kavli Institute of Nanoscience Delft  
Delft University of Technology, The Netherlands  
Thesis: "*In situ* transmission electron microscopy investigations of electromigration in metals"  
Promotor: Prof.dr. H.W. Zandbergen



## Publications

1. **Kozlova, T.**; Zandbergen, H.W. *In situ TEM observations of electromigration in Ni nanobridges*, to be submitted
2. **Kozlova, T.**; van Ruitenbeek, J.M.; Zandbergen, H.W. *The origin of increased resistivity in platinum nanobridges studied by in situ TEM*, to be submitted
3. **Kozlova, T.**; Zandbergen, H.W. *In situ visualisation of electromigration in Pt nanobridges at elevated temperatures*. Ultramicroscopy **2015**, 158, 74
4. Dugay, J.; Gimenez-Marques, M.; **Kozlova, T.**; Zandbergen, H.W.; Coronado, E.; van der Zant, H.S. *Spin switching in electronic devices based on 2D assemblies of spin-crossover nanoparticles*. Advanced Materials **2015**, 27(7), 1288
5. **Kozlova, T.**; Rudneva, M.; Zandbergen, H.W. *In situ TEM and STEM studies of reversible electromigration in thin palladium–platinum bridges*. Nanotechnology **2013**, 24, 505708
6. Rudneva, M.; **Kozlova, T.**; Zandbergen, H.W. *The use of STEM imaging to analyse thickness variations due to electromigration-induced mass transport in thin polycrystalline nanobridges*. Ultramicroscopy **2013**, 134, 155
7. Rudneva, M.; **Kozlova, T.**; Zandbergen, H.W. *New Possibilities for In-Situ Electrical Characterization Of Nanosamples at Different Temperatures Combined with Simultaneous TEM Observations*. Microscopy and Microanalysis **2013**, 19 (S2), 456

### Patent:

8. **Kozlova, T.**; Rudneva, M.; Zandbergen, H.W. *A memristor based on electromigration in metal alloy*, Netherlands NL 2010887, Issued May 29, **2013**



# Acknowledgements

The people are the biggest treasure that you can find in life.

In the final pages of this thesis I would like to express my gratitude to the people who directly or indirectly contributed to four years of my PhD journey. Without them, this book would be different and I would be slightly different too.

First of all, I am grateful to Prof.dr. Henny Zandbergen for giving me this great opportunity to work on *in situ* TEM studies for my PhD. Thank you for your time, for your creativity and energy in producing new ideas, thank you for your careful guidance and for all discussions we had. Henny, you are the most curious person I've ever met and it has been a great experience!

I would like to thank Dr.ir. Frans Tichelaar for the help with TEM. Starting from the first sessions on CM30T, you explained us step by step how things are working and made an unknown machine a handy tool. Frans, many thanks for being my first TEM teacher and thank you for restoring microscopes to good shape from any conditions.

Special thanks to my collaborator, Prof.dr. Jan van Ruitenbeek, for informative and productive discussions and newer insights into the vast theory of electromigration.

During my PhD I had an opportunity to be a visiting scholar at Harvard University. I would like to thank Prof. Frans Spaepen, Prof. Ariel Amir, Prof. Zhigang Suo, Prof. Carl Thomson (MIT) and Prof. Caroline Ross (MIT) for informative discussions on my research and their advice.

I would like to thank Prof. Joanne Etheridge for inviting me for a seminar in Monash University, Australia, for her hospitality and good organisation of my visit to the Centre for Electron Microscopy. Great thanks to Prof. Ray Withers for arranging my seminar in Australian National University, and warm thanks to his wife Viki for their hospitality and friendship.

A big thanks to Dr. Julien Dugay, for interesting and productive collaboration on SCO NPs. I appreciate our discussions about the last chapter of this dissertation.

Big part of my PhD project was devoted to the clean room sample preparation. So, I would like to thank Marco van der Krogt, Mark Zuiddam, Charles de Boer, Roel Mattern, Anja van Langen-Suurling, Arnold van Run, Hozan Miro for making fabrication process smooth and workable. Great thanks to Raymond Schouten and Ruud van Ooijik for their help with electrical measurements setup. I would like to acknowledge the people from DEMO, especially Eef Grafhorst and Danny de Gans, who helped to build the new electromigration holder in the middle of my PhD.

Great thanks to my colleagues from HREM group: Dr. Jouk Jansen for the help with all computer questions and for Dutch translation of propositions and summary of this thesis; Tom de Kruijff for technical support and solving many “how to make” questions; Marijke van der Veen for solving all administrative issues and for being always helpful and kind. My special thanks goes to Shiv, I’m happy that we started PhD together and became good friends. Meng Yue, thank you for sharing the office with me and our nice chats. Anil, Yoones, Masha, Leonardo, Ahmet, Chao and Qiang, thank you guys for being good colleagues during all of these years.

My dear paranymphs, Masha and Sairam. Even if I type “thank you” in each line of this thesis it would not be enough to express my gratitude to both of you. Sairam, thank you for each time when you helped me with all kind of experiments, for your patience and responsiveness, you can become a great teacher! Great thanks for our lunches, BBQ, movies, Indian food, Liverpool trip and nice chats. You are a great colleague and friend, I’m happy that we’ll work together a bit more.

Masha, let’s start with science: when I’ve just joined the group, you became my mentor. I’ve learned a lot from you – clean room sample preparation, electrical measurements, wire bonder, probe station... you’ve introduced me to so many people around whom I could ask if something was not working. Great thanks for all of this, because of you my PhD had a fast start and we were able to receive a lot of interesting results during the first two years of our collaborative work. Besides scientific stuff, you are my best friend. Thank you for everything: for our first Amsterdam trip when we were frozen, for Friday cakes, for joint trips, for the talks in the middle of the night, for your willingness to help and for wise advises. Thank you for our shared secrets. It’s great that you believe in people around you.

Moving slowly to the life after six, I would like to thank people who indirectly contributed to this thesis by refreshing the life with their energy. Starting with the tango family: Zaneta and Take, thank you very much for four years of your inspiring dance lessons, for your warm hugs and energy. Thank you Alex for convincing me to join, Quincy, Raoul, Gabi, Maria, Panos, Eleni, Michal, Joey, Eda, Burak, Anna, Pedro, Melody, Mauro, Tim, Perizad... thank you guys for all dances, performances and chats!

I owe special thanks to my Russian-speaking community of friends for making me feel like home, for our Iceland trip, for “Nice in Nice”, for Germany and Belgium, for skiing and sailing. Thank you very much Ilya for being a great neighbor. Denis, thank you for our scientific and non-scientific talks and the tricks shared for ideal presentations. Great thanks to my Novosibirsk friends, especially to Misha, Toma and Anya for all their letters, Skype calls and deep warm home-feeling regardless of physical location.

Oleg, thank you for support, understanding and warmth. Thank you for every day listening, advice and balance of my first-impulse reactions. Thank you for your patience with teaching me how to ski and for the back seat on your bike ;) Thank you for being my family here.

Мои дорогие мама и папа, спасибо вам огромное за веру в меня, за любовь и тепло. Спасибо, что не побоялись отпустить меня в Новосибирск, а потом и в Голландию. Я всегда чувствовала вашу поддержку, и было как-то не так страшно пробовать новое, ведь я знала, что всегда могу вернуться домой. Спасибо за ежедневные звонки, за советы и за безусловную любовь. Я бы очень хотела, чтобы у меня получилось дать своим детям то, что дали мне вы.

Моя Леночка, спасибо тебе, что, несмотря на мои мотания по свету, мы с тобой всё такие же родственные души как в детстве. Спасибо за твою поддержку, советы, за отзывчивость и теплоту. Спасибо за ученого зайчика на моем рабочем столе, когда ничего не работало, он меня спасал.

*Tatiana V. Kozlova,*

*Delft, 2015.*

